12-8-2020 10:30 AM

Uncertainties in the Assessment of Individual and Compound Flooding from River Discharge and Coastal Water Levels under Climate Change

Shuyi Wang, *The University of Western Ontario*

Supervisor: Najafi, M. Reza, *The University of Western Ontario*

A thesis submitted in partial fulfillment of the requirements for the Master of Engineering Science degree in Civil and Environmental Engineering

Abstract

It is widely recognized that climate change can impact the risks of flooding in many regions around the world especially the low-lying coastal areas. The concurrent occurrence of multiple flood drivers such as high river flows and coastal water levels can aggravate such impacts causing catastrophic damages. In this study, the individual and compounding effects of riverine and coastal flooding are investigated over Stephenville Crossing, a town located in the coastal-estuarine region of Newfoundland and Labrador (NL), Canada. The impacts of climate change on flood characteristics and the corresponding uncertainties associated with model inputs and structure, and emission scenarios are assessed. A hydrologic model (HEC-HMS) and a 2D hydrodynamic model (HEC-RAS 2D) are setup and calibrated to simulate the flood inundation for the historical period (1976-2005) as well as near future (2041-2070) and far future (2071-2100) periods under Representative Concentration Pathways (RCPs) 4.5 and 8.5. Results of the HEC-RAS 2D model, including the water surface elevations, are then compared with the 1D model simulations. Future storm events are generated based on projected Intensity-Duration-Frequency (IDF) curves from the convection-permitting Weather Research and Forecasting (WRF) climate model simulations, using SCS, Huff, and alternative block design storm methods. The results are compared with simulations based on projected IDF curves that are derived from statistically downscaled General Circulation Models (GCMs) and the uncertainties from different sources are quantified. Overall, the compounding effects of river overflows, sea-level rise, storm surge and wave can result in extensive inundation of the study area under climate change. The uncertainties associated with climate change impact analyses are propagated from GCMs to flood inundation estimations

through design storms, projected IDF curves and modeling processes. Simulations based on projected WRF-IDF curves show higher risks of flooding compared to the ones associated with GCM-IDFs. This research provides a new approach to apply projected IDF curve for compound flood analysis under changing climate conditions.

Keywords

Compound Flooding, Hydrodynamic Model, HEC-RAS, Climate Change, IDF Curves, Uncertainty Analysis, General Circulation Models (GCMs)

Lay Summary

Flooding is one of the most common natural disasters in Canada which has negative impacts on the economy, society, and environment. More than 600 flood events are recorded in Newfoundland and Labrador's (NL) Flood Events Inventory over the period of 1950-2011 (Atlantic Climate Adaption Solutions Association, 2012). Stephenville Crossing is situated on the west coast of Newfoundland, and the town is located between St. George's River estuary and Rothesay Bay. The location of community makes it vulnerable to both coastal and riverine flooding. The combination of multiple extreme events can cause more catastrophic consequences compared to the individual extreme occurrences. Multiple factors will increase flood risks in Canada with changing climate extremes, including more intense rainfall, warmer temperature, local land subsidence and global sea level rise (Canadian Changing Climate Report, 2019). The interactions between future climate and extreme hazards indicate that it is vital to include climate change analysis in flood analysis. Calibrated hydrological model (HEC-HMS) and two-dimensional hydrodynamic model (HEC-RAS) are used to investigate the individual and combined effects of fluvial and coastal flooding. The flood characteristics based on different projected Intensity-Duration-Frequency (IDF) (generated based on GCMs and high-resolution convection-permitting WRF simulations) are compared. Further, the uncertainties in the generated hyetographs and model parameters are quantified.

Acknowledgement

First, I would like to express my appreciation to my supervisor, Dr. Najafi, who guided my thesis responsibly. Professor Najafi always provided his students the greatest help and resources during our research life. I believe the knowledge and skills gained from his teaching would be very practical for my future work. Thanks Dr. Najafi again for giving his time generously and I would not complete this thesis without his support and constructive suggestions.

I wish to acknowledge the funding provided by the NSERC CRD grant and RiskLogik solutions Inc. Thanks to Dr. Alex Cannon from Environment and Climate Change Canada for providing the projected Intensity-Duration-Frequency curves based on high-resolution WRF model simulations. Also, I would like to thank Dr. Amir Ali Khan and his team from Water Rights, Investigations and Modelling Section in the Department of Environment, Climate Change and Municipalities in Newfoundland and Labrador for providing data, relevant reports and the HEC-HMS hydrological model to setup the flood model and perform extensive analyses.

I would like to extend my gratitude to committee members and examiners, Dr. Robinson, Dr. Dagnew and Dr. Goda. I appreciate your time, feedback, and valuable advices toward improving this thesis.

My thanks would also go to my family for their trust and endless love. I am grateful to my parents for giving me a chance to study in Canada. Your support make me feel warmth, despite there is a long distance between us.

Lastly, I am also deeply indebted my colleagues and friends for their assistance and encouragement. I am so glad that we can experience hard time and enjoy good time together.

Table of Contents

List of Figures

List of Tables

Chapter 1 Introduction

1.1 Background

Flooding is one of the most common natural disasters in Canada (Public Safety Canada, 2020) which has negative impacts on the economy, society, and environment leading to loss of life, infrastructure failures, and damages to properties and ecological systems. In terms of economic damage, with $673 million estimated annual costs floods account for the highest proportion (75%) of extreme weather-related expenses in Canada (Office of the Parliamentary Budget Officer, 2016). Historical Disaster Financial Assistance Arrangement (DFAA) payments in flood damage show there is a rising trend over the past 40 years, which is expected to continue to grow in the future (McClean, 2019). More than 600 flood events are recorded in Newfoundland and Labrador's (NL) Flood Events Inventory over the period of 1950-2011, and only about 8% of them have damage estimates, which are about $252 million in total (Atlantic Climate Adaption Solutions Association, 2012). The actual flood costs may be much higher due to limited damage estimates of flood inventory. According to the Flood Events Inventory, the major cause of flooding in NL is associated with rainfall (72%), followed by coastal flooding (17%), ice jam and snowmelt (7%) and other factors (Atlantic Climate Adaption Solutions Association, 2012).

In general, there are two main factors that can cause or exacerbate flooding, which are natural and human factors. The natural factors include heavy precipitation, storm surges, snowmelt, etc. Floods often happen when the instantaneous rainfall or accumulated rainfall exceeds the discharge

capacity of the river or drainage channels, which sometimes occur in combinations with storm surge. Urbanization is a significant human factor to increase flood risk in urban areas through changes in the hydrological process. Further, climate change is another main factor in flood risk analysis because the sea level rise and increasing intensity of precipitation will increase the frequency and severity of flood events (Najafi et al., 2021; Jalili et al., 2020; Zhang and Najafi, 2020).

Compound weather/climate events are defined as " the combination of multiple drivers and/or hazards that contributes to societal or environmental risk" (Zscheischler et al., 2018) . Ignoring the compounding effects of the hazards/drivers may result in an underestimation of societal and environmental risks (Singh et al., 2020; Singh and Najafi, 2020). For example, when a heavy rainfall event occurs together with high winds and storm surge events, the interaction between riverine and coastal processes can cause compound flooding in coastal areas. In recent years, the impacts caused by compound flooding have drawn attention to understanding the corresponding mechanisms and assessing the resulting flood risks (Zhang and Najafi, 2020).

We study the impacts of climate change on compound flooding in Stephenville Crossing, which is a town on the west coast of Newfoundland. The city is located between St. George's River estuary and Rothesay Bay. The location of the town makes it vulnerable to both coastal and riverine flooding. In the past, this community suffered floods due to storm surge, high river inflows, heavy rainfall, and their combination (Government of Newfoundland and Labrador, 2012). Based on the flood inventory records, the most severe flood event in Stephenville crossing happened in

December 1951 due to storms and high winds, and it caused more than 600 people displaced. Another severe flooding happened in March 2003 caused a loss of $ 14,000 in infrastructures, and the mechanism is the high river inflows due to precipitation and accumulating snowmelt (Atlantic Climate Adaption Solutions Association, 2012).

1.2 Research Gaps

Estuaries and coastal lands are commonly considered as flood-prone areas that can be affected by both inland and coastal flood events. The simultaneous occurrence of multiple flood drivers can result in more serious flood damages compared to their individual occurrences. Nonetheless, previous studies have commonly focused on individual flood generating mechanisms in isolation. Only in recent years, analyses have been conducted to characterize the combined effects of multiple flood drivers (Kumbier et al., 2018; Pasquier et al., 2019; Jalili et al., 2020). Compound flooding has not been studied in the Canadian estuarine areas previously. Further, it is widely recognized that climate change can affect the frequency and intensity of extreme precipitation, storm surge, and sea-level leading to increases in flood risks. However, the impacts of climate change on compound flood characteristics are under researched. In addition, recent efforts to update Intensity-duration-frequency (IDF) curves, which are widely used in engineering and infrastructure designs, considering climate change effects have been mainly based on coarse resolution General Circulation Model simulations which are incapable of accurately representing convective precipitation events. Therefore, these estimates are questionable for short-duration extreme precipitation events that can cause flash floods. Further, there are several sources of uncertainties in climate change impact analyses, such as the variability of GCM structures,

hyetograph designs, hydrodynamic models, and projected IDF curves. A comprehensive evaluation of these sources of uncertainty on flood inundation modelling is lacking.

1.3 Research Questions

Considering these research gaps, we address the following research questions in this thesis:

1. What are the individual and combined effects of fluvial and coastal flooding over Stephenville Crossing?
2. Which areas of Stephenville Crossing are more vulnerable to compound flooding?
3. What are the impacts of climate change on individual and compound flooding in the study area?
4. What are the significant sources of uncertainty in flood inundation assessment under climate change?
5. What are the differences in future flood characteristics associated with projected WRF-IDF and GCM-IDFs?

1.4 Research Objectives

The overall objective of the study is to investigate the effects of compound flooding under climate change by coupling a hydrological model and a hydraulic model. The sources of uncertainties in climate change analyses are identified to help stakeholders to make decisions with the consideration of uncertainty. The proposed research aims to address the following objectives:

1. Assess the individual and compounding effects of fluvial and coastal flooding through a calibrated hydrologic and a two-dimensional hydrodynamic model.
2. Identify the uncertainties in the climate change analysis (including design storm methods, variations of GCMs and approaches of updated IDF curves), and the uncertainties in hydrodynamic modelling (including terrain data, model structure, and roughness coefficient).
3. Compare the flood characteristics based on different projected IDF curves (generated based on GCMs and high-resolution convection-permitting WRF simulations), as well as the hyetographs generation and flow rate simulation conducted by these two updated IDF curves.

1.5 Dissertation Structure

The dissertation is comprised of six major chapters: Introduction, Review of Literature, Study Area and Data Availability, Findings and Discussion, and Conclusion.

- Chapter 1 presents an overall background and motivation for this study. Core research questions and corresponding specific objectives are listed in this chapter, as well as the description of the thesis outline.
- Chapter 2 assesses existing literature related to the research topic and then provides a brief review of different flood types, compound flood analysis, models commonly used in flood inundation mapping, and climate change impacts on flood risk. The potential sources of uncertainties in modeling, General Circulation Models, and methods to update intensity-duration-frequency curves under climate change are discussed.

- Chapter 3 describes the study area in detail, which covers an overview of the river system, land cover/land use conditions. Historical flood events are reviewed to find the main flooding mechanisms in the study region. Required data collection and their availability are also listed as an important part of hydrological and hydrodynamic modeling. The chapter also mentions the data used in climate change impacts analysis.
- Chapter 4 investigates the individual and combined effects of fluvial and coastal flooding under changing climate conditions through an integration of hydrologic and hydrodynamic models. Boundary conditions of hydrodynamic models are enforced with flow hydrographs simulated from the hydrologic model and tide predictions in the form of stage hydrographs. After model calibration and validation, the model is run considering three main scenarios, which represent riverine flooding, coastal flooding and compound flooding under climate change. Besides, a sensitivity analysis of the hydrodynamic model is conducted to improve the reliability and robustness of research.
- Chapter 5 focuses on the uncertainties in the climate change impacts analysis. Different design storm methods and GCM-IDF curve projections are discussed in this chapter. Different future climate scenarios and return levels are simulated to study how the uncertainty propagates through modeling. The applications of two projected IDF curves will be compared to assess their ability in the estimation of future rainfall intensity.
- Chapter 6 concludes the research results. The main findings are highlighted to answer the above research questions, followed by a discussion of the research limitations and recommendations for future research.

Chapter 2 Literature Review

2.1 Flood Types

When a temporary overflow of water inundates normally dry land, this is called flooding. The United Nations Office for Disaster Risk Reduction (UNISDR) and Centre for Research on the Epidemiology of Disasters (CRED) assessed all recorded natural disasters that occurred between 1995 and 2015. It has been observed that the highest occurrence among natural disasters is flooding, which accounts for 43% of total events affecting 2.3 billion people within 20 years (UNISDR, 2015). Throughout the world, two major drivers of flooding are heavy precipitation and high winds with storm surges and waves [Hunt et al., 2005]. The common flooding mechanisms in Canada are associated with heavy rainfall, snowmelt runoff, ice jams, intense coastal storms, and urban stormwater. Nied et al. (2014) described existing approaches to describe flood events, such as the classification into flood types based on the weather patterns, flow characteristics, or geography of flooding area.

Fluvial flooding, also called riverine flooding, occurs when the streamflow reaches the channel capacity and overtops the river banks. Intense rainfall events, heavy snowmelt and ice jams can result in streamflow spread out over the floodplain along rivers. Pluvial flooding can occur in both urban or rural areas when the ground cannot absorb more water due to heavy local precipitation. Overland flow generated by excessive water inundates the area before runoff runs into the water

body (Falconer et al., 2009). Coastal flooding results from extreme water levels, and can be caused by an individual component or a combination of multiple components including high tides associated with astronomical effects as well as storm surge and waves that are associated with strong winds and low atmospheric pressure (e.g. during hurricanes) or tsunamis. When the drainage system or sewer system reaches its capacity during an intense storm, urban flooding occurs due to excessive surface runoff in urban areas. Urbanization is one of the important factors that can negatively impact soil infiltration and water storage capacity, and these impacts cause increases in the rate and volume of stormwater runoff. One-dimensional (Mark et al., 2004), two-dimensional (Hunter et al., 2008) and coupled hydraulic models (Seyoum et al., 2012) are developed and applied for urban flooding analysis, as well as models combined with geographic information system tools and satellite missions (Chen et al., 2009; Elkhrachy, 2015).

Previous studies have been focused on analyzing the individual occurrence of flood events including pluvial (Falconer et al., 2009; Yin et al., 2016; Maksimovic et al., 2009 Lowe et al., 2017), fluvial (Yu et al., 2006; Beven et al., 2011), and coastal (Bates et al., 2005; Didier et al., 2015; Didier et al., 2019). Maksimovic et al. (2009) modelled the overland flow and flow pathway during pluvial flooding by analyzing the interactions between a one-dimensional surface system and drainage system in UK. The risk of pluvial flooding is also be studied in Greater Toronto Area through Bayesian belief network flood vulnerability model and geographic information system (Abebe et al., 2018). Yu et al. (2006) simulated fluvial flood through a two-dimensional hydrodynamic model, JFLOW, and evaluated the effects of varied mesh resolution on flood inundation prediction. A simple two-dimensional hydrodynamic model, LISFLOOD-FP, is

outlined by Bates et al. (2005) and successfully applied on coastal flooding simulation for large estuary with an advantage of high computational efficiency. Didier et al. (2019) conducted flood-mapping research in Eastern Canada, which sometimes suffers coastal flooding related to hurricanes. The results show the coastal flooding map derived from hydrodynamic model simulations performs better than that derived from static bathtub simulations. The interaction between tide and surge is also be studied at the east coast of Canada through a dynamic model, and the research illustrates the importance of tide-surge interaction for flood forecasting within coastal region (Bernier et al., 2007).

It is widely recognized that climate change can affect the individual drivers of flooding including pluvial(Zhou et al., 2012; Kaspersen et al., 2017; Evans et al., 2020; Pregnolato et al., 2017), fluvial (Eccles et al., 2019; Wilby et al., 2008; Van et al., 2012) and coastal (Purvis et al., 2008; Didier et al., 2019; Garner et al., 2017; Thompson et al., 2009). The investigation of the impacts of pluvial flooding and climate change mainly focus on urban region, for example, the effects on road traffic in UK (Pregnolato et al., 2017) and in Spain (Evans et al., 2020). Eccles et al. (2019) indicated the changing climate causes the increases in riverine flooding within tropical and sub-tropical regions, while further studies can focus on other regions and small-medium sized catchments. In 2009, Thompson et al. had focus on coastal flooding and changing climate in Atlantic Canada by estimating the extreme sea levels in two ways, storm surge modelling and statistical analysis. The results show both two approaches have the ability to predict the return level changes in the future, however, the effect of global sea level rise and the change frequency of storm events does not be assessed in this study. With the impact of climate change, studies start to focus on the relationship

between sea level rise and fluvial flooding (Garcia et al., 2014; Mosftakhari et al., 2017), as well as coastal flooding (Woodruff et al., 2013; Hinkel et al., 2014; Neumann et al., 2015). The frequency of 50-yr water level events is projected to double in Newfoundland due to around 10 cm of sea level rise (Vitousek et al., 2017).

Stephenville is frequently affected by riverine and coastal flooding based on the records of historical flood events. The coastal side of Stephenville Crossing suffers flooding due to surge, waves and high tides from St. George's Bay, whereas the inland side is also affected by tide and surge, and sometimes combined with river floods that flows into St. George's River. This study will mainly focus on the effects of coastal and riverine flooding on the urban area and the area along the river. Although comprehensive analyses have been conducted to evaluate the risks from individual flood drivers, the analysis of the joint impact of compound hazards is under researched.

2.2 Compound Flooding

Compound events are associated with the simultaneous occurrence of two or more events or events that occur in close succession. The combination of multiple extreme events (or events that are not extreme, individually, but their compounding effects can result in an extreme impact) can cause more catastrophic consequences compared to the individual extremes. Zscheischler et al. (2018) defined compound climate events as the combination and interaction of multiple climate drivers and hazards that cause significant impacts on the society and environment. Compound flooding, such as the co-occurrence of fluvial floods and extreme coastal water levels, may lead to

significant impacts in densely-populated low elevation coastal zones (Ganguli and Merz, 2019). Drivers comprise weather phenomena and related climate processes; for example, surge, tide, precipitation, and wind could be the drivers of coastal flooding.

Compound flooding involves multiple drivers or mechanisms of flooding, such as the combination of rainfall and storm surge (Wahl et al., 205; Couasnon et al., 2020; Herdman et al., 2018; Bilskie et al., 2018; Saleh et al., 2017; Ray et al., 2011). High river runoff from fluvial flooding and direct rainfall-runoff from pluvial flooding can be triggered by intense precipitation. Storm surge is an abnormal rise in sea level during intense storms that can lead to coastal flooding individually or sometimes combined with heavy waves and high tides. Compound flooding from precipitation and storm surge commonly occurs in the low-gradient coastal regions, which can severely impact the developed areas with high population density. In recent years studies have been performed to estimate the probability of compound flooding caused by multiple drivers occurring simultaneously or successively at a local scale (Serafin et al., 2019; Lian et al., 2013), regional scale (Zheng et al., 2013; Wahl et al., 2015), continental-scale (Bevacqua et al., 2019) and global scale (Couasnon et al., 2020). Therefore, it is critical to simulate the potential compound risks from rainfall-runoff and storm surge flooding in coastal regions.

Santiago et al. (2019) reviewed the current methods of coupled multiple models in low-lying coastal areas for compound flooding analysis. The most commonly used technique is the linked technique due to its simple application. The information between numerical models is transferred in one way, which means that the results from one model can be used as the inputs of another

model (Santiago et al., 2019). The hydrologic and hydrodynamic models have been widely used to assess the impacts of compound flooding from riverine and coastal flooding in Australia (Kumbier et al., 2018), in U.S. (Bacopoulos et al., 2017; Bakhtyar et al., 2020; Bunya et al., 2010; Saleh et al., 2017; Ray et al., 2011) and in Korea (Lee et al., 2019). For instance, Ray et al. (2011) studied the combined effects of storm surge and inland precipitation through steady and unsteady analysis. The time-series of storm surge water elevations driven from storm surge models and rainfall inputs were used to simulate the compound flooding in hydrodynamic models, HEC-RAS. However, uncertainties arise from the timing and intensity of storm surge or rainfall events. They act as separate events during simulation and event peaks may not always happen at the same time. In this research, the interactions between numerical models are simplified as much as possible to represent compound flooding, but there may still be misinterpretation for real situation events. Kumbier et al. (2018) investigated compound flooding effects in an Australian estuarine environment by considering the storm surge and extreme riverine discharge. A hydrodynamic model, Delft3D, is used to simulate flood extent and flood depth with or without upstream river discharge. The underestimation of the inundation area and flood depth shows the importance of considering the river discharge for flood analysis in the estuary region. The study of riverine-estuarine flooding was also conducted on Florida's river basin by applying hydrological and hydrodynamic models (Bacopoulos et al., 2017). All in all, no research has focused on compound flooding analysis in a Canadian estuarine area. Saleh et al. (2017) applied multiple models in the research of compound costal-riverine flooding in New York, included ensembles from numerical weather prediction models, hydrologic model HEC-HMS, Coastal model NYHOPS, and hydraulic model HEC-RAS 2D. Ensembles forecasting data as the inputs of hydrologic and coastal model is used to simulate inflow rates and coastal water levels, and then the boundary conditions of

hydrodynamic model are forced by the results from HEC-HMS and NYHOPS. The uncertainties within weather prediction ensembles can propagate through multiple models on flood inundations. The simulations are based on two historical extreme flood events, however, the changing climate also bring uncertainty from weather forecasting models.

2.3 Modeling

Setting-up models to solve practical problems is a common approach in engineering designs. Hydrological and hydrodynamic models play an essential role in characterizing river systems and basins. A flood model for a watershed is developed with required input data to simulate flood events, such as hydrological data, watershed characteristics, and specific boundary conditions. Combined with a hydrological model and Geographic Information System, the application of the flood model can be extended to flood protection and flood extent visualizations. The hydrological model is the simplification of actual physical processing by a set of equations and defined basin characteristics. River flows simulated by the hydrological model are used to drive the hydraulic model to characterize channel flows, and the potential flooding areas are delineated with the help of GIS. Hydrological and hydraulic modeling are widely used tools in flood analyses, which help with the identification of inundated areas and the investigation of flood risks for both historical and future events.

2.3.1 Hydrological Model

The hydrological model uses a set of equations to simulate hydrological processing, which includes two major components: parameters used to describe the catchment characteristics and input data used to drive the model and simulate runoff. Parameters are varied between each hydrological feature to describe watershed characteristics; for example, Curve Number used in the calculation of infiltration loss is based on soil properties and land cover. The inputs include weather data such as rainfall and snow measurements from gauges or remote sensing records. Freeze et al. (1969) provided a blueprint for the hydrologic response model and provided suggestions for future model development. The development and application of hydrologic models were discussed with the consideration of data availability, model complexity, model performance and calibration (Gupta et al., 1998; Wangener et al., 2001). After conceptualizing the model system, the optimum use of available data is determined based on multiple objectives evaluation. The model uncertainty is also investigated if it is within an acceptable range when the model performance is sufficient for users' modelling purpose (Wangener et al., 2001). Nowadays, various types of models have been applied in engineering problems, and the hydrological model is considered as a core tool for water resources management (Devia et al., 2015).

Hydrological models are classified as deterministic and stochastic models based on mathematic structure (Shaw et al., 1983). Considering model spatial processes, hydrological models are categorized as lumped, semi-distributed, and fully-distributed model. The lumped model describes the catchment as a single unit without spatial variation, the distributed model considers spatial variability by small grid cells, the semi-distributed model considers the spatial variability by sub-

catchments within the whole watershed. The lumped model has the least computational cost, but it losses characteristics of basics with a relatively low spatial resolution. The fully-distributed model has a much longer computation time, and it requires more data for each cell. The semi-distributed model is the balance between lumped and distributed model with an average of computational time, spatial variability, and data collection.

Currently, there are wide ranges of semi-distributed models used by researchers worldwide, such as Hydrological Modeling System (HEC-HMS) by U.S. Army Corps of Engineers, Topography Base hydrological Model (TOPMODEL), and Soil and Water Assessment Tool (SWAT). HEC-HMS is one of the hydrological models commonly adopted to estimate runoff of a watershed system due to its simplicity in model operation and flexibility in simulation time (Razi et al., 2010; Halwatura et al., 2013; Tassew et al., 2019). Basic hydrological processing analysis includes infiltration loss, direct runoff, base flow, and channel routing, as well as soil moisture, evapotranspiration, and snowmelt (U.S. Army Crops Engineers, 2008). Ramly et al. (2020) develop a framework that can provide accurate radar rainfall data as the inputs of HEC-HMS, and then it can be applied in flood risk analysis by simulating of future flood events. With the help of HEC-GeoHMS extension in ArcGIS, it is easier to prepare model spatial parameters related to topography data in the model set-up. The combination with other software tools also extends the model ability in flood forecasting, flood control measures, and floodplain delineation. The majority of studies integrated HEC-HMS with hydraulic model and GIS (Knebl et al., 2005; Anderson et al., 2002; Abdessamed and Abderrazak, 2019). Coastal model or storm surge model could be coupled with hydrologic model as the boundary conditions of hydrodynamic model in compound

flooding analysis, which considers heavy rainfall and storm surge together (Saleh et al., 2017). Similar studies also are conducted in compound flooding analysis involving HEC-HMS model, for example the study of Hurricane Ike 2008 (Ray et al., 2011) and Typhoon Maemi 2008 (Lee et al., 2019). Besides the application of hydrologic model, hydrodynamic model is also crucial for compound flooding analysis.

2.3.2 Hydrodynamic Model

Teng et al., (2017) reviewed the capability of the existing modelling techniques and discussed their advantages and limitations. The selection of modelling approaches involves the balance of computational costs, data availability, model set-up and user's objectives. Hydrodynamic models have a relatively wide suitability in flood related research, such as flood risk, flood damage, flood forecasting, and flood control. Hydrodynamic models are mathematical models designed to investigate water movements by solving governing equations. Based on the spatial representation of water flow, hydrodynamic models can be categorized into three types: one dimensional (1D), two-dimensional (2D) and three-dimensional (3D) model. 1D models can simulate the flow along the river, and different 1D models have been developed and applied in flood inundation analysis, including MIKE11 (Thompson et al., 2004), InfoWorks RS (Mah et al., 2007) and HEC-RAS 1D (Horritt et al., 2002; Hicks et al., 2005; Masood & Takeuchi, 2012). They describe the channel geometry along the river centerline based on multiple cross-sections, and flow is represented in one direction which is parallel to the channel. Flow depth at each cross-section is taken to assess whether the surrounding areas are flooded and to distribute the flow based on topography with the

help of a geographic information system or other tools. The number and location of cross-sections are essential to provide accurate information on the geometry of the river system (Ali et al., 2015). 2D models have attracted much attention from researchers and practitioners, and many two-dimensional models are developed and applied for flood analysis in recent decades, such as LISFLOOD-FP (Fernandez et al., 2016; Van Der Knijff et al., 2010; Neal et al., 2011; De Roo et al., 2001). Two-dimensional models describe floodplain flow as two-dimensional mesh, and assume another dimension, water depth, is relatively shallow. 2D models are simulated by much denser mesh cells compared to the simple cross-section in 1D models. Hence 2D models solve the problem of 1D models to represent complex topography, but they require more substantial computational time. Taking advantage of one-dimensional and two-dimensional models, the coupled 1D/2D hydrodynamic model is developed and used in floodplain research, such as MIKE FLOOD (Patro et al., 2009) and 1D/2D HEC-RAS (Patel et al., 2017; Pasquier et al., 2019) and SOBEK 1D/2D (Vanderkimpen et al., 2008; Carrivick et al., 2006). Coupled 1D-2D HEC-RAS provides the simulation of river flow in one-dimension and the simulation of floodplain flow in two-dimension, and cross-sections in 1D features could be connected with 2D mesh area through structures, like levees (Patel et al., 2017). Although coupled 1D-2D model has the advantage of balance of simulation accuracy and computational time, the parameters described the coupling could reduce model stability and cause further uncertainty. With the advancement of computational technology, complex 3D models are developed to represent vertical flow features, such as Delft3D (Kumbier et al., 2019). Alcrudo et al. (2004) states 3D models are not necessary for broad floodplains, especially when the 2D model is well-calibrated and validated. Currently, two-dimensional hydrodynamic models are the most commonly used models for generating flood maps and investigating related flood risks. A detailed comparison between 2D HEC-RAS and

LISFLOOD-FP models has been conducted by evaluating computational time and performance in a complex topographic region (Shustikova et al., 2019). The simulated flood extent and water levels at 25m-resolution were similar without significant difference. LISFLOOD-FP was more efficient due to faster running speed, while HEC-RAS had better performance for areas with relatively complex terrain.

In recent researches, compound flooding associated with coastal and riverine flooding has been analyzed using HEC-RAS model (Saleh et al., 2017; Serafin et al., 2019; Pasquier et al., 2019; Gori et al., 2020), Delft3D model (Herdman et al., 2018; Kumbier et al., 2018; Lee et al., 2019), and MSN_Flood model (Comer et al., 2017; Olbert et al., 2017; Kirkpatrick and Olbert, 2020). Pasquier et al. (2019) integrated 1D-2D HEC-RAS model to assess the sensitivity of different sources of flooding happened in coastal regions, and the results show the storm surge is likely to be the main driver of flooding for current and future. Only sea level rise is considered as future climate change condition, the changes in the pattern and intensity of precipitation still remain uncertain for compound flooding analysis (Singh and Najafi, 2020). Hydrodynamic model Delft3D is coupled with hydrologic model HEC-HMS for the simulation flood event happened during Typhoon Maemi, and two models are responsible for tidal and storm surge and river discharge respectively (Lee et al., 2019). The case included river discharge has better performance than the case only consider storm surge and tide, and that illustrates coupled hydrodynamic-hydrologic model is appropriate approach for compound flooding analysis. Although MSN_Flood model has successfully been applied in the simulation of coastal-fluvial flooding event, the misrepresentations still exist in model, such as turbulence and model forcing, and also the model's

spatial resolution can affect simulation accuracy and cause more uncertainty in model performance (Olbert et al., 2017). Compound flooding happened in estuarine areas has been investigated through Delft3D model (Kumbier et al., 2018) and coupled 1D-2D Mike Flood model (Webster et al., 2014). The ability of two-dimensional HEC-RAS in the simulation of multiple-drivers flooding can be explored in an estuary region, like the town of Stephenville Crossing, also a comprehensive climate change analysis should be conducted, especially included the changes in short-duration rainfall events.

Previous studies have conducted sensitivity analysis to investigate different sources of uncertainty and determine the influential factors. This is a necessary step to improve the reliability and practice of hydrodynamic models. Such analyses have been focused on input data (Vojtek et al., 2019; Feng et al., 2016), model structure (Liu et al., 2019), model configuration (Papaioannou et al., 2016), model parameters (Liu et al., 2019; Pappenberger et al., 2005), and terrain data (Pender et al., 2016; Cook et al., 2009). Flooding studies usually consider the most influential factor is friction parameter in hydrodynamic model, however, the ranking of sensitivity factors could be changed with different methods, models, and study regions. There is no firm conclusion about the importance of parameter factors that are applicable for all studies (Pappenberger et al., 2008). Sensitivity analysis is still a crucial step to understand the uncertainties in hydrodynamic modeling for detailed regional study. In addition to the uncertainties in model, the uncertainty related with design storm methods and climate change analysis should be addressed.

2.4 Projected Impacts of Climate Change Impacts on Flooding

The current and future climate are affected by human activities and natural climate variability. To understand the current and future climate change, General Circulation Models (GCMs) can simulate many elements of natural variability and anthropogenic factors based on emission scenarios. The 5th Assessment Report of the Intergovernmental Panel on Climate Change (IPCC AR5) indicated that climate change can affect hydrological parameters, like rainfall and snow, which are the main contributors to pluvial and fluvial flooding events. Canadian Changing Climate Report (CCCR) 2019 also illustrates that multiple factors will increase flood risks in Canada with changing climate extremes, including more intense rainfall, warmer temperature, local land subsidence and global sea level rise. Through the re-analysis of Alberta flood in 2013, increasing greenhouse gas emissions could increase the likelihood of extreme rainfall that may cause flooding under changing climate. The interactions between future climate and extreme hazards illustrate that it is vital to include climate change analysis in flood analysis (Seneviratne et al., 2012). The potential risk of fluvial floods is also projected to increase under the impact of climate change (Wilby et al., 2008).

In recent years, flood assessment under the impact of climate change has received wide attention worldwide, such as New York City (Garner et al., 2017), Europe (Alfieri et al., 2015; Bevacqua et al., 2019) and Asia (Ali et al., 1996; Gao et al., 2020; Karim et al., 2008; Shrestha et al., 2017), as well as the global scale (Arnell et al., 2016). Gaur et al. (2018) estimate streamflow across Canada

based on multiple General Climate Models with different future scenarios. The results show the flood frequencies are projected to increase in northern Canada, like Yukon and Nunavut, under climate change with the least uncertainty, however, part of Newfoundland Island can be expected to have a decreasing trend of flood frequency but with the most uncertainty. That mean there was a lower degree of confidence in the projections of decreasing flooding frequencies. The future changes of runoff may still cause an increase in flooding frequency and flooding risk with the combination of other climate drivers, therefore it is still necessary to investigate flooding risk in flood-prone regions of Newfoundland.

Compound flooding analysis can be conducted through a historical event, such as Hurricane Irene and Sandy (Saleh et al., 2017), Typhoon Maemi (Lee et al., 2019), Cyclone Sidr (Ikeuchi et al., 2017), and Hurricane Isabel (Blanton et al., 2018). Besides the research of existing flood event, more researches focus on compound flooding with the impact of climate change recently (Herdman et al., 2018; Kirkpatrick and Olbert, 2020; Erikson et al., 2018; Pasquier er al., 2019). The compound effects of river overflows, sea level rise and extreme storm surge may cause more severe and frequent flooding. Therefore, it is necessary to understand the combined risks of potential weather drivers because it helps to manage the estuarine environment effectively and conservatively under current and future periods. Kirkpatrick and Olbert (2020) assess the changes in flood mechanisms caused by extreme flow and sea level rise under climate change, and simulated potential flood inundation area with the consideration of the various level of future climatic scenarios. Very limited researches focus on climate effects on compound flooding in the Canadian estuary region. Flooding analysis is conducted in an open estuary of eastern Canada,

however it is only for coastal flooding mapping (Didier et al., 2018). Webster et al. (2014) investigate riverine-coastal compound flooding in an estuarine area of Nova Scotia with the consideration of future sea level rise. The study adopts a coupled 1D-2D Mike flood model for river and floodplain flow simulations respectively. The future scenario is represented by the combination of mean high tide and future sea level rise predictions in 2D hydrodynamic model Mike-21; while the 50 and 100 return periods of extreme river discharge based on historical records are considered as the upstream boundary condition of 1D hydrodynamic model Mike11. Changing climate not only causes sea level rise, but also affects future temperature and precipitation, therefore future extreme event estimations could be further explored with the help of climatic model simulations.

Intensity-duration-frequency (IDF) curves have been widely used in engineering and infrastructure designs. In future climate impact analysis, IDF curves can be updated based on historical and future climate model simulations. General Circulation Models (GCM) are numerical climate models that represent physical processes of land, ocean, atmosphere and their interactions. Simonovic et al. (2016) adopted equidistant quantile-matching method for downscaling precipitation data to establish a statistical relationship between annual maximum precipitation of climate model baseline and sub-daily historical observations. A relationship between annual maximum precipitation from GCM baseline and GCM future scenarios is established through the quantile delta mapping method to update IDF curves (Simonovic et al., 2016). However, the resolution of GCM is too coarse to capture small-scaled physical processes, in particular short-duration rainfall extremes may not be adequately modeled in GCMs. Cannon et al., (2019) propose a method to

project intensification of rainfall extremes from the high resolution (4-km) Weather Research and Forecasting (WRF) model, which is a numerical weather prediction model designed to simulate meteorological processes and provide weather forecasting. A Generalized Extreme Value Simple Scaling (GEVSS) approach is adopted for IDF curve estimation, and the future changes in GEVSS parameter are estimated to evaluate the changes of sub-daily rainfall extremes. This approach is not bound by the stationarity assumptions of IDF changes and scaling factors can change for events with different durations (Cannon et al., 2019). To assess the future impacts of climate change on flood risks, it is crucial to evaluate the uncertainties associated with the projected IDF curves. Such analysis is lacking in flood-related studies.

Climate change impact analysis involves many sources of uncertainties. Therefore, identifying the uncertainties and understanding their influences are a crucial part of improving the model reliability. There is extensive research on GCM development and its applications as a core climate driver in future climate analysis. The uncertainties associated with GCM structure, future emission estimation, downscaling methods, and hydrological models have been widely investigated in many climate change impact studies (Kay et al., 2009; Chen et al., 2011; Najafi et al., 2011; Najafi et al., 2017). Her et al. (2019) state the main contributor to uncertainties in climate change analysis is GCM projections when rapid hydrological components are simulated. Regarding the reliability and quality of further research, GCM selection becomes more critical because hydrological and hydrodynamic models highly rely on the model dataset as inputs (Abbasin et al., 2020a; Abbasian et al., 2020b).

Chapter 3 Study Area and Data

3.1 Study Area

3.1.1 Overview

The Newfoundland and Labrador (NL) province is located in eastern Canada, and consists of the Newfoundland Island in the Atlantic Ocean and continental Labrador. The Town of Stephenville Crossing is located on western coast of Newfoundland Island at 48° 31' N latitudes and 58° 27' W longitude (Figure 3.1). According to 2016 Canada Census data, approximately 1700 people reside in the town, which represents 0.33% of the total population in NL. The land area of Stephenville Crossing is 31.2 square kilometers, but most of the population is concentrated on the coastline and along Harry's river (Statistics Canada, 2016).

The area between the coastline and the mouth of Harry's River is particularly important because many residences and commercial premises are located here. A hospital and a rescue organization provide daily and emergent services for surrounding communities. In addition, there is a long-term government based care center, which provides service to over 100 seniors (Western Health, n.d.).

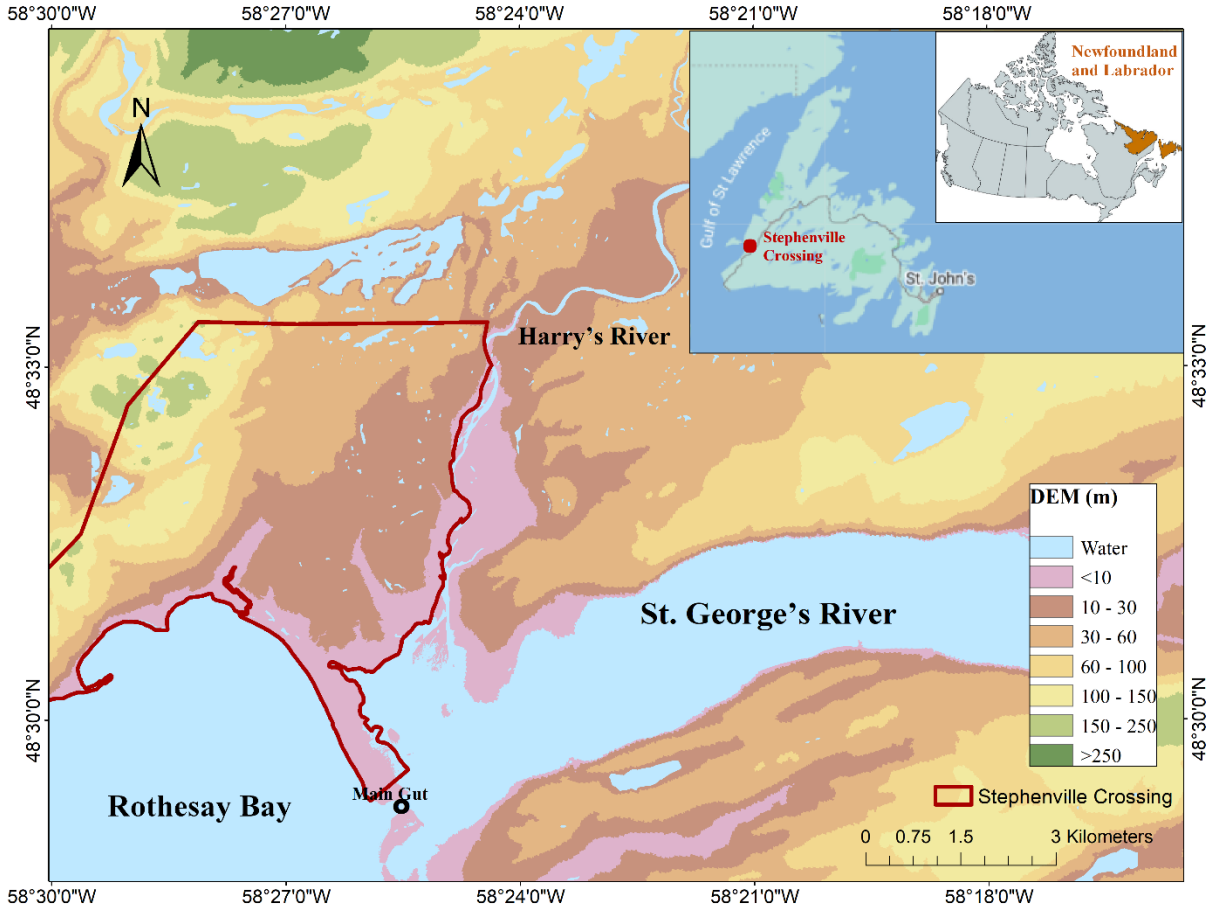

Figure 3. 1 Study area including the Town of Stephenville Crossing

In the study area (Figure 3.1), the average monthly temperature varies between around -7°C and 16°C and the annual average relative humidity is 81% (Environment and Climate Change Canada, 2019). The lowest and highest temperature occurs in February (-10°C) and August (20°C), respectively. Precipitation is much lower in March, April, and May compared to the other months. From the period of 1961-1990 to 1981-2010, the Canadian Climate Normal shows a slightly increasing trend in both temperature and precipitation. During the winter, winds are stronger than other seasons, and the maximum wind gust can reach approximately 140km/h (Environment and Climate Change Canada, 2019).

The town of Stephenville Crossing is located at the far east of St. George's Bay. The east side of the study area is St. George's River estuary, and the west side is part of the Bay of St. George, called Rothesay Bay. Harry's river discharges into St. George's River from the north, and Southwest Brook discharges into St. George's River from the far east. St. George's River flows westward into Rothesay Bay through a narrow channel called Main Gut (Figure 3.1). The drainage area of gauge station (Harry's River below Highway Bridge, see Figure 5.3) is 640 km², and the drainage area into St. George's River is 1670 km² in total, which including the drainage of the mouth of Harry's River, the eastern tributary and river's local drainage area (Government of Newfoundland and Labrador, 2012). There are two bridges across the Main Gut to link the town of Stephenville Crossing with other communities. The new Stephenville Crossing Gut bridge is constructed on Route 490, and the abandoned railway bridge is beside it. Besides, at the upstream of Harry's River, there is a bridge built on Route 460.

3.1.2 Land Use and Land Cover

The study region is mainly covered by forest, based on a 2015 Land Cover of Canada with resolution 30m. This land cover map is extracted from Landsat's Operational Land Imager with an accuracy of 79.9% (Nature Resources Canada, 2019). Landsat is a satellite program operated by National Aeronautics and Space Administration (NASA) and U.S. Geological Survey (USGS), and Operational Land Imager helps with the collection of Earth's surface image. Other major parts of the study basin are covered by shrubland and wetland along the river system. The original land cover map is reclassified into eight main types (Figure 3.2) and the corresponding roughness values

are listed in Table 1 (Chow, 1959). Only a small part of the region is developed, and these urban areas and built-up areas are situated in the region between the bay and the estuary of Harry's River.

The land use map of the town of Stephenville Crossing is shown in Figure 3.3. Town zone is planned between the estuary and the bay, and the floodway is designed around it. Designated Floodway is the area that has potential higher flow velocities and more flood damages, typically, the floodway includes the stream channel and adjacent areas (Municipal Affairs of Alberta, 2014). The small area located in the south of town is planned as flood fringe, which is part of floodplain between the designed floodway and edges of flood vulnerability zone. Flood fringe zone has relatively shallow water, lower flow velocities and less potential flood damages.

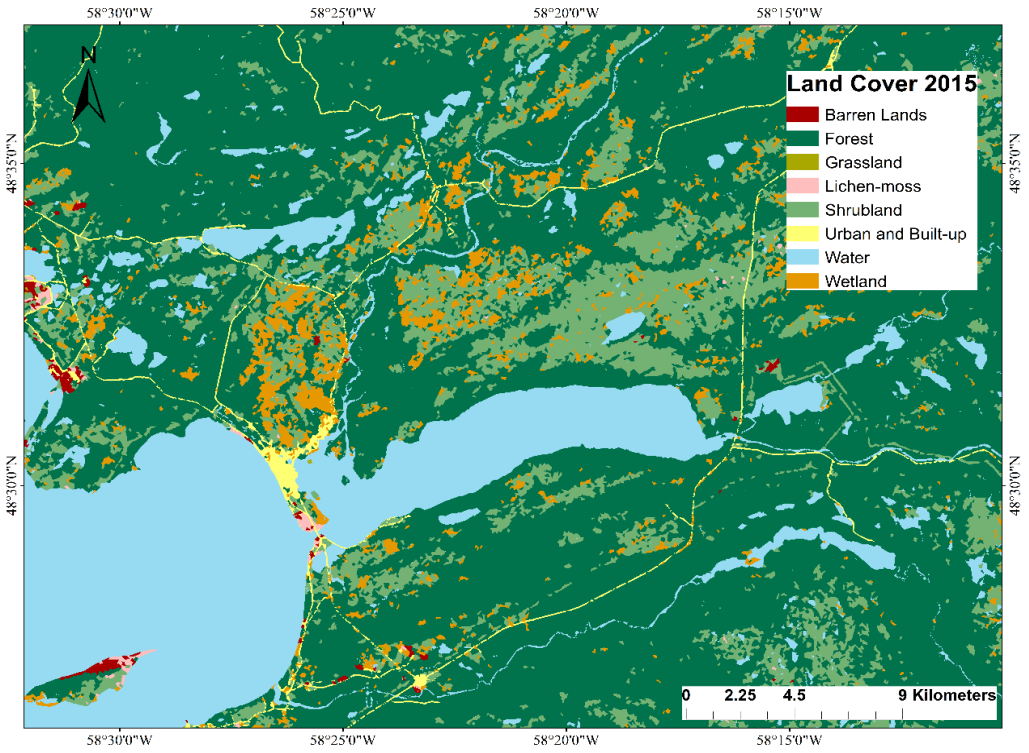

Figure 3. 2 Land Cover Map 2015 (Natural Resources Canada, 2019)

Table 3. 1 Roughness value (manning's n) for each land cover type

Land Cover Type	**Roughness (Manning's n)**
Barren lands	0.03
Forest	0.13
Grassland	0.04
Shrubland	0.12
Lichen-moss	0.03
Urban	0.1
Water	0.04
Wetland	0.1

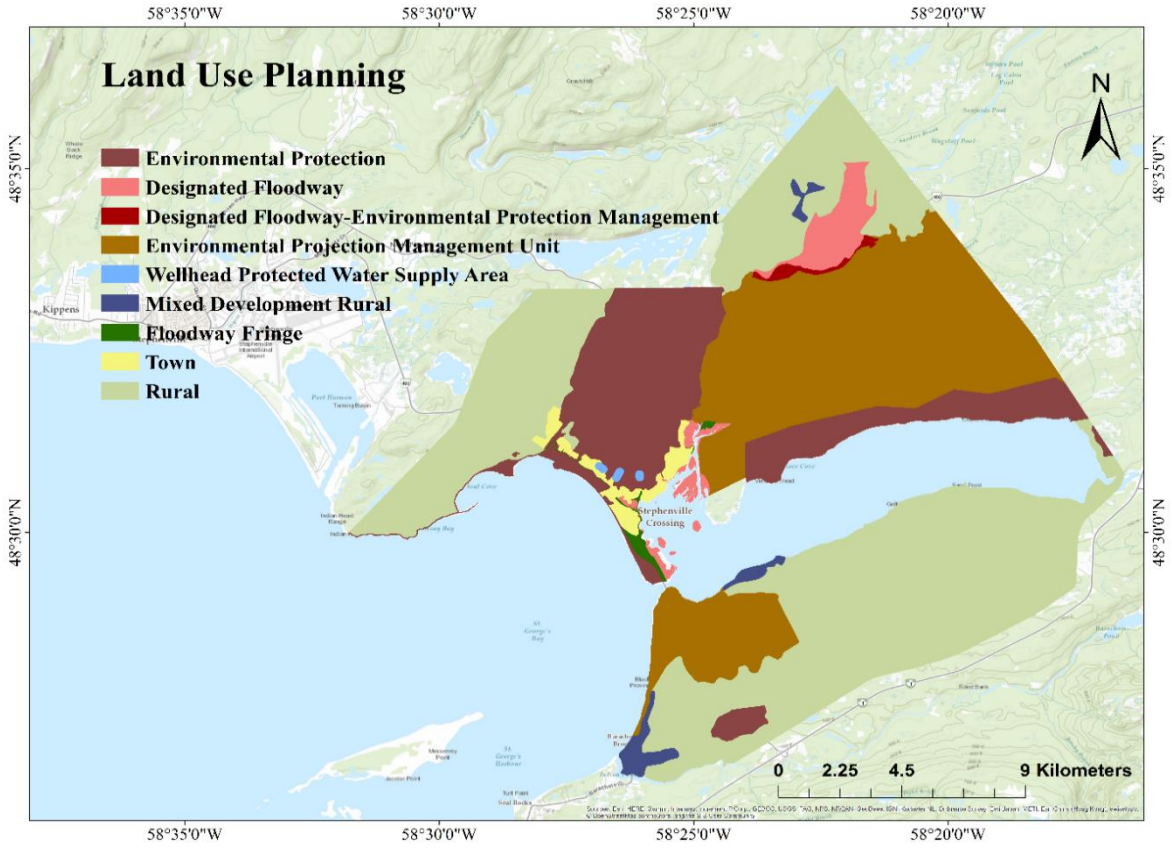

Figure 3. 3 Land Use Planning Map (Government of Newfoundland and Labrador)

3.1.3 Historical Floods

Flood disasters have repeatedly occurred in this area in the past. The details and losses of some of the recorded flood events are described. In late December 1951, coastal flooding affected the area resulting in the displacement of ~600 people. The severe storm caused high-speed winds of 110 miles per hour that swept through the railway station and destroyed 15 surrounding electrical poles. Many fishermen lost their boats and tools. In addition to seawater overtopping the coastal area of Stephenville Crossing, heavy rainfall resulted in Harry's River overflowing the streets. Some stores and house interiors were damaged (Atlantic Climate Adaption Solutions Association. 2012). In December 1977, another coastal flooding forced five families to evacuate and caused house damages. High winds and tides brought flooding again and washed out the road and streets. Surrounding communities also reported damages due to this flood inundation (Atlantic Climate Adaption Solutions Association, 2012). A flood event in March 2003 caused a loss of $ 14,000 in infrastructures. The weather warmed in spring, and the snow and ice melted rapidly. Precipitation and the simultaneous melting of ice in multiple rivers caused high inflows. The flood brought about bridge damage, highway closure, and water in the basement (Atlantic Climate Adaption Solutions Association, 2012). In early November 2014, a gusty wind of up to 110 kilometers per hour caused flooding, and roads were closed (CBC News, 2014). As Figure 3.4 shows, the pavement in Stephenville Crossing experienced flooding due to high waves.

Considering the historical records of flooding, the main contributors of flooding in Stephenville Crossing are heavy precipitation causing rover overflows and coastal high winds and tides. Due to

the location of the town, damages and losses could become more significant under compound flooding, hence it is vital to conduct flood analysis of both riverine and coastal drivers.

Figure 3. 4 Flood event of November 2014 happened in Stephenville Crossing (CBC News, 2014)

3.2 Data

3.2.1 Topographic Data

As discussed in chapter 2, both hydrological and hydrodynamic models rely on accurate topographic data, especially for two-dimensional flood modelling. Many studies have investigated the importance of quality and resolution of terrain data in hydrodynamic models with different spatial and temporal scales. In this study, we use three different types of digital elevation models (DEM): SRTM, CDEM, and TanDEM-X. Light Detection and Ranging (LiDAR) survey was

completed in September 2010 at a high-resolution of 1m (Terrapoint, 2010). This high-resolution digital elevation data is only available at the western coast of Stephenville Crossing, therefore LiDAR DEM does not cover the entire simulation area.

Canadian Digital Elevation Model (CDEM) is provided by Natural Resources Canada, and covers entire Canada. In areas south of 68°N latitude, the spatial resolution is 0.75 arc-second (~20m) (Natural Resources Canada, 2013). The measured altimetric accuracy of CDEM in the study area is within a range of 5-10m under Canadian Geodetic Vertical Datum 2013 (Government of Canada and Natural Resources Canada, 2013)

Shuttle Radar Topography Mission (SRTM) by National Aeronautics and Space Administration (NASA) provides the global-scale digital elevation data at three arc-seconds and one arc-seconds resolution, which are approximately 90m and 30m resolution, respectively. 30m SRTM data is available to cover Stephenville Crossing, which has an absolute vertical accuracy of below 16m and absolute horizontal accuracy of less than 20m under vertical datum of Earth Gravitational Model 1996 (https://www2.jpl.nasa.gov/srtm/statistics.html).

German Aerospace Center's TanDEM-X is a synthetic aperture radar mission that can generate global digital elevation data at three arc-seconds spatial resolution. The absolute horizontal and vertical accuracies are below 10m within 90% confidence interval under vertical datum of World

Geodetic System 1984. This DEM data is freely available and can be obtained from the website of Geoservice under German Aerospace Center (https://geoservice.dlr.de/web/dataguide/tdm90/).

During a 2010 survey conducted by Hatch, 46 detailed cross-sections were collected along Harry's River. DEM does not contain the terrain information below water bodies, therefore the channel bathymetry was included in channel flow simulation. Hence all available cross-section lines were interpolated to generate the river bathymetry. Then, the resulting bathymetry data was fused into all DEMs for further simulation.

3.2.2 Precipitation and Hydrometric Data

There are three climate stations and one hydrometric station operated by Environment and Climate Change Canada (ECCC) within the basin (Figure 3.5). In this study, the climate station at Stephenville Airport and the hydrometric station 02YJ001 (Harry's River Below Highway Bridge) were used for model simulation (Table 3.2). Compared with station Stephenville RCS and Black Duck, climate station of Stephenville Airport is the only gauge that used to generate Intensity-Duration-Frequency (IDF) estimations due to sufficient historical records. Harry's River Below Highway Bridge station (02YJ001) is the nearest hydrometric gauge with long-lasting records from 1969. There is no gauges within the simulation area for calibration, except the one station used as the upstream boundary. Therefore, we used a few observation points along the river channel obtained from (Government of Newfoundland and Labrador, 2012) corresponding to 25th September 2010 and 3rd November 2010 to calibrate the model.

Table 3. 2 List of climate stations and hydrometric station

STATION ID	STATION NAME	DATA	RECORDS LENGTH
8403800	Stephenville Airport	Precipitation	1953 – present
8403820	Stephenville RCS	Precipitation	2008 – present
8400570	Black Duck	Precipitation	1981 – 2004
02YJ001	Harry's River Below Highway Bridge	Water Level & Flow	1968 – present

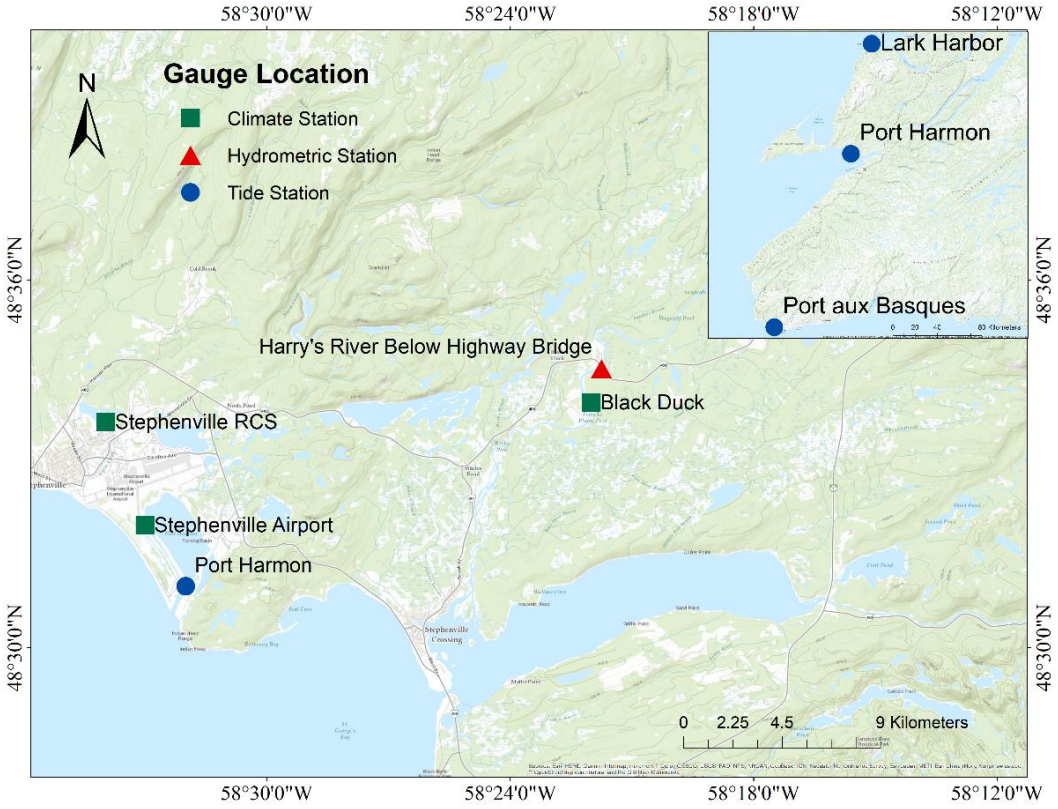

Figure 3. 5 Location of all available gauges (climate station – green rectangular; hydrometric station – red triangular; tide station – blue dot)

3.2.3 Tide Data

There are three tide stations close to Stephenville Crossing: Port Harmon, Lark Harbor, and Port aux Basques (Figure 3.5). Hourly tide predictions and observed water levels are available at these gauges , and can be obtained from Fisheries and Oceans Canada (Table 3.3). The nearest station is Port Harmon, which is located on the coast between the towns of Stephenville and Stephenville Crossing. Station Port Harmon provides daily tide predictions and a short-period tide observation, which only lasts a few months. The second nearest station is Lark Harbor, approximately 70km north of the study area. It has longer tide observation records from year 1963 to year 1988, However, there is no tide prediction available here. The farthest station is Port aux Basques, which is located at the south of the study area with sufficient long-lasting tide observations. The cyclic rise and fall of seawater is called tide, which is caused by gravitational attraction between the moon, the sun and the Earth oceans (Sumich, 1996). All ocean areas should experience two high tides and low tides every tidal period and tides will move westwards ideally without the block of continents. Therefore, large continents would block the water movement and then tidal patterns would be changed at varied locations. Two major types of tide pattern are observed in Canadian shoreline: semidiurnal tides along eastern coastline and mixed-semidiurnal tides along western coastline (Pidwirny, 2006). A semi-diurnal tidal cycle represents similar heights of two high tides and two low tides each day, while mixed-semidiurnal tidal cycle has different sizes.

Tide predictions table are estimated based on the information of Reference ports and Secondary ports. Tidal heights, extremes and mean water levels are available for Reference ports, while Secondary ports have the information of time and tidal heights differences. The tide predictions at

Secondary ports are estimated from the addition or subtraction from the times and heights of Reference ports (Fisheries and Oceans Canada, 2020). Surge can be estimated by calculating the difference between water level observations and tide level predictions.

Table 3. 3 List of climate stations and hydrometric station

STATION ID	STATION NAME	TIDE OBSERVATIONS
2710	Port Harmon	1968 – 1968
2685	Lark Harbor	1963 – 1988
665	Port aux Basques	1935 – present

3.2.4 Climate Change Data

General Circulation Model (GCM) is a numerical model that simulates physical processes in the ocean, land surface, and Earth's atmosphere. Perez et al. (2014) evaluated the performance of GCMs over the north-west Atlantic region through analysis of their similarity, variability, and consistency. The study area included the town of Stephenville Crossing, therefore we selected GCMs according to the evaluation of this research. Nine GCMs were chosen for climate change impact analysis: ACCESS1.0, HadGEM2-CC, HadGEM2-ES, GFDL-CM3, MPI-ESM-LR, HadGEM-AO, CSIRO-Mk3.6.0, GFDL-ESM2G, and CanESM-2.

Daily minimum temperature and maximum temperature of statistically downscaled GCMs are obtained from the Pacific Climate Impacts Consortium (PCIC, https://www.pacificclimate.org/) during the period of 1950 - 2100. In general, the spatial resolution of GCM is in the range of 100 - 300km, but the resolution of PCIC's downscaled climate data is 300 arc-seconds, which is roughly 10km. Representative Concentration Pathway (RCP) 4.5 and 8.5 were chosen in this study to represent different greenhouse gas emission pathways in the future. RCP 4.5 refers to a stabilized scenario before year 2100, whereas RCP 8.5 means an increasing trend of greenhouse gas concentration over time.

3.2.5 Intensity-duration-frequency (IDF) curve

Intensity-Duration-Frequency (IDF) curves describe the relationship between rainfall occurrence frequency and rainfall intensity under multiple durations (Figure 3.6). The development of IDF curves requires the support of sufficient historical records from climate station. Tipping bucket rain gauge data is fitted into the selected distribution function to generate the maximum rainfall intensity for each duration and return period. For example, the 2007 IDF of climate gauge of Stephenville Airport was generated based on 39-years of gauge data from 1967-2007. Each line in the graph represents specific return levels, ranging from 2 years to 100 years with a various duration from 5min to maximum 24hrs. Through the diagram, the rainfall intensity value can be found for further engineering applications. Besides, the fitted equations and total precipitation table at Stephenville Airport can be obtained from Environment Canada. Currently, the intensity-duration-frequency curve is an essential tool for engineering and infrastructure design, such as storm-water ponds and sewers. Canadian Standard Association (CSA) group indicates the

importance of development and application IDF curves for current and future conditions, as it improves the understanding of local extreme rainfall patterns and helps with engineering designs due to urbanization or climate change. In this study, IDF curves are required to generate storm designs as the inputs to the hydrological model. Under the climate change impact analysis, IDF curves will be updated for future scenarios, therefore the changes in hyetographs cause the changes in flooding simulations in the next step of hydrologic and hydrodynamic modeling.

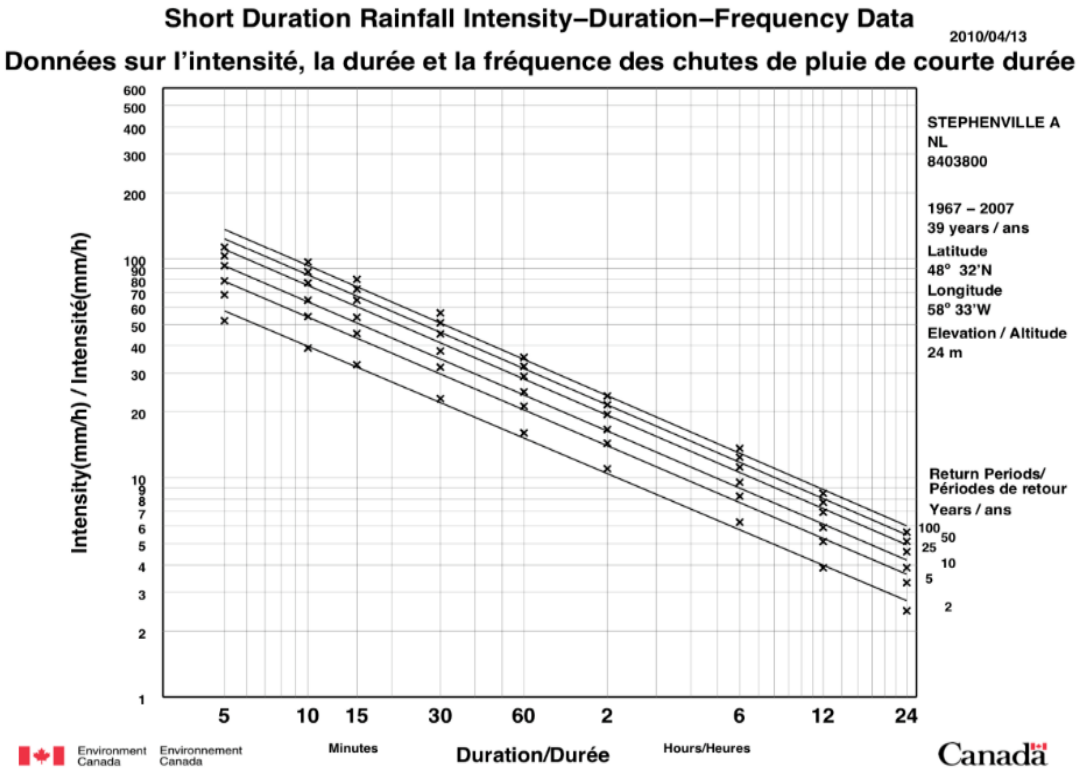

Figure 3. 6 Rainfall Intensity-Duration-Frequency curve 2007 (Environment Canada, 2010)

3.2.5 Sea Level Rise

Climate change is expected to increase the global sea levels through glacier melting and thermal expansion of sea water. The risk of coastal flooding is increasing as the direct consequence of sea level rise. With increasing urbanization, the population and economy is growing in coastal low-lying areas globally, which makes the cities and communities more vulnerable to coastal flooding. Batterson et al. (2010) studied the past and future sea level change in Newfoundland and Labrador and estimated a local trends of sea level for different zones of province. The effects of land subsidence and global sea level rise are superimposed as the results of local sea level rise in this study. The projected local ground subsidence rate is 2 mm/year for the main area of Newfoundland Island (Tarasov and Peltier, 2004). The study shows the sea level rise in Newfoundland Island is more significant than Labrador, especially in south areas of Newfoundland. The sea level trends in Stephenville Crossing is projected to increase by 30cm and 80cm by 2050 and 2099, respectively (Batterson, 2010). The increase in local sea level is considered for the simulation of coastal flooding and compound flooding in climate change impact analysis.

Chapter 4 Methodology

4.1 Intensity-Duration-Frequency (IDF) curves and Design Storms

4.1.1 IDF curves

Rainfall intensity-duration-frequency (IDF) curves are essential for the design and maintenance of sewers, stormwater ponds, catchment basins, among other various types of engineering infrastructures. Municipal design in Canada highly relies on IDF curves as it can help with the design, operation, and maintenance of infrastructures. In addition, water resources management is dependent on the IDF curves, as it provides critical estimates of extreme rainfall events for flood control and water supply (Canadian Standards Association, 2012). The local IDF curves can be represented in functions based on different empirical approaches such as:

Sherman's formula: $i(t) = \frac{a}{(t+b)^c}$ $(Equation\ 4.1)$

Bernard's formula: $i(t) = \frac{a}{t^b}$ $(Equation\ 4.2)$

where i (mm/h) is the rainfall intensity at specific storm time t (hour), and a, b and c are parameters for each return period. IDF curves generated by Environment and Climate Change Canada adopt Bernard's equation, while Gutierrez-Lopez et al. (2019) adopts Sherman's equation. The IDF curve for the study area is generated based on local rainfall data that are collected from nearby gauge station.

Rainfall hyetographs or design storms represent the temporal pattern of precipitation, which is required as input data for hydrological simulation and flow routing. The resulting flow hydrographs at a specific point can be used as the inputs to the hydrodynamic model for flood analysis. Design storms can use the precipitation records at a specific point or other types of rain data over the study region. Rainfall patterns can be obtained from local historical precipitation events or be constructed by a statistical approach. There are various methods to generate design storms, such as the triangular method, alternating block method, instantaneous intensity method, and more (Chow et al., 1988). The triangular method and linear/exponential method are not adopted in this research because they are more suitable for 6-hour and 1-hour storm events, respectively. Three approaches used in this study are the methods of SCS and Huff, and Alternative Block Method (ABM). The required input parameters and procedures to generate hyetographs by using two methods are described in detail. Besides, the features and limitations of design storm methods and how design storms can affect further model simulations are discussed.

4.1.2 Design Storms

Method of SCS

Method of Soil Conservation Service (SCS) can capture the rainfall patterns with the maximization of peak rainfall. SCS rainfall distribution was developed in 1986 and applied for a single storm event with 6- or 24-hour duration across the U.S. Four different distribution types are generated based on the data in multiple areas. Stephenville Crossing belongs to the Atlantic coast, so SCS curve Type III is applied to generate the design storm. Curve numbers (CN) and depth of storm are required in SCS curve generation. Curve number represents the basin’s capacity in

imperviousness and absorption, is calculated based on land use map, soil types, and hydrologic conditions. Curve number is typically used in hydrologic studies to estimate rainfall-runoff response, and rainfall excess can cause direct runoff or infiltration based on varied CN. This simple method is widely used in engineering designs of dams and urban facilities, among others. Notably, the limitation of SCS method is the designed duration of storm event because the curves are only applied for storm events up to 24 hours.

a. Required Information:

1. Storm duration (24 hours)
2. Design return periods (25 years and 100 years)
3. Distribution type (Type III is used for Atlantic coast)
4. Total rainfall amount (calculated from IDF curves)

b.Steps to generate hyetographs:

1. Calculate total precipitation for a given duration and return period
2. Apply the SCS curve to get cumulative precipitation
3. Calculate increments between each time step
4. Plot precipitation versus time

Method of Huff

The procedure in the Huff method is similar to the SCS method, as they both use a standardized distribution type to describe rainfall pattern. However, method of Huff provides more flexibility because there is no restriction in the duration of design storms, while SCS method is only suitable for storm events up to 24 hours duration. Huff method was developed based on approximately 300

storms with durations ranging from 3 to 48 hrs. Four types of distribution curve describe the relationship between cumulative fraction of precipitation and storm time, and the timing of peak intensity varies between each types. The distribution is chosen based on the duration of designed storm. The drawback of hyetographs generated by Huff method is that it may lose the rainfall features, like extreme peak intensity because it flattens the peak of precipitation during a event.

a. Required Information:

1. Storm duration (24 hours)
2. Design return periods (25 years and 100 years)
3. Quantile distribution type (Type III is used for 12-24 hours storm duration)
4. Total rainfall amount (calculated from IDF curves)

b. Steps to generate hyetographs:

1. Calculate total precipitation for the given duration and return period
2. Apply the Huff quantile curve to get cumulative precipitation
3. Calculate increments between each hour
4. Plot precipitation versus time

Alternative Block Method (ABM)

The precipitation pattern produced by Alternating Block Method maximizes the depth rainfall intensities for all different storm durations by using the function of IDF curves. The duration of storm event and the time step of hyetographs are chosen first. Contrary to the two methods with different distributed curve, a single theoretical rainfall pattern is generated by this method, which is the drawback of ABM. Method of Huff and SCS have variations in the time of peak rainfall by choosing different distribution curves, however, ABM method always generates the peak rainfall

at the middle of storm event. Design storms based on projected WRF-IDF curves are updated in two ways resulting in two types of hyetographs generated with Alternative Block Method for comparison and discussion. One way is to apply constant temperature scaling rate to the whole event; while another way is to apply varied temperature scaling rate to each time step.

a. Required Information:

1. Storm duration (24 hours)
2. Design return periods (25 years and 100 years)
3. Time interval (1-hour increment for 24 hours event)
4. Equation expression of IDF curves

b. Steps to generate hyetographs:

1. Calculate precipitation (mm) of different duration with corresponding rainfall intensity (mm/hr)
2. Calculate increments of precipitation amount between each time interval
3. Place the highest precipitation increment (maximum block) in the middle of the hyetograph. Place the second-highest increment to the right of the maximum block, and then place the third-highest increment to the left of the maximum block, and so on until the last block is placed.

4.2 Hydrologic and Hydrodynamic Modelling

This study utilizes the Hydrologic Engineering Center-Hydrologic Modeling System (HEC-HMS) hydrologic model and Hydrologic Engineering Center-River Analysis System (HEC-RAS) hydraulic model to characterize compound flooding and estimate the potential flood inundation

area along the river and urban domain. These two models were developed by the U.S. Army Corps of Engineers (USACE) and have been widely applied for flood hazard modeling, as discussed in the literature review section. As part of the Newfoundland and Labrador flood risk mapping program, HEC-HMS and a 1D HEC-RAS models have been calibrated and validated against observed water levels for Stephenville Crossing to ensure that they accurately simulate the hydrologic and hydraulic response of the watershed.

4.2.1 Hydrologic Model

The HEC-HMS model simulates the drainage basin of Harry's River up to Black Duck Siding, and consists of 33 sub-basins, 10 river reaches, and 17 junctions. Junction 11 represents the hydrometric gauge of 02YJ001, Harry's River below highway bridge (Figure 4.1). For each reach, the required inputs of channel characteristics, which include the length and slope of channel and Manning's n coefficient. All reaches are set as trapezoid shape, and the slopes of reach are varied between 0.001 (reach 3 and 4) and 0.025 (reach 13) with the same Manning's n value of 0.04. Loss method, transform method, and base-flow method are chosen for each sub-basin to simulate rainfall-runoff process: U.S. Soil Conservation Service (SCS) Curve Number, SCS Unit Hydrograph and Constant Monthly, respectively. Related parameters are Curve Number, impervious rate, lag time and monthly base-flow rate. Curve Number represents the basin's capacity in imperviousness and absorption, and a weighted Curve Number is estimated for each sub-basin based on soil group and land use type. Then lag time is determined based on empirical formula involving Curve Number, sub-basin slope, and travel distance. All sub-basins and reaches need to be connected to a downstream junction, and junction needs to be connected with its

downstream reach. Specific hyetograph is chosen as precipitation inputs in flow simulation without the consideration of evapotranspiration and snowmelt. The Muskingum-Cunge routing method is improved from classic Muskingum method by Cunge in 1969 and is utilized for flow routing in HEC-HMS. The parameters of routing method are estimated from channel morphology, such as roughness coefficient and cross-sectional characteristics of channel. Although the climate station, Black Duck, is available inside the modelling watershed, only daily measurements were recorded from 1981 to 2004. The short recording length and coarse precipitation data mean this station may not be an optimal choice to simulate the short-duration runoff response. Rainfall inputs are collected from the nearby climate station, Stephenville Airport, which has the most complete and longest records of historical rainfall from 1953 until the present. To use the rainfall gauge data in hydrologic model, an areal reduction factor of 0.9 is used on precipitation inputs, hyetographs.

The model was calibrated with measured hydrographs in December 1990 event and validated with June 1995 event and September 2005 event (Government of Newfoundland and Labrador, 2012). Model parameters are generated through geographic information system (GIS) analysis are fixed for all simulations. During event calibration and validation, base-flow is estimated from flow records at hydrometric gauge (02YJ001) before the date of the simulation event. The calibration results of event December 1990 show a well match between simulated flow peak and observed flow peak, but there is a few hour timing difference between peak flow, which may be caused by the basin response time or assumed reduction factor of precipitation inputs. Simulated results of validation events would match the observations after an adjustment of Curve Number, and the hydro-technical study report also indicates it would be better to have available precipitation data within this watershed for event reproduction (Government of Newfoundland and Labrador, 2012).

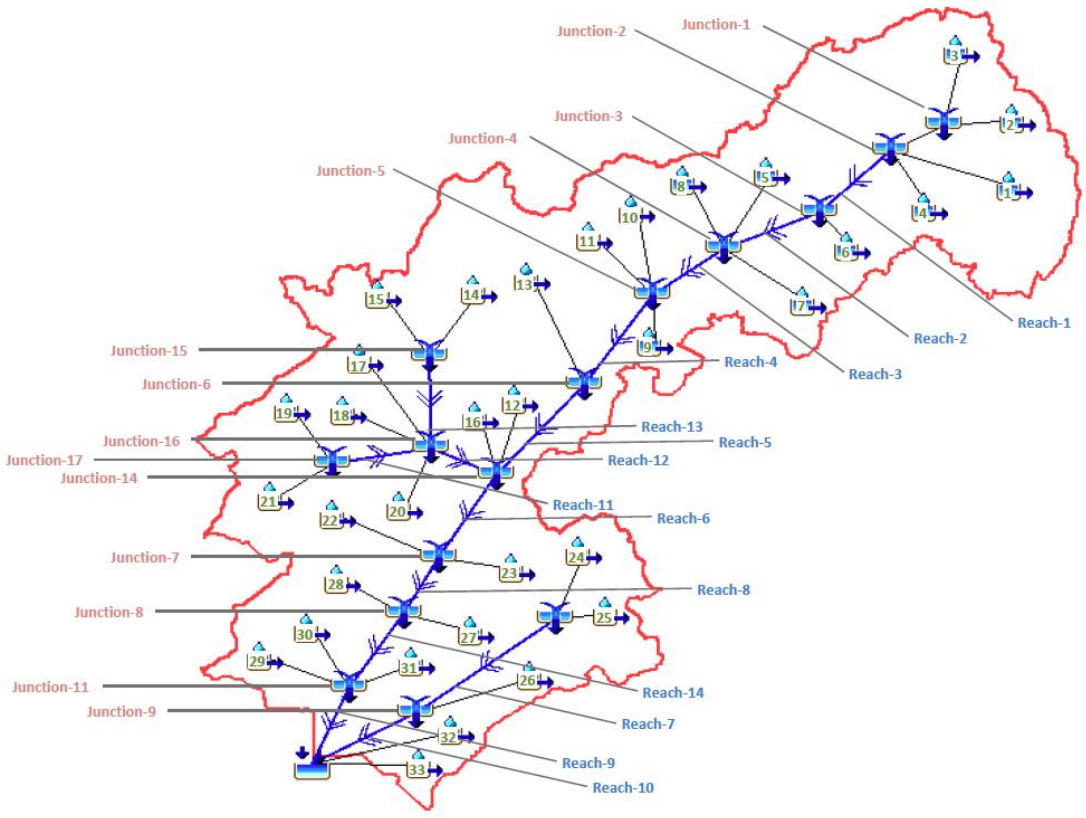

Figure 4.1 Overview of the HEC-HMS model (Government of Newfoundland and Labrador, 2012)

4.2.2 Hydrodynamic Model

The one-dimensional HEC-RAS represents the riverine systems through a series of one-dimensional cross-sections, and the water depth is calculated at each cross-section based on the boundary conditions including the upstream flow hydrographs generated from the HEC-HMS model. The 1D HEC-RAS model that is set up for Stephenville Crossing simulates river flow from the lower downstream of Harry's River to Main Gut. Eleven surveyed bathymetric cross-sections across the reach were used to describe the channel geometry and floodplains (Fig 4.2). Roughness coefficients of channel and floodplain were estimated based on the type of channel and overbanks. HEC-RAS model is forced by the flow hydrograph as the upstream and stage hydrograph as the

downstream boundaries. It was assumed that the flow hydrograph has a triangular shape with a peak discharge obtained from HEC-HMS. The assumption of a simple triangular shape of the flow hydrograph might not represent the actual flooding conditions, accurately therefore it was not considered in the 2D model setup. The unsteady flow analysis was performed by solving a dynamic wave equation to route the inflow through the reach and generate time-varying water surface profiles. The 1D HEC-RAS model was calibrated based on several water level measurements at cross-sections of 10-12, 14 and 16-17 during the simulation from 25th to 28th September 2010 and validated based on the November 2010 event, from 3rd to 7th November. Results show that the simulated depths fall within the expected range of water levels (Government of Newfoundland and Labrador, 2012).

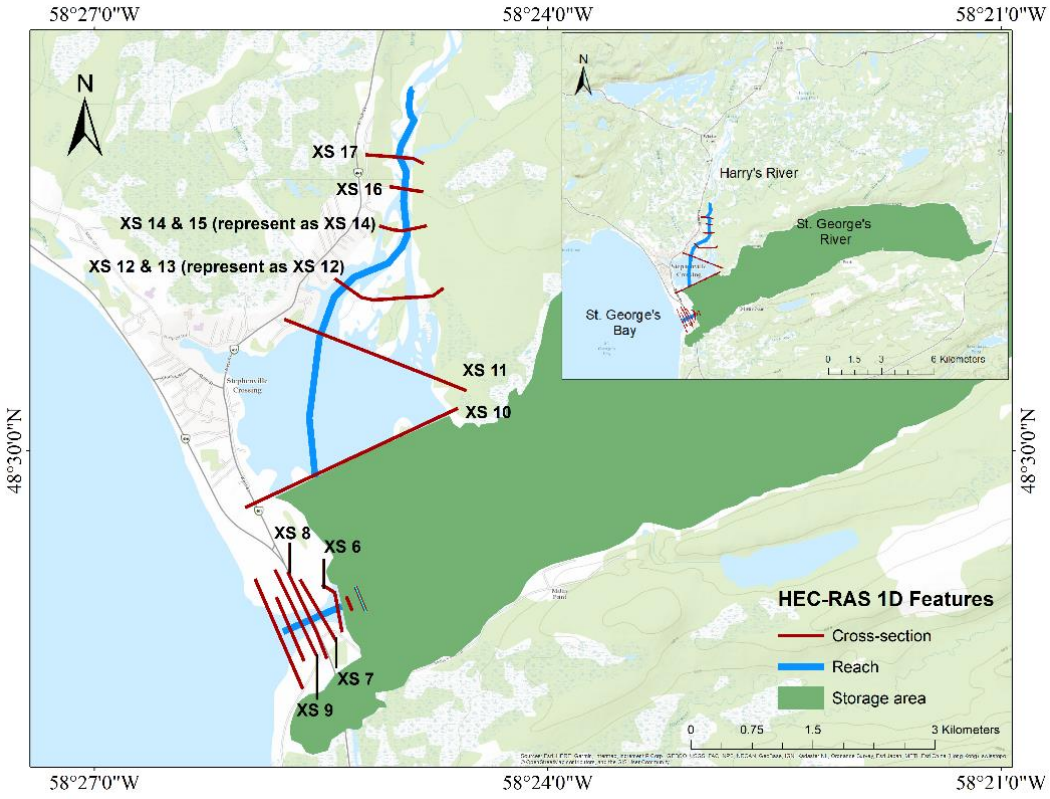

Figure 4.2 Geometric features in the HEC-RAS 1D model (cross-section –red line; river reach – blue line; St. George's River – green)

With the advancement of computation resources and improvements of hydrodynamic models, the 2D HEC-RAS model is recently developed and released. The two-dimensional HEC-RAS represents floodplain flow as a 2D cell, by assuming the third dimension of water depth is relatively shallow. The conservation of mass and of momentum equations are expressed as follow:

$$Mass\ Conservation\text{:}\ \frac{\partial H}{\partial t}+\frac{\partial (hu)}{\partial x}+\frac{\partial (hv)}{\partial y}+q=0 \qquad (Equation\ 4.3)$$

where t is time, *x* and *y* represent spatial dimensions, the 2D vector (u,v) represents the velocity components in two dimensions, q is flux, H is water surface elevation, and h is water depth (US Army Corps of Engineers, 2016).

$$Momentum\ Conservation\text{:}$$

$$\frac{\partial u}{\partial t}+u\frac{\partial u}{\partial x}+v\frac{\partial u}{\partial y}=-g\frac{\partial H}{\partial x}+v_t\left(\frac{\partial^2 u}{\partial x^2}+\frac{\partial^2 u}{\partial y^2}\right)-c_f u+fv \qquad (Equation\ 4.4.1)$$

$$\frac{\partial v}{\partial t}+u\frac{\partial v}{\partial x}+v\frac{\partial v}{\partial y}=-g\frac{\partial H}{\partial y}+v_t\left(\frac{\partial^2 v}{\partial x^2}+\frac{\partial^2 v}{\partial y^2}\right)-c_f v+fu \qquad (Equation\ 4.4.2)$$

where t is time, u and v represent velocity components in x and y directions, g is the gravitational acceleration, c_f represents the bottom friction, f is the Coriolis parameter, and $v_t$is the horizontal eddy viscosity coefficient (US Army Corps of Engineers, 2016).

Setting up the HEC-RAS 2D model

DEM, channel bathymetry, and land cover map with spatially-varied roughness are required to set up the model. A 1m-resolution LiDAR product is available for the urban area of Stephenville Crossing however, the coverage of this data is insufficient to build the 2D model for the watershed. The 20m-resolution Canadian Digital Elevation Model (CDEM) covers the watershed area and has a relatively better resolution than other global DEM products, therefore it is used to represent the

terrain's topography. DEM does not include the bathymetry details under the water surface, therefore cross-sections are interpolated into a surface profile and then fused into the CDEM data. Additional 40 surveyed cross-sections are created in ArcGIS and then be imported into HEC-RAS at the upstream of simulation reach (Fig 4.4). With the help of the details of additional 40 cross-sections, the interpolated channel bathymetry is sufficient to cover the simulated reach, and then bathymetry data is fused into original DEM data. There is no local land use map available with fine resolution, therefore the global land cover map with 20m-resolution is used in this study to generate the spatially-varied Manning's n values for every pixel. Table 3.1 lists all types of land cover in the study region with corresponding roughness coefficients. The area of the main channel is delineated to substitute the original pixels in the land cover map because roughness coefficients would be slightly different for channel and water. The manning's n for channel remains the same with the 1D HEC-RAS model, which is 0.035 for the reach along Harry's River.

After preparing DEM data, the 2D mesh area is delineated in Geometric Data Editor of HEC-RAS, and the simulation is conducted within this region with specific cell size. Smaller mesh size can capture the terrain features in high resolution however it requires more computational time. The determination of cell size is not only dependent on the scale of the study region and the objectives of the analyses but also dependent on the resolution of DEM used in the model. A very fine simulation cell is not reasonable to consider for a model with coarse-resolution DEM. Therefore, we set up the 2D model considering a 20m x 20m cell size consistent with the 20m-resolution DEM. In addition, the break-lines are added along the river centerline and right and left of the overbank. The cell size around the break-line can be refined into relatively smaller irregular meshes, as it can provide more accurate simulation for channel and overbank area with less

computational time. It is noted that the difference in the sizing of cells between 2D flow area and the break-line area could not be very large, as the maximum allowable faces of cells are eight in HEC-RAS setting. A relatively small-sized cell surrounding with larger-sized cells would exceed the limitation of the number of cell faces.

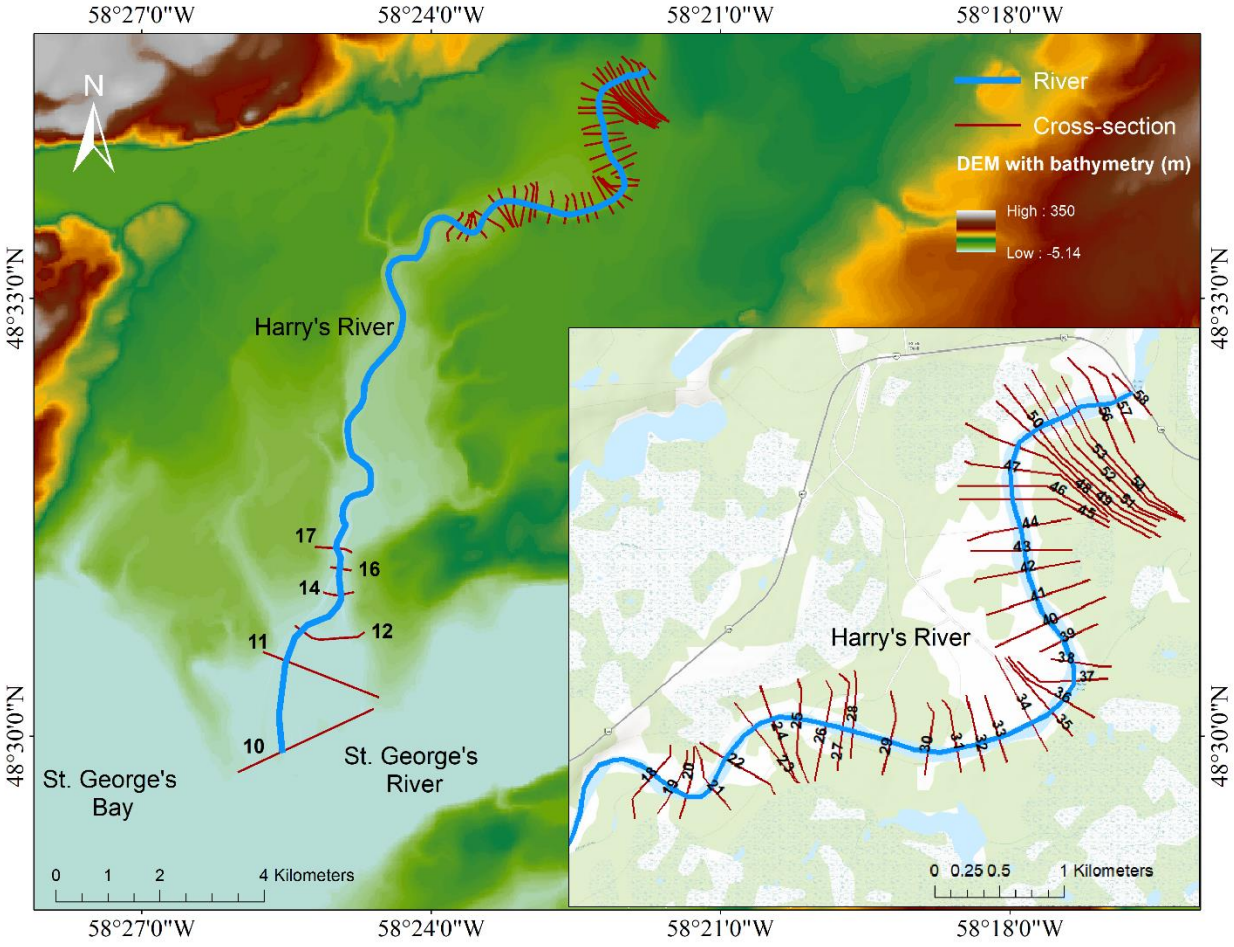

Figure 4.3 Additional surveyed cross-sections (red line) with bathymetry-fused DEM

HEC-RAS 2D model constructed for Stephenville Crossing extends the location of the upstream boundary to the location of hydrometric gauge, Harry's River below Highway Bridge (Figure 4.2

and Figure 4.3). The 2D model is forced by simulated flow hydrographs as the boundary condition and coastal stage hydrographs as the downstream boundary condition. Due to missing bathymetry information at the mouth of Harry's River, two downstream boundary conditions are set-up along the coastline (outer of Main Gut) and estuary (inner of Main Gut), separately. Main gut is the connection point between St. George's River and St. George's Bay, the outer of Main Gut represents the bay region and the inner of Main Gut represents the river region. The coastal downstream boundary condition is constructed with hourly tidal predictions, which are collected from the tide gauge at Port Harmon which is an active station close to St. George's Bay.

A calibrated HEC-RAS 1D model is utilized to validate the stage hydrographs of the inner downstream boundary condition of HEC-RAS 2D, to make sure the adjustment is reasonable and accurate. The temporary HEC-RAS 1D model uses the same downstream boundary conditions as the original HEC-RAS 1D model. Calibrated original HEC-RAS 1D model is the only relatively reliable source that can provide time-series data for model adjustment. For historical event simulation, the flow hydrographs of upstream boundary conditions are obtained from HEC-HMS simulations at Junction 11, which is the location of a hydrometric station of Harry's River below Highway Bridge (Location of gauge, see Figure 3.1; Location of the junction, see Figure 4.1).

Models and related input data used in this study are demonstrated in Figure 4.4. Rainfall hyetographs generated based on IDF curves are precipitation inputs in hydrologic model (HEC-HMS). After the simulation of HEC-HMS, flow hydrographs are obtained and used as the

upstream boundary condition in hydrodynamic model (HEC-RAS). Enforced with downstream boundary condition, tide prediction, the model can simulate the channel flow characteristics.

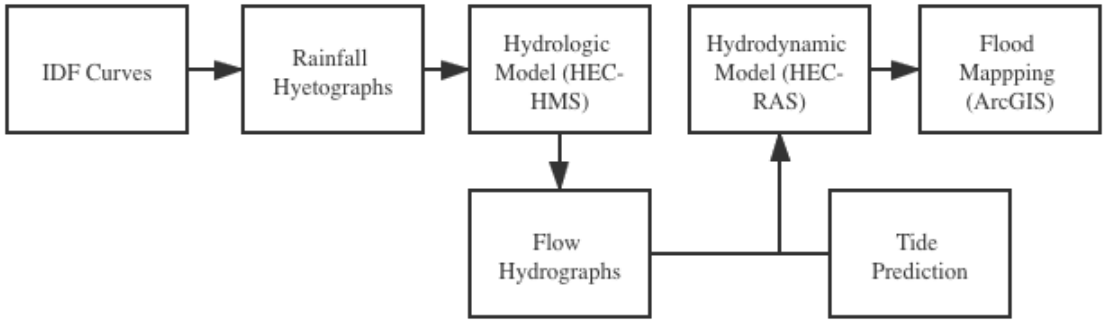

Figure 4.4 Flowchart of models and related inputs

4.3 Satellite Imagery

With the advancement of remote sensing technology, satellite images can capture terrain features in different resolutions. The flood inundation map generated from satellite imagery is also used to evaluate model performance. European Space Agency (ESA) conducted the Sentinel-1 mission to provide enhanced revisit frequency and coverage of interferometry capability. The satellite covers the entire world's land at different frequencies, for example, bi-weekly for sea and ice zones, and daily frequency for European coastal regions (ESA, 2020). The first Sentinel satellite was launched in 2014, and the second one was launched in 2016, so it does not include the data corresponding to the 25th September and 3rd November 2010 event. A flood event in January 2018 is selected as another validation event by comparing it with the Sentile-1 image.

Long et al. (2014) proposed the method of change detection and thresholding to extract flood extent mapping with Sentinel-1 images. This method identifies the changes between flood event image and normal condition image by comparing the differences in brightness information. Multiple images represented normal conditions without any flooding would be combined as the final reference image (Table 4.1). River volume generally varies between seasons, therefore it would be better to choose the images within the same season of the flood event. Therefore the images used as reference image is taken from 8th January 2017 to 20th January 2019 for the potential flood event of 14th January 2018. For flood mapping studies, HH polarization of transmitter-receiver is generally considered as a preference than other polarizations (Henry et al., 2006; Gan et al., 2012; Twele et al. 2016). A reference image is generated by taking the median of all available selected images. Speckle noise is granular salt and pepper that existed in synthetic aperture radar (SAR) images due to random interference (Pasmurov and Zinoviev, 2005). A speckle filter is applied for both reference and flood images to remove speckle and improve the smoothness of the image with reduced resolution and blurred features. Senthilnath et al. (2013) evaluated different speckle filters (Lee filter, Frost filter and Gamma MAP filter) in flood extent extraction from Sentinel-1 C band image. Gamma MAP filter is based on Bayesian analysis and Gamma distribution, and the results show it has better performance in this study area. After applying the speckle filter, the difference between the two images was calculated as the difference image. Most of the above processes are conducted in Google Earth Code Editor, including image collection, reference image calculation, and difference image generation. Speckle removal is completed through multiple types of filters in Sentinel Application Platform toolbox (SNAP). The difference image is filtered based on a threshold in geographic information system (ArcGIS) to identify the actual flooded area.

Table 4. 1 List of satellite images including reference images and flood image

Satellite	Image type	Image Date	Resolution (m)	Mode	Polarization
Sentinel-1A	Reference	20171208	10	IW	HH
		20171220			
		20180101			
		20180125			
		20181215			
		20181227			
		20181204			
		20190108			
		20190120			
	Flood	20180114			

4.4 Projected IDF Curves

4.4.1 Projected WRF-IDF curve

Currently, IDF curves are generated based on historical rainfall observations indicating that the historical variations can represent the future climate system. However, this stationarity assumption might not be valid because the future rainfall patterns are projected to change. Therefore, the current IDF curves may not be adequate to represent future events in a changing climate. It is important to assess the impacts of climate change on IDF curves for future infrastructure design and planning, and water resources management.

The approach used in this chapter to update IDF curves for climate change analysis is based on high-resolution WRF-simulated precipitation. Weather Research and Forecasting (WRF) system

is a numerical weather prediction model designed to simulate meteorological processes and provide weather forecasting, as well as for climate change analysis (Cannon et al., 2019). WRF can produce simulations based on actual atmospheric conditions or idealized conditions, across scales from tens of meters to thousands of kilometers. Many studies have assessed the ability of WRF model in convective or non-convective rainfall simulations, and the results show that it can adequately represent the features of rainfall events (Kouadio et al., 2020, Mugume et al., 2017). For example, Knist et al. (2020) applied convection-permitting WRF simulations, at a spatial resolution of 4km and hourly temporal resolution, for the analysis of extreme precipitation changes in Europe. Cannon et al. (2019) expressed the projected precipitation for different return levels based on relative changes of temperature (i.e. temperature scaling) and assessed the adherence to the theoretical Clausius-Clapeyron (CC) relation. Under theoretical CC relation, the water can hold approximately 7% of air rise capacity for every 1K warming of air temperature (Pall et al., 2007; Schneider et al., 2010). Singh et al. (2020) studied the relationship between temperature and precipitation over Canada, and the results show sub-CC scaling rate is observed in the major Canadian region, except extreme north areas. WRF CTRL represents the historical control run and PGW includes the future climate simulations using the downscaling method of Pseudo-Global Warming, which assumes the boundary condition is the composite of observation data and the differences between present and global warning conditions (Kimura and Kitoh, 2007). WRF model simulations have been conducted by Rasmussen (2017) to assess the impacts of climate change on convective population and thermodynamic environments at a relatively high resolution of 4km. The sub-daily outputs of pseudo-global-warming convection-permitting climate model were used by Cannon et al. (2019) to project changes in characteristics of IDF curves over North America. A parsimonious Generalized Extreme Value Simple Scaling (GEVSS) method is used to improve the

efficiency of model integration, and then the future changes of local-scaled short-duration extreme rainfall events are estimated. The study shows an increase in the scaling exponent of the GEVSS parameter, indicating that the return levels corresponding to the short duration rainfall events can increase to a larger extent compared to ones associated with longer duration events (e.g. 24hr).

General Circulation Models (GCMs) simulate the hydroclimatic processes in changing climate conditions to improve the understanding of climate change impacts under different future scenarios, which is represented by the Representative Concentration Pathways (RCPs). RCP 4.5 and RCP 8.5 used in this study reflect a range of possible concentration of future greenhouse gas emissions. RCP 4.5 represents an intermediate scenario that carbon emission will decline after reaching a peak around 2040, while the RCP 8.5 scenario assumes the carbon emissions will continue to rise in the future as the worst-case scenario of climate change. We study extreme 24-hour rainfall event with return periods of 25 and 100 years over the historical period (1976-2005) and two future periods of 2041 – 2070 (2050s) and 2071 -2100 (2080s).

Temperature scaling, defined as a percent change of precipitation rate per degrees Celsius, is determined for North American region with different return periods and rainfall durations. To apply the scaling rates on the IDF curve at Stephenville Crossing we first calculate the average temperature of the region over the historical and future periods based on downscaled GCMs. The scaling factor per degree Celsius is then applied to the temperature changes between future and historical periods to estimate the projected increases in rainfall events with different durations. Then a final change rate of precipitation during a period can be used to update current IDF curves. Depending on the choice of method of design storms, the scaling rate can be applied

on total rainfall depth calculated from IDF curves or rainfall intensity obtained from IDF equations. For the former, the calculated increase rate is directly applied to the total precipitation amount. For the latter, the simple way is to apply the scaling rate on the current IDF equation, which means the increase rate of each time step of a storm event is constant. Cannon (2019) indicates different durations have slightly different scaling rates, therefore another approach of applying scaling rate on rainfall intensity is to update the IDF equation with varied temperature scaling for each time step.

4.4.1 Projected GCM-IDF curve

Another approach to develop projected IDF curves (beside high resolution climate model simulations such as WRF-IDFs) is to use statistically downscaled GCM-simulated precipitation data, which might not provide robust estimates of subdaily rainfall events (Simonovic et al., 2016). In this chapter, we compare the projected flood characteristics based on IDF curves derived from GCM and WRF precipitation simulations over Stephenville Crossing. The first step in projecting IDF curves based on GCMs' precipitation simulations is to extract sub-daily maximum rainfalls (varied from 5min to 24hr) from historical observed data and daily maximum rainfalls from historical and future GCMs. The Generalized Extreme Value distribution (GEV) is fitted to the sub-daily/daily maxima using the L-moments method. Using the rain gauge data at Stephenville Crossing, an equidistant quantile-matching approach is applied to downscale precipitation data by establishing a direct statistical relationship between daily maximum precipitation simulated by the climate model (GCM; at reference period) and sub-daily historical observations. Further, it establishes the relationship between maximum rainfalls for historical and future GCM datasets.

The relative change in simulated precipitation between GCM baseline and future scenario is calculated and applied on established functional relationship between observed historical data and historical GCM data. Finally, the projected IDF curve is generated with different GCMs and RCP scenarios (Simonovic et al., 2016). The study by Cannon et al. (2019) shows the return levels corresponding to the short duration rainfall events can increase to a larger extent compared to ones associated with longer-duration events (e.g. 24hr). Therefore, the assumption that extreme rainfall events are projected to increase at the same scale for daily and sub-daily durations, considered in GCM-projected IDF curves, is called into question.

4.5 GCM Selection

General Circulation Models (GCMs) are commonly used to project future impacts of climate change on water resources (Nissen, 2001; Dibike, 2005; Najafi, 2011), flood analyses (Kay, 2009; Hirabayashi, 2013; Gao, 2020), and stormwater assessments (Semadeni-Davies, 2008; Zahmatkesh, 2015). There exists a large number of GCMs, and they represent physical processes of the atmosphere, ocean, and land by their specific representations and assumptions with the consideration of different future climate scenarios. Hence the selection of a set of GCMs is a vital step in climate change impact analysis before hydrological and hydrodynamic modelling. GCM selection without sufficient information on their quality and reliability can reduce the efficiency of water resource management and the reliability of climate change research.

The performance of each GCM is varied across different regions, and it changes for different variables. Downscaling is commonly applied to translate the GCM outputs at a coarse resolution

to regional variables at high resolution. GCM selection in this study is based on Perez (2014) who evaluated the performance of CMIP3 and CMIP5 GCMs over the northeastern Atlantic region covering the entire study area. Scatter index and relative entropy were applied to assess the skill of GCM datasets to reproduce synoptic situations, historical seasonal variability, and the consistency of GCM projections. GCM models were chosen based on critical factors for the estimation of future regional multi-model projections of surface variables driven by the atmospheric circulation in the north-east Atlantic Ocean region. Given that the study area is located in Canada, the Canadian GCM (CanESM2) is also included in this study. Accordingly, 9 GCMs were considered in this study including ACCESS1.0, HadGEM2-CC, HadGEM2-ES, GFDL-CM3, MPI-ESM-LR, HadGEM-AO, CSIRO-Mk3.6.0, GFDL-ESM2G, and CanESM2. We extracted temperature simulations from corresponding downscaled GCMs provided by the Pacific Climate Impacts Consortium (PCIC) to project rainfall extremes based on WRF-simulated IDFs through the temperature scaling approach. The features of selected GCMs are listed in Table 4.2, including resolution and simulation period.

Table 4. 2 Features of the selected GCMs

GCMS	MODELING CENTER	RESOLUTION (ATMOSPHERE)	AVAILABLE DATA
ACCESS1.0	Commonwealth Scientific and Industrial Research Organization and Bureau of Meteorology	1.25 x 1.875 degree	1950-2005 2006-2100
CANESM2	Canadian Centre for Climate Modelling and Analysis	2.8 x 2.8 degree	1850-2005 2006-2100
CSIRO-MK3.6.0	Australia's national science agency Atmospheric Research	1.86 x 1.875 degree	1950-2005 2006-2300
GFDL-CM3	Geophysical Fluid Dynamics Laboratory	2 x 2.5 degree	1860-2005 2006-2100
GFDL-ESM2G	Geophysical Fluid Dynamics Laboratory	2 x 2.5 degree	1860-2005 2006-2100
HADGEM2-AO	Institute of Meteorological Research/Korea Meteorological Administration	1.25 x 1.875 degree	1860-2005 2006-2100
HADGEM2-CC	UK Met Office Hadley Centre Carbon Cycle Model	1.25 x 1.875 degree	1950-2005 2006-2100
HADGEM2-ES	UK Met Office Hadley Centre Carbon Cycle Model	1.25 x 1.875 degree	1860-2005 2006-2100
MPI-ESM-LR	Max Planck Institute for Meteorology	1.86 x 1.875 degree	1979-2005 2006-2300

4.6 Costal Components

The individual and compound effects of riverine and coastal flooding are investigated in this study. First, the projected rainfall effects on flood characteristics are assessed and then the compounding effects of projected rainfall and coastal components (storm surge, wave, and sea-level rise) under climate change are investigated. The simulations corresponding to each scenario are conducted using the calibrated HEC-RAS model considering changes at the upstream and/or downstream boundary conditions.

We perform simulations of coastal flooding considering tidal effects as well as changes in storm surge, wave, and sea-level rise (Table 4.3). Probability density functions of water levels due to astronomic tides and atmospheric forcing are combined to generate a new frequency distribution of water levels due to all components, including tide, surge and wave (Government of Newfoundland and Labrador, 2012). High tide levels obtained from tide predictions of Port Harbor station is used to generate tidal probability density function. Although the Port Harmon is the nearest tide station, it does not have sufficient observation data for surge analysis, therefore the observed water levels obtained from gauge Lark Harbour are used to conduct a surge frequency analysis. Surge is calculated based on the difference between water level observation and tide prediction at the same time. The wave analysis involves the frequency analysis of wind data and wind hindcast. As discussed in Chapter 3, local sea-level rise (SLR) over Stephenville Crossing is retrieved from Batterson (2010) who studied the past and future sea-level changes in Newfoundland and Labrador. A triangular shape hydrograph is considered to apply the super-elevation on tide prediction graphs, consistent with Karim (2008). The worst condition is

considered assuming that the peak of surge and tide occurs at the same time. Figure 4.5 shows the downstream boundary condition estimated by imposing the triangular shape of super-elevation and constant future SLR on tide predictions.

Table 4. 3 The terrestrial and marine components considered in coastal flood assessments under climate change

Coastal Components	**Scenarios**	
Storm surge and wave (m)	25-year event	100-year event
	5.25	*6.34*
Sea- level rise (m)	2050s period	2080s period
	0.3	*0.8*

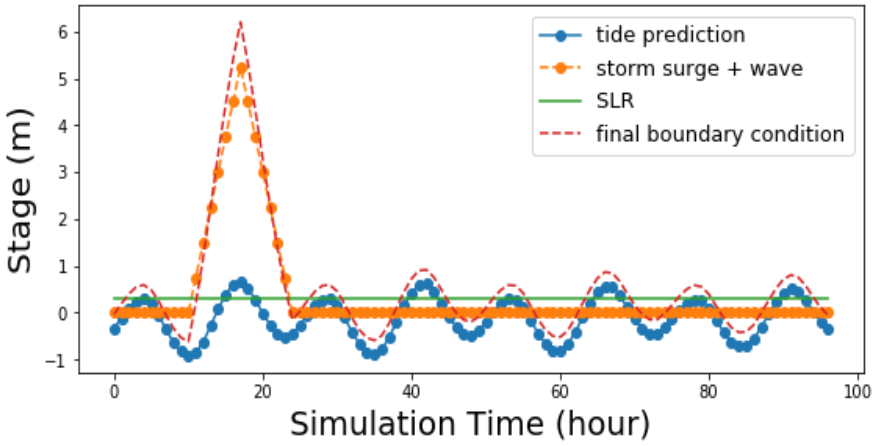

Figure 4.5 Example of coastal boundary condition with tide prediction, storm surge, wave, and future sea level rise (SLR) for 25-year event at future period of 2050s

4.7 Flood Inundation Map

Flood inundation map is commonly used for floodplain management and planning, especially in flood-prone areas. With the advancement of new technologies, the computational costs are reduced to benefit the development of flood mapping. ArcGIS extensions can be used to analyze and process hydrologic and hydraulic model results including HEC-GeoHMS and HEC-GeoRAS. The results of HEC-RAS 2D model can be directly shown in the model interface, RAS Mapper, such as the velocity, depth and the water surface elevation. Terrain data is essential for using RAS Mapper to analyze water surface profiles and floodplain boundary. RAS Mapper provides a quick visualization of simulation results for the whole area, however, a specific point needs to be chosen to view the time-series results. The flood map plays an important role to illustrate the flood risk to stakeholders in making decisions, as well as design, planning, operation and maintenance of engineering and public infrastructures. In this study, simulated maximum flood depth is equal or larger than 0.01m will be defined as inundated pixels. In climate change impact analysis, there are many climate scenarios with different RCPs, future periods, and return levels. For each scenario, different types of design storms with different GCMs are simulated. The maximum flood extent map and flood depth map of each simulation are generated through a geographic information system (ArcGIS).

Chapter 5 Results and Discussion

5.1 Introduction

Historical flood events suggest that Stephenville Crossing is vulnerable to both coastal and fluvial flooding. The population of the town is mainly concentrated in the area between the coastline and the river downstream. Besides residential properties, school, long-term care center, hospital, and many commercial properties are also located in this flood-prone region. The compound effects of river overflows, storm surge, tides, and waves can cause severe losses and damage communities and essential infrastructures. Such impacts can be more catastrophic compared to the individual occurrence of flood drivers. In this study, a two-dimensional hydrodynamic model is set-up to investigate the individual and compound effects of multiple climatic and marine drivers in a changing climate. The hydraulic model is forced by observed and simulated (using a hydrological model) river flows at the upstream and (coastal) water levels at the downstream. A calibrated hydrological model is applied to simulate the hydrological response of the river system to short-duration extreme rainfall. The two-dimensional hydrodynamic model is calibrated and validated based on water level observations and compared with simulation results of a calibrated one-dimensional model. A sensitivity analysis of the hydraulic model is conducted with varied terrain data, simulation cell size, and roughness coefficient sets. Flood inundation and flood probability maps are generated to help with the identification of flood-prone areas with higher risk.

With increases in Greenhouse Gas emissions and subsequent changes of the hydroclimate system, rainfall patterns are expected to change possibly resulting in stronger and more intense storm

events (Trenberth, 2011). The increased frequency and magnitude of short-duration extreme rainfall events can cause increases in flood occurrences and flood risks. In addition to changes in extreme precipitation events, sea-level rise and land subsidence (partly due to glacier retreat associated with global warming) are factors that contribute to intensified coastal flooding. However, there are several factors that can contribute to the overall uncertainties in the analyses including model structure, model parameters, projected IDF curves, design storm approach, and emission scenarios.

After the calibration and validation of the two-dimensional hydrodynamic model, the model is used to investigate the impacts of climate change on compound flooding. The hydraulic model is forced by hydrologic and coastal boundary conditions including the upstream river flows (hydrograph) and downstream coastal water levels. Projected temperature increases from nine General Circulation Models (GMCs) are used to update the historical intensity-duration-frequency curve based on WRF-simulated data. Results are then compared with projected IDF curves based on downscaled GCM simulated precipitation. Further, we analyze different methods for storm design, which are varied in the pattern and peak intensity of storm event. Three widely used design storms are applied in this study to generate hyetographs as the input data to the hydrological model, and the resulting flow rate is used to drive the hydrodynamic model.

5.2 Projected Impacts of Climate Change on Flood Characteristics

5.2.1 Model Performance

Adjusting the downstream boundary condition

The temporary HEC-RAS 1D model uses the same downstream boundary conditions as the original HEC-RAS 1D model for boundary condition adjustment. The simulated water levels at multiple cross-sections show the inner and outer of Main Gut have different stage hydrographs (Figure 5.1.a). There are a 2-hr time lag and magnitude reduction of peak value between outer and inner downstream boundary conditions. After the adjustment of time lag and magnitude reduction of the inner hourly tide prediction as a downstream boundary condition, the temporary-constructed HEC-RAS 1D model has been calibrated successfully to match with the results of original HEC-RAS 1D model at available cross-sections (Figure 5.1.b).

The roughness coefficients in channel and floodplain are calibrated with measurements of water surface elevation (WSE) at specific points along the channel. The results of the calibrated HEC-RAS 1D model for the September 2010 event are used for additional calibration (Figure 5.2). Since 1D HEC-RAS only simulates the lower part of Harry's River, and a limited number of results are available to be used to compare with 2D HEC-RAS simulations. Observations 1, 2, and 3 correspond to measurements taken at different locations along the cross-sections during a certain time range. For cross-section 11, 12, 14, 16 and 17, there is not a specific time for each measurement, so the horizontal line represents the duration of taking all measurements, which is

3 pm – 7 pm, September 27, 2010. As Figure 5.2 (a-e) shown, during a certain duration, the measurements of these cross-sections are the same as horizontal lines, but three observations vary between measured locations along each cross-section. For cross-section 10, the corresponding time of each measurement is available, which is 1 pm, September 27, 2010. Three observations are represented as points in Figure 5.2 (f). The simulated discharge at the location of the hydrometric gauge (02YJ011, station of Harry's River below Highway Bridge) is used as the upstream boundary condition for the HEC-RAS 2D model. 2D model simulations are consistent with the results of the 1D model, especially for peak points. For the low points, the maximum difference between 2D- and 1D-model results is about 0.1m. Water surface elevations simulated by the 2D- and 1D-model at different cross sections are compared in Figure 5.2 and Figure 5.3, and the results show the 2D simulations can match calibrated 1D simulations well, especially for the downstream cross-sections (XS10-12, Figure 5.2 d-f). Nash-Sutcliffe efficiency (NSE) is used here to assess the predictive skill, which is ranged from 0.80 at XS17 to 0.95 at XS10 (Figure 5.3). Except for XS10, 2D-model simulations of all cross-sections fall within the range of observations. Overall, the simulated 2D-model results are consistent with the 1D-model results, as well as most observation points.

The performance of the HEC-RAS 2D model is evaluated based on water level measurements. Further the results are compared with the 1D model simulations of November 2010 event, from November 3 to November 7 (Figure 5.4). We analyze the consistencies in the peak and timing of water stage hydrographs through the simulation duration. Although the first peak of WSE is not well represented in the 2D model, the remaining peaks caused by the majority of flooding impacts

are captured better compared to the 1D model. Overall, the results of 1D & 2D models are consistent and represent the observations well. The 1D & 2D simulations closely match at cross-sections 11 and 10 (downstream of Harry's River), and there are differences between observation points and 2D results (Figure 5.4 d-e), however at cross-sections 17, 16, and 14 (Figure 5.4 a-c), simulation results of the 2D HEC-RAS model closely match the observation points. WSE simulations of these cross-sections by the 2D model are higher than calibrated 1D results, and 2D results give less fluctuation.

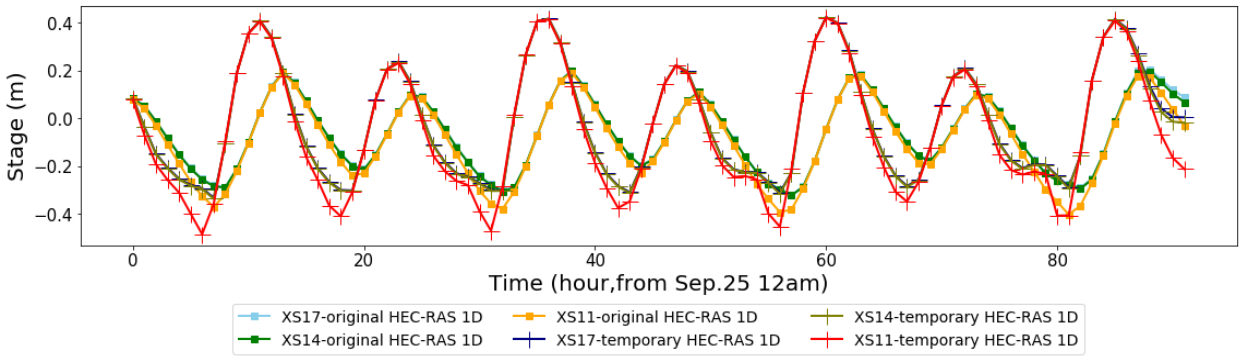

(a)

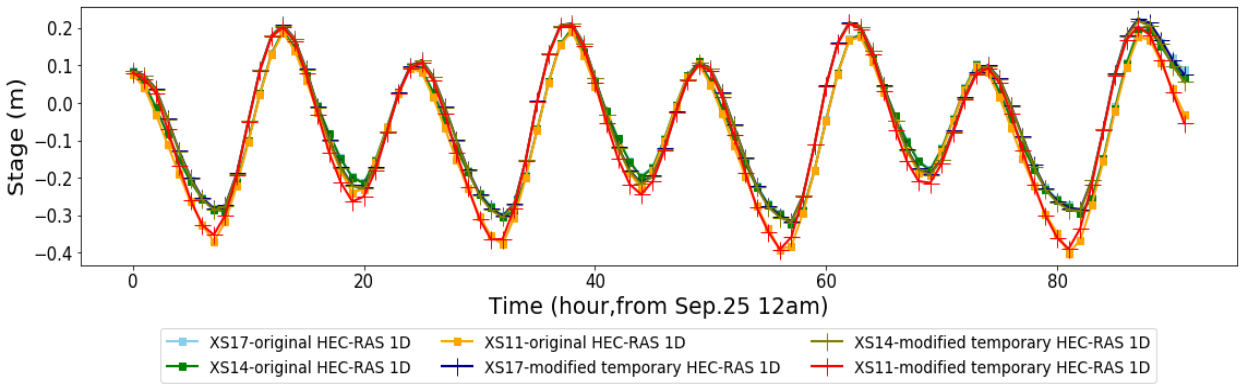

(b)

Figure 5. 1 Comparison between the simulation results of original 1D HEC-RAS and temporary 1D HEC-RAS (a. by enforcing same stage hydrograph as downstream boundary condition; b. after adjustment of downstream boundary condition in temporary 1D model)

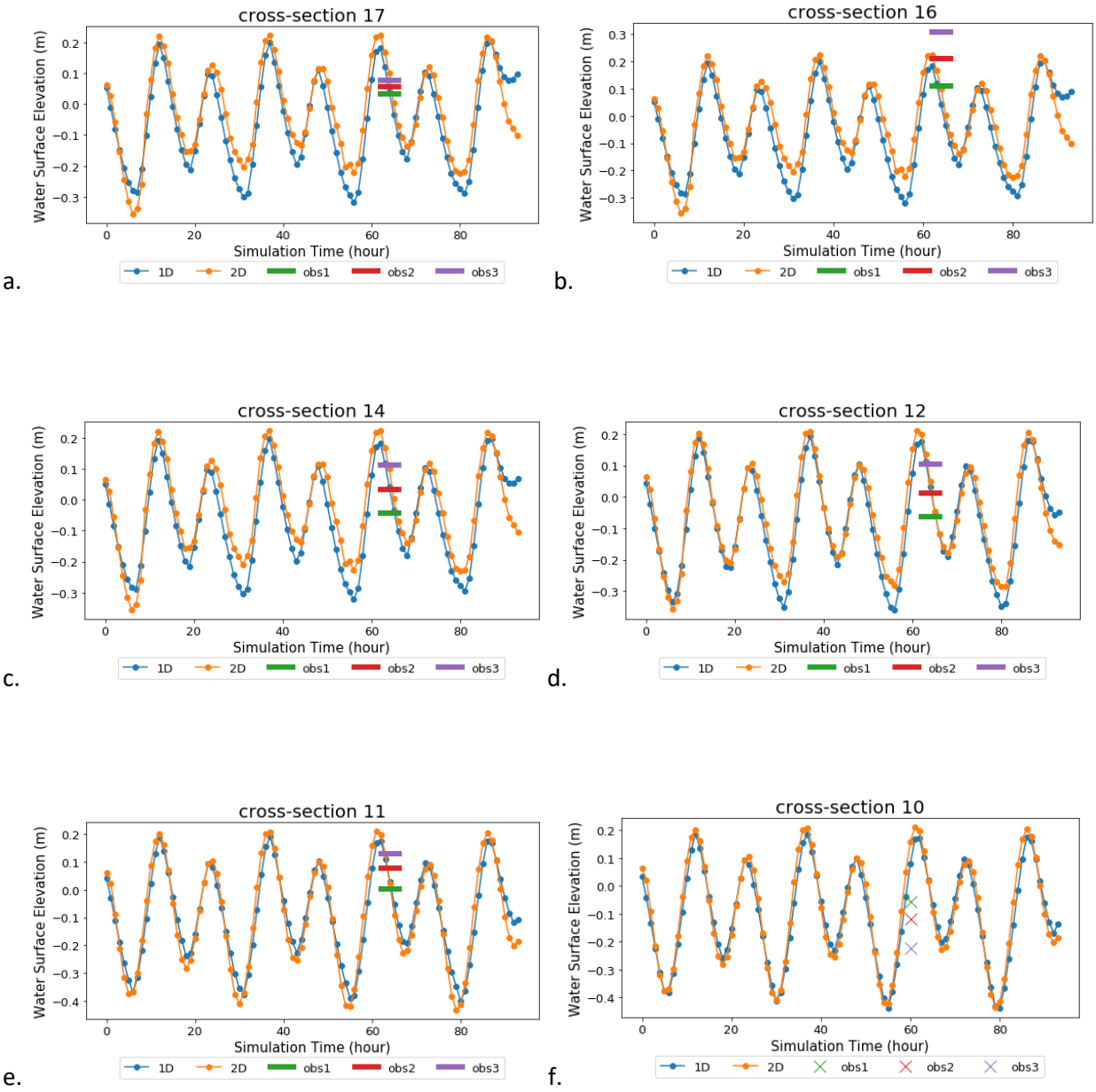

Figure 5. 2 Observed Water Surface Elevations and HEC-RAS 1D and 2D model simulations corresponding to event September 25th – 28th, 2010 at cross sections 10-12, 14 and 16-17 (shown in Figure 4.2); orange represents HEC-RAS 1D results, blue represents HEC-RAS 2D results; obs1, 2, and 3 represent observations at different locations along the cross-section during certain time range)

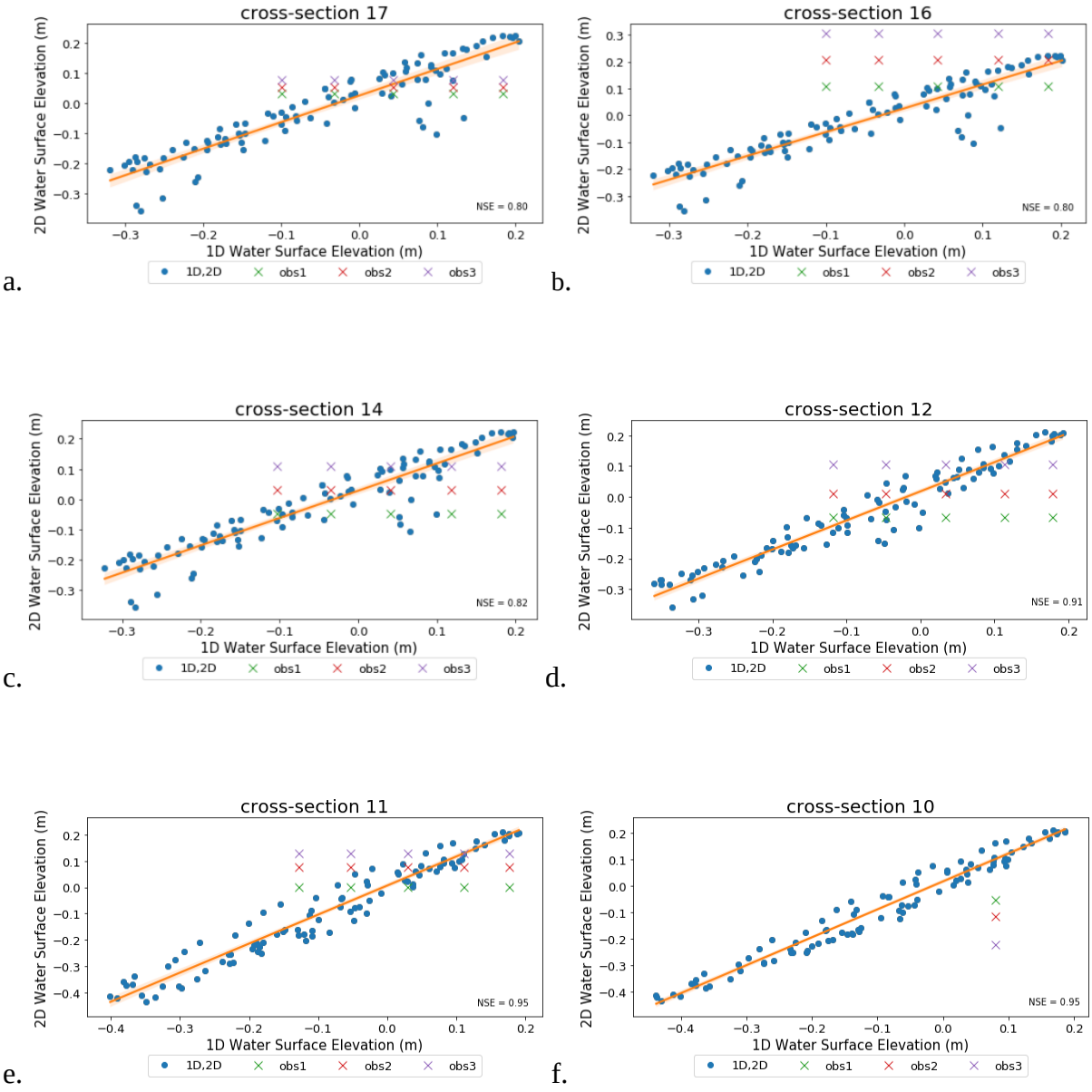

Figure 5. 3 Comparison between the calibrated-1D and 2D water surface elevations at different cross-sections along the channel (shown in Figure 4.2); observation points are also shown as cross-marker.

There are some possible reasons to cause different results between 2D and 1D HEC-RAS models. The upstream boundary location is extended up to the site of hydrometric gauge in 2D simulations. The original upstream boundary condition of the flow hydrograph in the 1D model adopts simple triangular-shape hydrographs. The peak discharge rate of hydrograph is obtained from simulation results at Junction 11 of HEC-HMS. Since the location of the upstream boundary condition of HEC-RAS 1D is relatively far away from the location of Junction 11, therefore the peak flow used in 1D model is prorated by drainage area. The time-series input hydrographs in the 2D HEC-RAS model is directly obtained from the HEC-HMS model, which is less uncertain than a theoretical flow hydrograph pattern used in 1D simulations. Due to the limited number of surveyed cross-sections along 1/3 of the simulated reach (the area between the original and extended location of the upstream boundary), the estimated bathymetry details are uncertain (the bathymetry is estimated by interpolating between two cross-sections that are far apart). Besides, the differences between 1D and 2D HEC-RAS can cause some inconsistencies in results, including the solving equations of two models and the subjective decisions made in the 1D model, such as cross-section location and spacing, and the contraction and expansion coefficients.

Sentinel-1 satellite does not have any image until 2015 for Stephenville Crossing. According to the flow gauge records, there was potential flooding in January 2018. Therefore, we analyze the associated Sentinel - 1 images on 14th January, 2018. The comparison between the maximum inundation boundary of 2D HEC-RAS simulation and Sentinel-1 flood map is shown in Figure 5.5. The overall results of sentinel-1 images might not accurate as a reference to compare with the HEC-RAS 2D results. According to the sentinel-1 image, the upstream part of Harry's River is not flooded, however the HEC-RAS 2D shows inundation. The small pixels in the inland area are

possible noise from the sentinel-1 image. The high flow records of the gauge might not represent the occurrence of flooding, and even there is small flooding happened, it is probably not significant enough to be detected by Sentinel 1 at relatively coarse resolution.

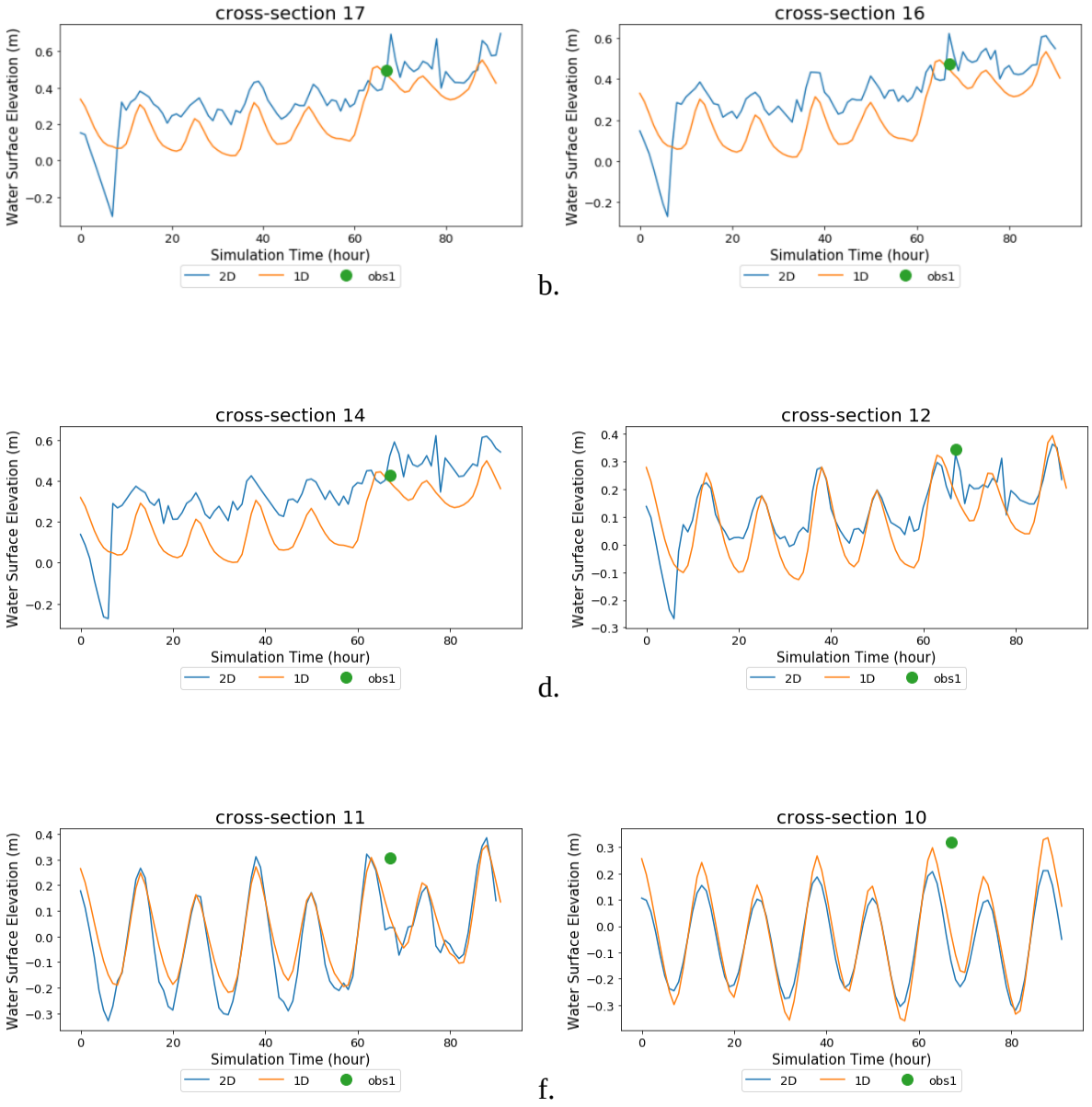

Figure 5. 4 HEC-RAS 1D & 2D model evaluation from 8pm, 3rd November to 4pm, 7th November 2010. Orange represents 1D HEC-RAS results, blue represents 2D HEC-RAS results; obs represents the measurements at 4pm, November 6, 2010.

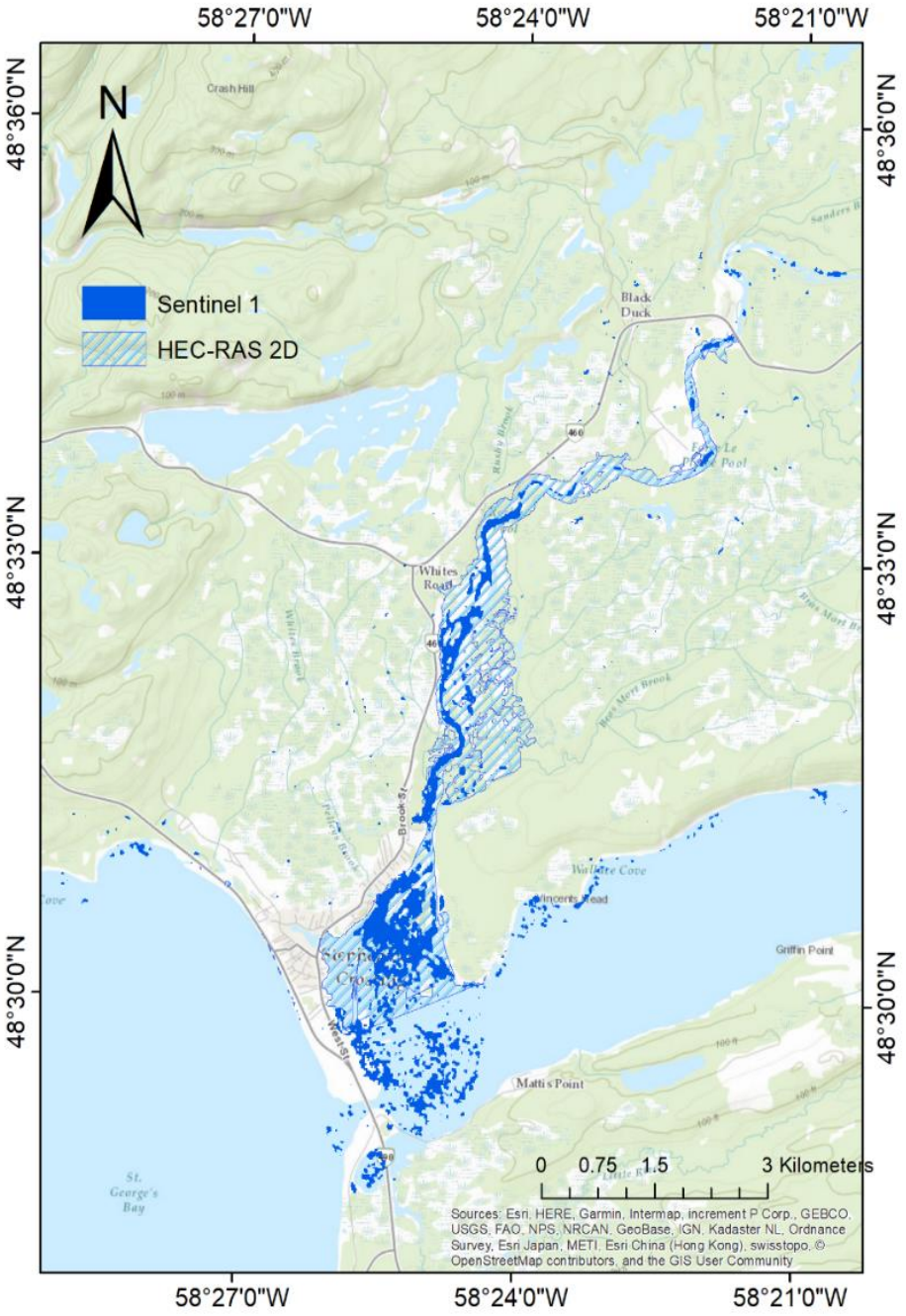

Figure 5. 5 Flood area detection using Sentinel-1 image (compare with results from HEC-RAS 2D)

5.2.2 Sensitivity Analysis

Sensitivity analysis is performed by changing the cell size, DEM product, and the set of Manning's n roughness factors in in the HEC-RAS 2D model (Table 5.1). The 2D HEC-RAS simulation of September 2020 event is not very sensitive to these factors. However, November 2010 event is much more sensitive than September 2010 event, as during November 2010 has a much higher peak flow than September 2010 at around 80 m^3/s and 30 m^3/s, respectively. The sensitivity analysis is conducted with November 2010 event.

Table 5.1 Description of factors considered in the sensitivity analysis

Factors	Description	No. of run
DEM	SRTM (30m resolution), CDEM (20m resolution), TanDEM (90m resolution)	3
Mesh size in 2D simulation area (and around the break-line)	Run1: 100m (70m) Run2: 50m (30m) Run3: 30m(30m) Run4: 20m (15m)	4
Manning's n	Unique value for the floodplain and river channel	3

As mentioned in the model set-up, DEM is crucial in 2D HEC-RAS models, which is also shown in the sensitivity analysis of DEM. A 20m-resolution CDEM significantly increases simulation accuracy when it is compared with 90m-resolution TanDEM. The differences of these DEMs are

significant at the upstream of reach, and the distinction between DEMs gradually decreases as the river flows from upstream to downstream. For the sensitivity analysis of cell size, the comparison of 4 Runs clearly illustrates the importance of spacing, as the decrease of cell spacing improves model performances (Figure 5.6). Run 4 (20m in 2D area and 15m around break-line) has the largest simulated inundation area, however it takes the longest simulation time. Run1 (100m in 2D area and 70m around break-line) with the largest cell size is finished in 20s after the computation of terrain data, but the least simulated inundation area might indicate an underestimation of flood extent. Besides, the balance of computational cost and accuracy also should be considered in model simulation. The sensitivity analysis of the roughness coefficient investigated the manning's n values for river channel and floodplain. It is found that the lower part of reach in HEC-RAS 2D model is not very sensitive to manning's n values (Figure 5.7), therefore a single value of manning's n might be sufficient enough to represent the characteristics of lower floodplain in Stephenville Crossing. Through multiple simulations by varied DEM data, cell size, and manning's n, it is obviously found the middle and upper part of reach in HEC-RAS 2D model is more sensitive in these parameters and inputs. The adjustment of DEM, cell size and roughness coefficients both causes considerable changes in results accuracy.

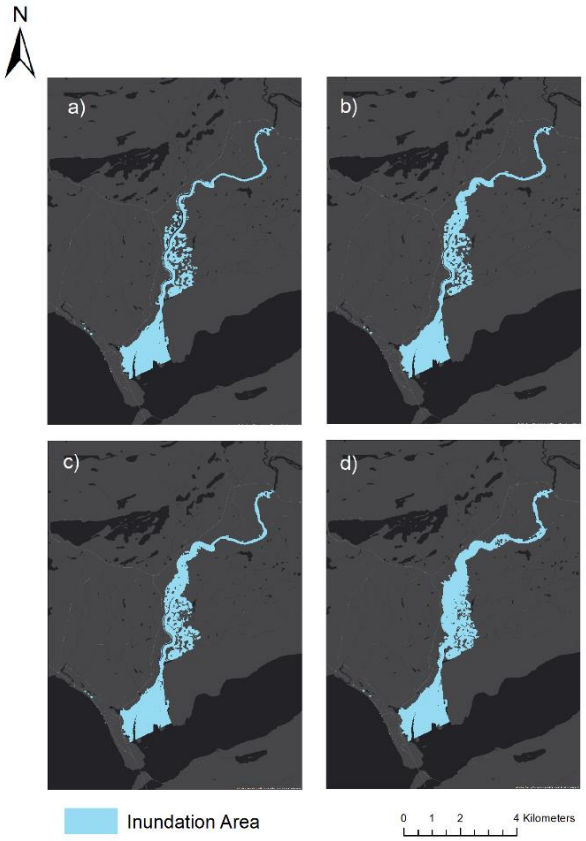

Figure 5. 6 Comparison between 2D simulated flood inundation extents using different mesh sizes (around break line): a. 100m (70m); b. 50m (30m); c. 30m (30m); d. 20m (15m)

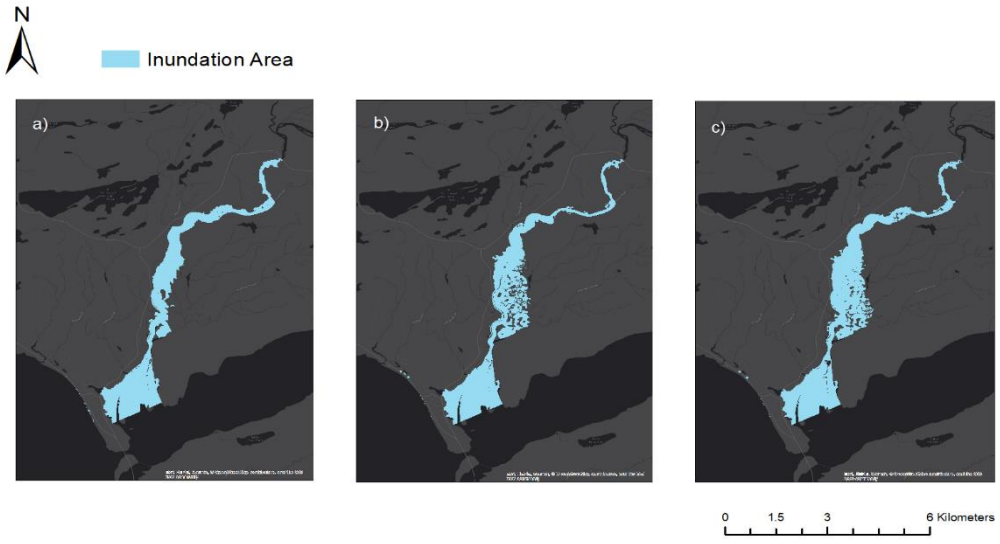

Figure 5. 7 Comparison between 2D simulated flood inundation extents based on different roughness values for channel and floodplain: a) 0.033 and 0.05; b) 0.045 and 0.05; c) 0.033 and 0.08

5.2.3 Climate Change Impacts on Flooding

The simulation of the rainfall-only scenario is conducted by considering historical tide estimates as the downstream boundary condition and projected flow hydrographs generated based on future design storms as upstream boundary condition. Figure 5.8 shows relative changes in the flood inundation extent and maximum flow depths in 2050s (under the RCP 4.5 emission scenario) compared to the reference period (1976-2005). Results correspond to a 25-year event with a design storm generated based on the SCS approach. Increases in rainfall intensity under climate change can lead to higher risks of flooding in low-lying areas. Areas at the upstream are expected to experience large flood extents/depths in a changing climate. Therefore, it is necessary to conduct the climate change impacts analysis in flood risk studies for future planning. Next, we add the effects of projected coastal flood drivers (storm surge, wave, and sea-level rise) and assess compound flooding under climate change. We assume that the peak of the stage hydrograph coincides with the peak of flow hydrographs. Table 5.2 lists the simulated flood inundation areas corresponding to rainfall-only and compound flooding simulations under all future climate scenarios. In all future scenarios, the compound flooding simulation estimates a higher flooding area compared to the rainfall-only analysis. From RCP4.5 to RCP8.5 and from future period of 2050s to 2080s, the flooding areas of two scenarios are increasing. However, the trend is not always consistent with the results of differences in simulated mean inundations from individual flooding and compound flooding. For example, during 25-year flood event simulation, the results of inundation difference show a decrease from RCP 4.5 to RCP 8.5. For a 100-year compound flooding event, RCP 4.5 and far future (2080s) period has the relatively higher risk.

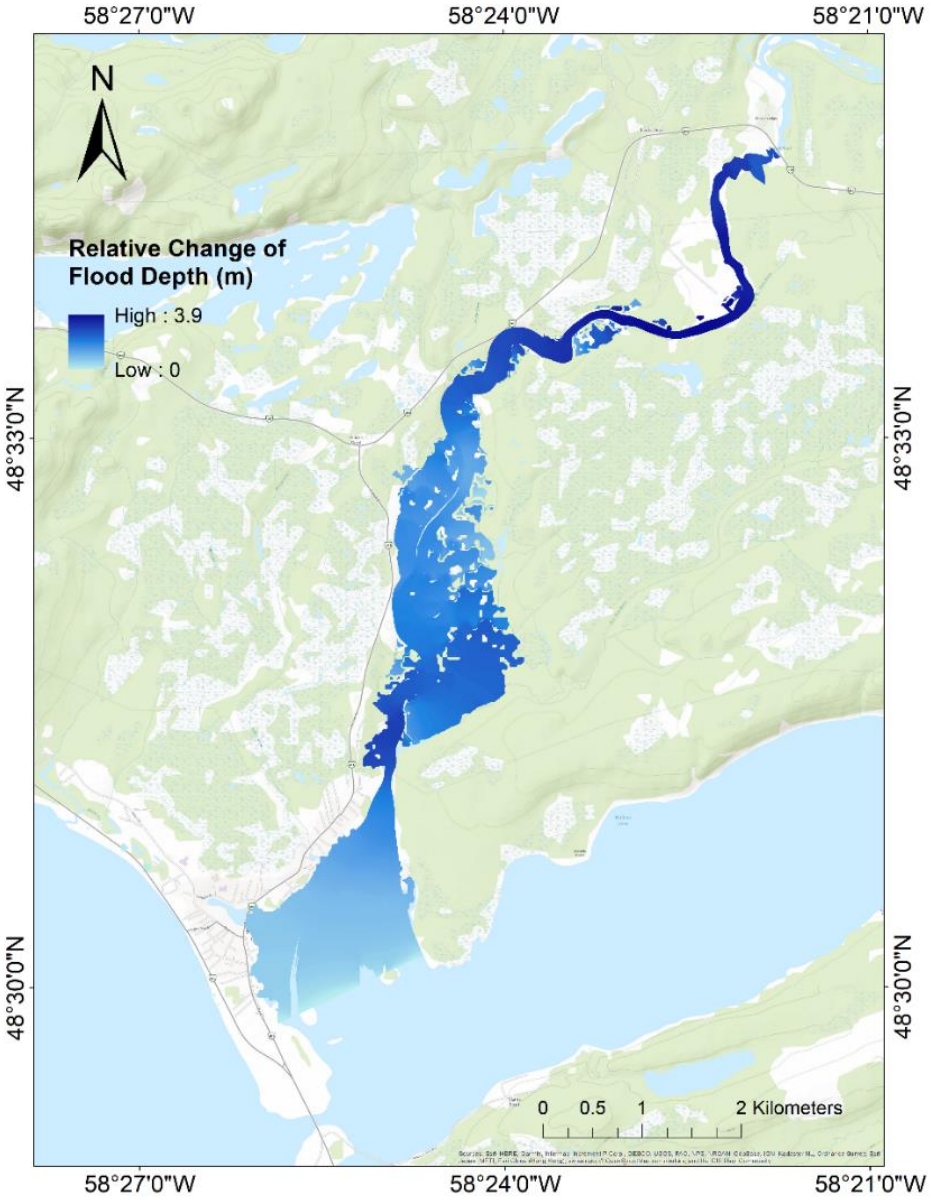

Figure 5. 8 Relative changes in 25-year flood inundation corresponding to RCP 4.5 in 2050s compared to current condition (based on the SCS design storm method)

Table 5.2 Simulated flood inundation (square meter) based on projected WRF-IDF curves (Mean value is calculated over from multiple GCMs)

Return Level	RCP	Future	Fluvial flood scenario	Compound flood scenario
		Period	Mean	Mean
25-year event	4.5	2050s	6164480	6658483
		2080s	6287770	6872976
	8.5	2050s	6281605	6754643
		2080s	6784134	7304280
100-year event	The 4.5	2050s	6972582	7632519
		2080s	7879017	8695312
	The 8.5	2050s	7809291	8493611
		2080s	8980685	9782332

The rainfall-only scenario and compound scenario are compared through flood inundation map of estuarine area (Figure 5.9). The blue area represents the simulation under the changes of future extreme rainfalls. When all coastal components (surge, wave and local sea level rise) are included in simulations, the coastal areas are flooded, as well as the urban zone between the coastline and the estuary area. The mouth of Harry's River is also vulnerable to coastal flooding. This highlights the importance of compound flooding analysis in an estuarine region. The compound impacts from high river inflows, storm surge, and tide cannot be ignored, as well as considering the impacts of climate change such as sea level rise, and land subsidence. The results show the upstream area of Harry's River suffers more from riverine flooding, while the coastal area suffers more from coastal flooding. The estuary or the mouth of the river suffers from both coastal flooding and riverine flooding. The corresponding return period can be estimated by deriving the joint distribution of both flood drivers and characterizing the dependencies (Couasnon et al., 2018).

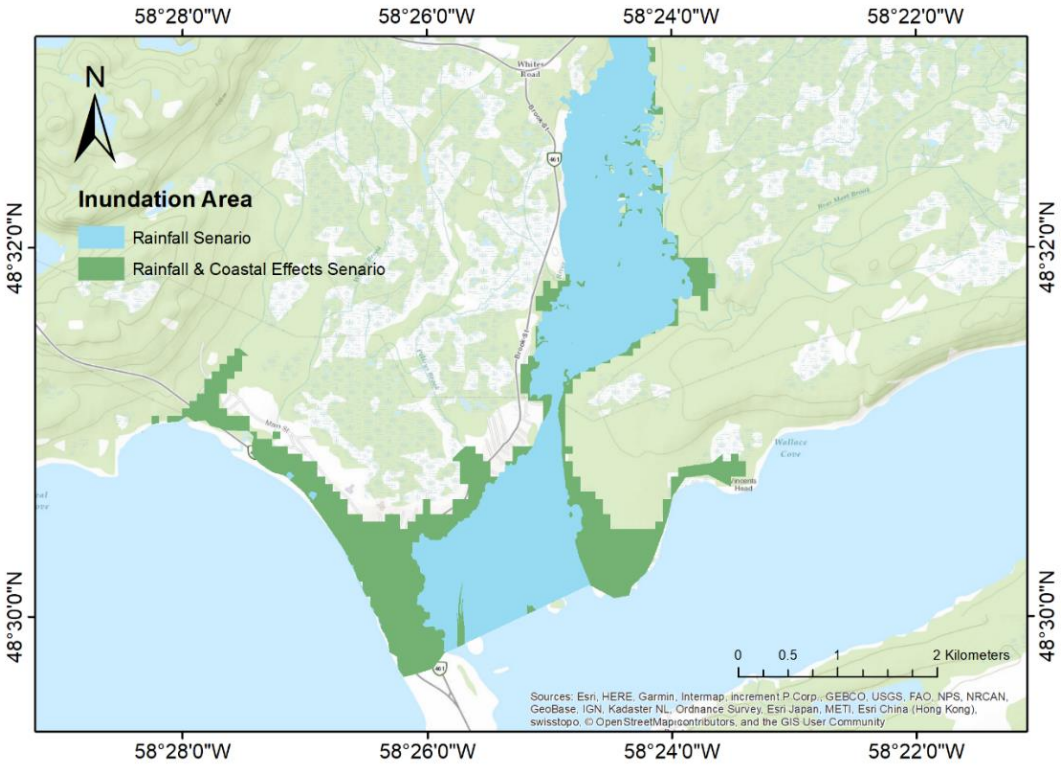

Figure 5. 9 Flood inundation map for rainfall only scenario (blue) and compound scenario (green) that considers the effects from rainfall and coastal components

5.3 Uncertainties in Climate Change Projections

5.3.1 Hyetographs Design

The validated two-dimensional hydrodynamic model is used to assess the impact of climate change on compound flooding and the corresponding uncertainties. A total of 432 hyetographs (288 for WRF- IDF curves and 188 for GCM-IDF curves) were generated for Stephenville Crossing, based

on projected IDF curves, three design storm methods, Representative Concentration Pathways (RCP) 4.5 and 8.5, and two future periods of 2041 - 2070 (2050s) and 2071 - 2100 (2080s) representing the near future and far future scenarios (Table 5.3). There are slight differences in the assessments of climate change impacts based on the two types of projected IDF curves. As mentioned in Section 5.2.2, nine GCMs are selected in climate change analysis using WRF-IDF curves, however, six of those models were available for the GCM-IDF curve assessment (using IDF-Tools). For projected WRF-IDF curve, two future periods, two return periods, two RCP scenarios, nine GCMs and four design storms are considered in this analysis resulting in a total number of 288 simulations. For projected GCM-IDF curve, two future periods, two return periods, two RCP scenarios, six GCMs and three design storms are considered in this analysis with a total number of 188 simulations. Further, there is a slight difference in the implementation of Alternative Block Method for the projected WRF-IDF curves, so two types of ABM hyetographs are generated as ABM1 and ABM2. The first approach is to apply one constant increase rate directly on the IDF equations (ABM1). The second approach applies different increase rates on the IDF equations each hour (ABM2). The hyetographs based on historical IDF and future IDF curves are then used to drive the HEC-HMS model, and three methods of design storms include Soil Conservation Service (SCS), Huff and Alternative Block Method (ABM) (Figure 5.10).

The variations of total rainfall amount between GCM- and WRF-IDFs are shown in Table 5.4. For 25yr event, WRF-IDF generates higher rainfall amounts. The maximum of WRF-IDF curves is similar with GCM-IDF curves, however, the minimum is much higher than GCM-IDF curves, 26% higher for scenario of RCP 8.5 and future period of 2080s. For 100yr event, WRF-IDF generates lower average rainfall amount with a narrower uncertainty range than IDF tools for all future

scenarios. The uncertainty of GCMs has a significant impact on the projected IDF curves using IDF tools due to more variations among selected GCMs.

Table 5.3 List of scenarios and the simulations

Projected IDF curves	**WRF-IDF curve**	**GCM-IDF curve**
Future period	2050s (2041-2070) & 2080s (2071-2100)	
Return period	25-year and 100-year flood events	
RCP	RCPs 4.5 & 8.5	
GCMs	ACCESS1.0, HadGEM2-CC, HadGEM2-ES, GFDL-CM3, MPI-ESM-LR, HadGEM-AO, CSIRO-Mk3.6.0, GFDL-ESM2G, and CanESM2 (total 9)	HadGEM2-ES, GFDL-CM3, HadGEM-AO, CSIRO-Mk3.6.0, GFDL-ESM2G, and CanESM2 (total 6)
Design storms	SCS method Huff method ABM method (2 ways)	SCS method Huff method ABM method
Total No. hyetographs	288	144

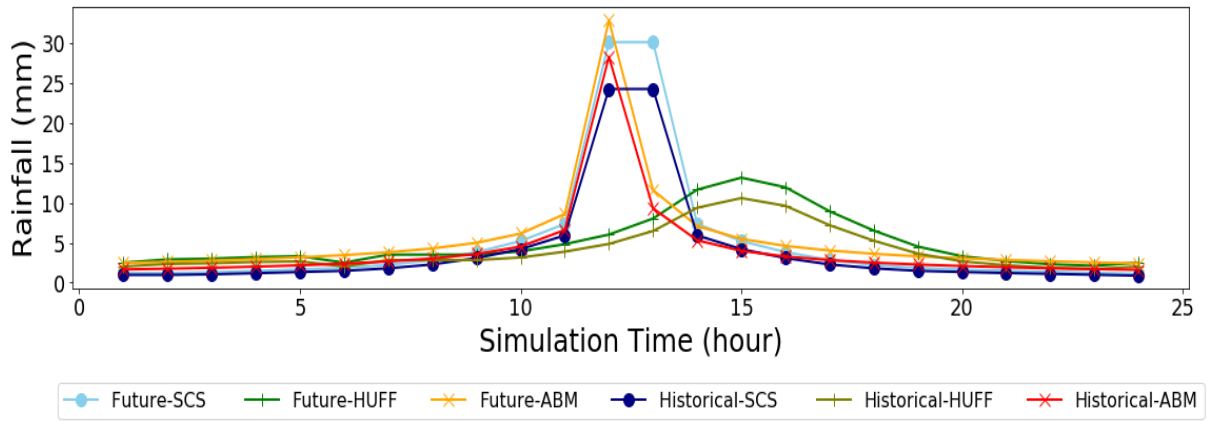

Figure 5. 10 Hyetographs generated by three design methods (Historical: 25-year event; Future: 25-year event, RCP 4.5 and period of 2050s)

Table 5. 4 Comparison of 24-hr rainfall (mm) for current and future climate conditions of 2050s (2041-2070) and 2080s (2071-2100) under emission scenario of RCP 4.5 and RCP 8.5. Six GCMs are considered for hyetographs using WRF-simulation and GCM-simulation curves, respectively

Return period (years)	Current	Future climate change			
		Period	RCP	Multi-model ensemble average of GCMs (*minimum and maximum*)	
				using GCM-simulation	using WRF-simulation
25	107.94	2050s	4.5	131.44 (*111.38, 152.31*)	137.17 (*121.80, 147.35*)
			8.5	135.75 (*118.8, 169.00*)	143.03 (*126.65, 154.14*)
		2080s	4.5	129.93 (*105.00, 153.94*)	141.62 (*127.04, 151.94*)
			8.5	142.50 (*113.86, 176.36*)	163.05 (*145.5, 176.54*)
100	142.79	2050s	4.5	184.82 (*144.33, 233.31*)	169.73 (*150.15, 182.70*
			8.5	185.32 (*149.58, 241.31*)	177.20 (*156.33, 191.35*)
		2080s	4.5	181.76 (*124.37, 237.56*)	175.40 (*156.83, 188.55*)
			8.5	200.0 (*133.85, 333.34*)	202.70 (*180.34, 219.89*)

Resulting hyetographs between three design storm methods for a 25-year event corresponding to the RCP 4.5 emission scenario for 2050s are compared in Figure 5.11. The figure shows the average values of hyetographs generated based on multiple GCMs and the corresponding maximum and minimum values. The peak rainfall occurs at around the 11^{th} hour for both ABM and SCS design dorms, while the peak rainfall of Huff design storms occurs around the 14^{th} hour. Designed hyetographs based on Alternative Block Method (ABM) have the highest peak rainfall and peak intensity, then followed by the hyetographs based on SCS method. In general, the peak precipitation values in Huff hyetographs are much smaller, with less variation in magnitude. The overall rainfall pattern in Huff method is more even and flat than other two methods. Consequently, the estimated flow discharge is much smaller and it may cause an underestimation in peak flood volume in the hydrodynamic model simulation. The overall pattern of rainfall graphs are similar in ABM-1 and ABM-2, however, the ABM2 hyetographs generated by varied scaling rates have

slightly higher peak values among GCMs, as there also is a slightly wider uncertainty range between them. For the near future scenario with 25-yr event, the mean peak flow is similar between two projected IDF curves, and the difference might be enlarged for higher return level events, and higher emission scenarios.

The differences in ABM hyetographs between two projected IDF curves are also shown in Figure 5.12, corresponding to 100-year event under a high emission scenario of RCP8.5 and the far future of 2080s. The lower bound of hyetographs generated by WRF-IDF curves is higher than that generated by GCM-IDF curves, while the comparison between their higher bounds is opposite. Similar results are also be observed in Figure 5.11. The lower bound of design storms from GCM-IDF curves is very close to hyetographs generated through historical IDF curve, which is consistent with the results in Table 5.4. The minimum rainfall amount for some cases in GCM-simulated IDF curves is lower than the total rainfall based on historical condition, such as 100-year event under future period of 2080s. Part of selected GCMs simulates lower precipitation for far future period under RCP 8.5. It is indicated that the uncertainty range of hyetographs based on GCM-IDF curves is relatively large and significant.

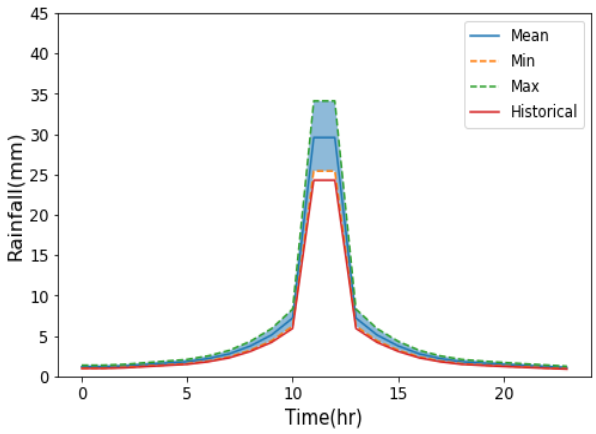

(a1)

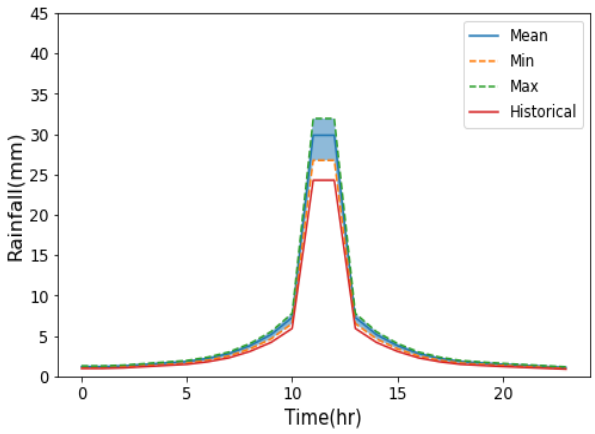

(a2)

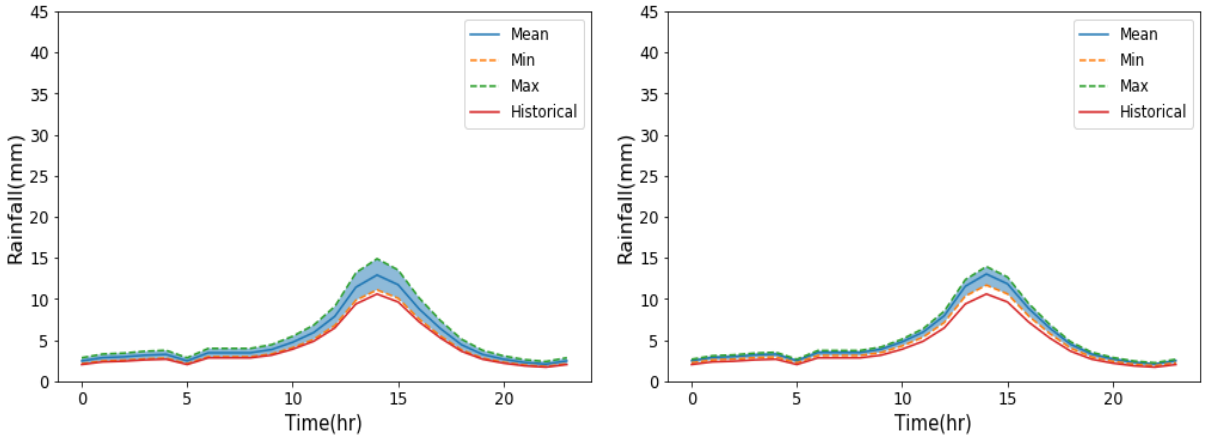

(b1)

(b2)

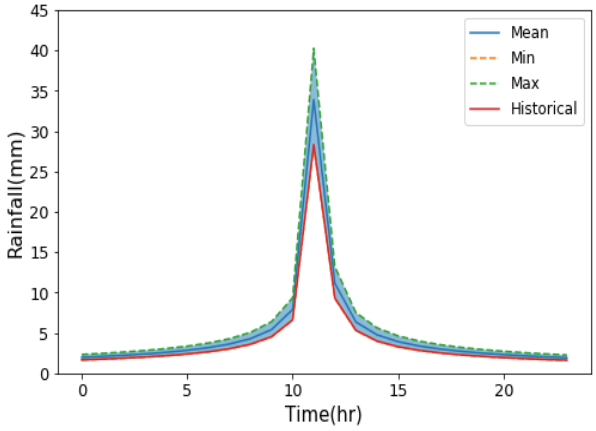

(c1)

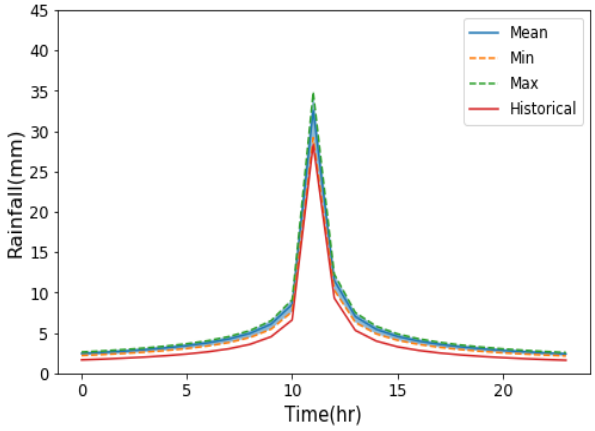

(c2)

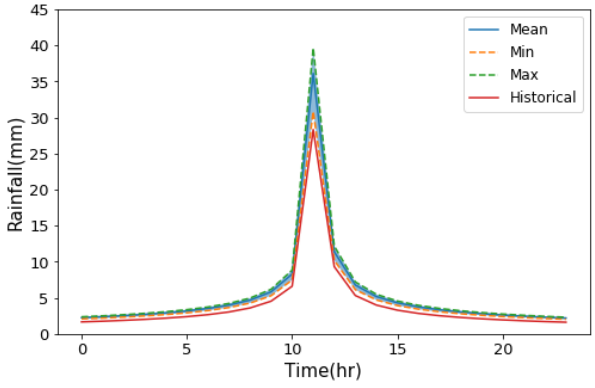

(c3)

Figure 5. 11 Projected rainfall hyetographs corresponding to 25-year event based on historical condition and future condition of RCP 4.5 emission scenario in 2050s. Hyetographs are generated based on projected GCM-IDF curves using a1. HUFF method, b1. SCS method, and c1. ABM design storm method; while others based on WRF-IDF curves using a2. SCS method, b2. HUFF method, c2. ABM-1 and c3. ABM-2.

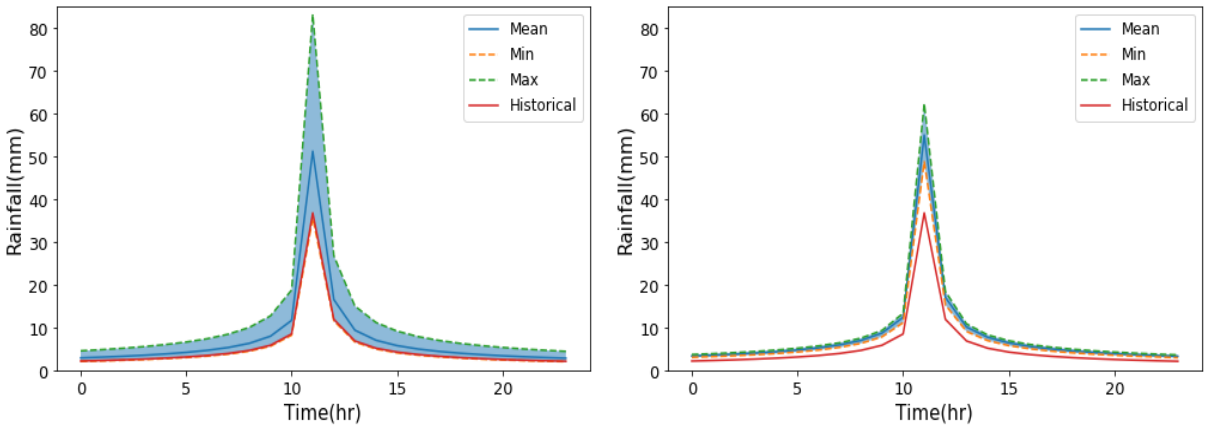

Figure 5. 12 Projected rainfall hyetographs corresponding to 100-year event based on historical condition and future condition of RCP 8.5 emission scenario in 2080s. The hyetographs are generated based on projected a. GCM-IDF (ABM)and b. WRF-IDF (ABM-2)

Resulting design storms for CanESM2 based on RCP 4.5 emission scenario are shown in Figure 5.13. All hyetographs (based on ABM, SCS and Huff methods) are defined with a one-hour time interval and a total storm duration of 24 hrs. Results show a considerable difference in rainfall patterns based on different approaches. In the alternative block method (ABM), high rainfall intensity is maximized within a short duration, which occurs at the middle time of the whole event, for example, the peak rainfall intensity always happens at the 12^{th} hr during the 24-hr event. Differences between ABM hyetographs in 2080s are generally larger than those in 2050s. The peak rainfall value of ABM2 hyetograph is always higher than the amount in ABM1 hyetograph because shorter duration always gives a higher scaling rate, and the difference in the two approaches of WRF-IDF curve in alternative block method varies with RCP scenarios and future periods. The overall pattern of hyetographs generated by the SCS method is very similar to ABM hyetographs, however SCS hyetographs generate a longer time of maximum rainfall. The timing of peak rainfall value in the hyetographs generated by Huff method is about 3 hours later than the

peak time of ABM and SCS hyetographs. In addition, the magnitude of maximum precipitation of Huff hyetographs is considerably smaller than the hyetographs generated by the other two methods. The differences in the peak rainfall can be as high as three times among design storm methods. The ABM hyetographs have maximum precipitation peak, followed by SCS hyetographs and Huff hyetographs. The maximum rainfall amount in a 25-yr event during the future period of 2050s ranges from 13 mm, based on the Huff approach, to 39 mm based on ABM2. Within a 24-hr duration storm, the peak rainfall intensities are the largest in ABM and SCS hyetographs, while Huff hyetographs provide relatively low rainfall intensities that are distributed over an extended period of time. Consequently, the variations of rainfall patterns are highly dependent on the choice of design storm methods.

The relative differences between the project IDF curves (GCM vs. WRF precipitation simulations) based on CanESM2 under two future periods and return levels are also shown in Figure 5.13. Considering the RCP 4.5 scenario, there are slight differences in the 25-year rainfall event between the hyetographs generated by GCM-IDF and WRF-IDF curves. For simulations based on CanESM2, the peak rainfall in design storms based on GCM-IDF curve is higher than that based on WRF-IDF curves, particularly for 100-year event. However, it is not always valid for all GCMs, for example in HadGEM-AO (AO), WRF-IDF curves can generate higher peak rainfall in hyetograph designs than that based on GCM-IDF curves (Figure 5.14). Compared with Huff hyetographs, the differences between two updated IDF curves are more clearly reflected in ABM and SCS hyetographs. Although the differences of peak values between the methods of design storms and projected IDF curves are not very huge, it may cause significant effects in hydrological simulations.

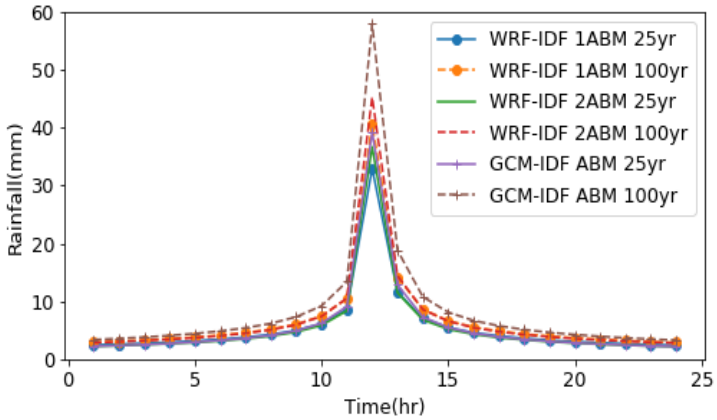

a. ABM method

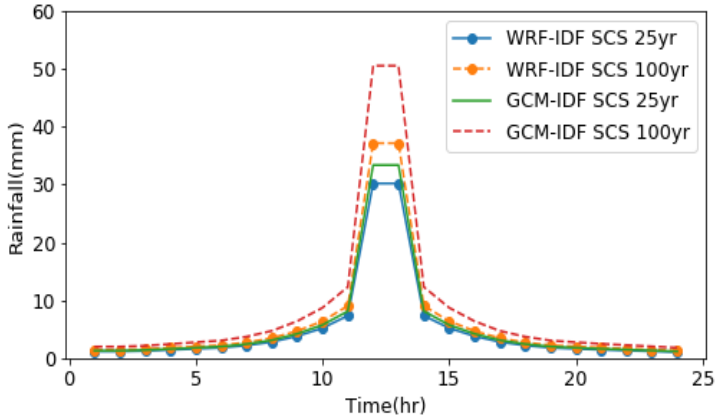

b. SCS method

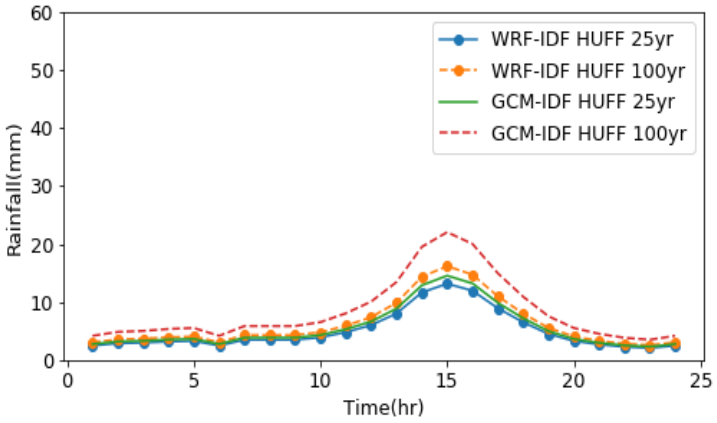

c. Huff method

Figure 5. 13 Rainfall hyetographs for CanESM2, corresponding to future period of RCP4.5 and 2050s (a. ABM method; b. SCS method; c. Huff method)

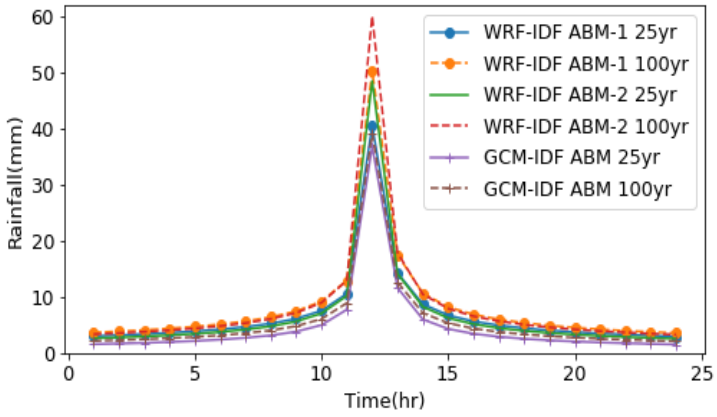

a. ABM method

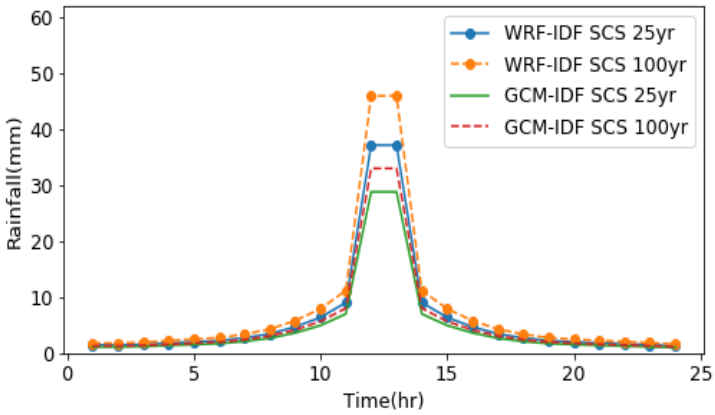

b. SCS method

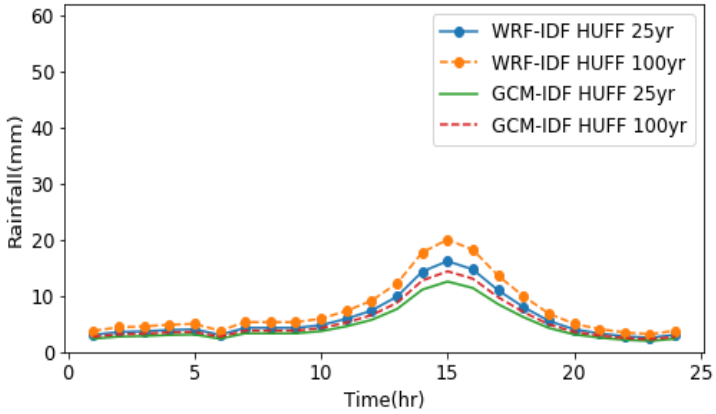

c. HUFF method

Figure 5. 14 Rainfall hyetographs for HadGEM-AO (AO), corresponding to future period of RCP8.5 and 2080s (a. ABM method; b. SCS method; c. Huff method)

Peak rainfall values for all future scenarios by CanESM2 are detailed in Tables 5.5 and 5.6. The hyetographs generated by WRF-IDF curves are projected to have a higher peak precipitation intensity based on RCP 8.5 compared to the RCP 4.5 hyetographs in both future periods. However, the RCP 8.5 peak rainfall generated based on GCM-IDF curves is estimated to be lower than that in RCP 4.5 hyetographs for the 2050s period. RCP 4.5 is an intermediate emission scenario indicating that carbon emissions will decrease after reaching the peak, while RCP 8.5, as the worst-case scenario of climate change models, assumes that the carbon emissions will continue to rise in the future. According to the tables, the magnitude of rainfall in RCP 8.5 scenario is larger compared to the RCP4.5 scenario in most cases. However, design storms by GCM-IDF curves give lower estimation for the future period of 2050s. From RCP 4.5 to RCP 8.5, and from 25-year event to 100 year-event, the trends of hyetographs by WRF-IDF curves remain consistent for all periods and design storm methods. The incoherence GCM-IDF generated hyetographs may be associated with the uncertainty in the projected IDF curves based on GCM precipitation estimations. Comparison between the three design storm methods shows that there is more considerable variation between rainfall peaks associated with higher return-level events in 2080s, compared to those in 2050s. Therefore, the hyetographs for 100-year flood events in 2080s have the largest uncertainties. The duration of peak rainfall can further affect the rainfall-runoff simulations in addition to the differences in peak rainfall values.

Table 5.5 Peak Rainfall (mm) values corresponding to WRF- and GCM-IDF curves based on CanESM2 simulations in 2050s

SCS method	WRF-IDF curves				GCM-IDF curves	
Return period	25yr		100yr		25yr	100yr
RCP 4.5	30.16		37.10		33.32	50.45
RCP 8.5	31.44		38.73		32.48	44.88
DIFF between RCPs	1.28		1.62		***-0.84***	***-5.56***
Huff method	WRF-IDF curves				GCM-IDF curves	
Return period	25yr		100yr		25yr	100yr
RCP 4.5	13.17		16.20		14.55	22.03
RCP 8.5	13.73		16.91		14.18	19.60
DIFF between RCPs	0.56		0.71		***-0.37***	***-2.43***
ABM method	WRF-IDF curves				GCM-IDF curves	
Return period	ABM1		ABM2			
	25yr	100yr	25yr	100yr	25yr	100yr
RCP 4.5	32.90	40.66	36.63	45.21	39.17	57.85
RCP 8.5	34.30	42.44	38.80	47.94	38.17	52.01
DIFF between RCPs	1.40	1.78	2.18	2.73	***-0.99***	***-5.84***

Table 5.6 Peak Rainfall (mm) values corresponding to WRF- and GCM-IDF curves based on CanESM2 simulations in 2080s

SCS method	WRF-IDF curves				GCM-IDF curves	
Return period	25yr		100yr		25yr	100yr
RCP 4.5	31.33		38.59		29.66	45.78
RCP 8.5	36.09		44.62		36.90	49.61
DIFF between RCPs	4.77		6.04		7.25	3.83
Huff method	WRF-IDF curves				GCM-IDF curves	
Return period	25yr		100yr		25yr	100yr
RCP 4.5	13.68		16.85		12.95	19.99
RCP 8.5	15.76		19.49		16.12	21.66
DIFF between RCPs	2.08		2.64		3.17	1.67
ABM method	WRF-IDF curves				GCM-IDF curves	
Return period	ABM1		ABM2			
	25yr	100yr	25yr	100yr	25yr	100yr
RCP 4.5	34.17	38.61	42.29	47.70	35.06	52.43
RCP 8.5	39.38	46.71	48.91	57.85	42.93	57.60
DIFF between RCPs	5.20	8.09	6.62	10.14	7.87	5.16

5.3.2 Hydrological model simulations

The hyetographs generated based on SCS, HUFF and ABM methods, corresponding to projected WRF-IDF and GCM-IDF curves, are applied as the inputs to the HEC-HMS hydrological model to simulate the upstream basin's hydrological response (i.e. flow discharge).

The variations of simulated peak discharge rates among different design storm methods are shown in Figure 5.15 corresponding to two types of updated IDF curves. Based on WRF-IDF curves, the uncertainties of design storm methods are gradually enlarged from 2050s to 2080s, and from RCP 4.5 to RCP 8.5. However, based on GCM-IDF curves, the peak discharge in the future periods is quite similar during RCP 4.5, where there is a relatively larger difference between near future and far future period during RCP 8.5. The hyetographs generated from method of SCS always provide the highest simulation in peak discharge rate for all future scenarios and two projected IDF curves, while the method of Huff provides the lowest simulations for all cases. Future period of 2080s with a high emission scenario of RCP 8.5 would get the highest river discharge, while the lowest value can be found in near future 2050s with an intermediate emission scenario of RCP 4.5.

The variations of peak discharge among different GCMs are shown in Figure 5.16 for 25-yr and 100-yr design events. For WRF IDF curves, CSIRO-Mk3.6.0 (CSIRO), GFDL-ESM2G (ESM2G) and MPI-ESM-LR (MPI) give relatively lower results, whereas the discharge rates are close for other GCMs. However, for IDF tools, except HadGEM2-ES (ES) that shows the highest peak discharge rates, the projections of other GCMs vary among different future periods**.** GFDL-ESM2G (ESM2G) provides a low peak flow rate in both projected IDF curves. The performance

of GFDL-CM3 (CM3) and HadGEM-AO (AO) are distinct between projected IDF curves. It is obvious to see the uncertainty of GCMs has a significant impact on the projected GCM-IDF curves.

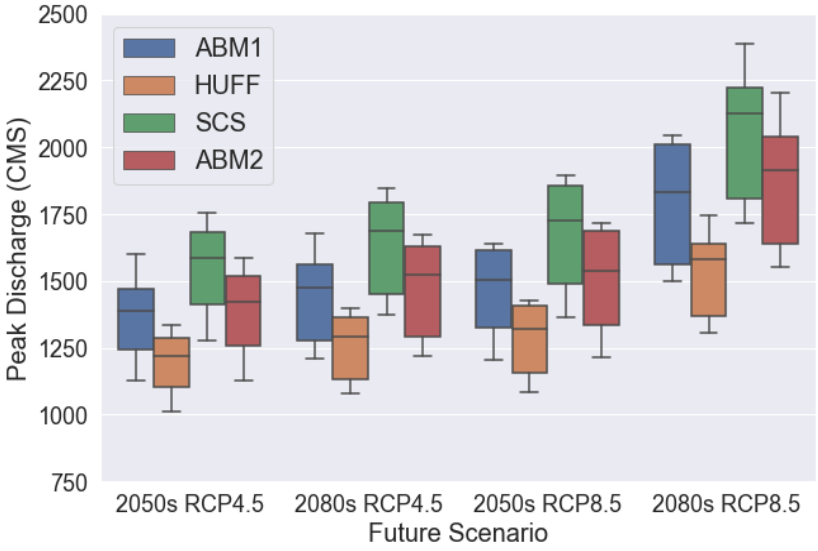

a.

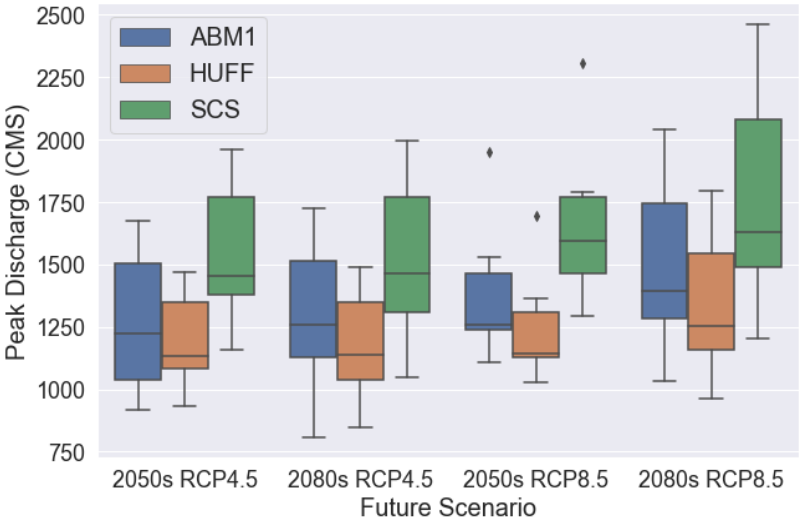

b.

Figure 5. 15 Simulated peak discharge rates (25yr event) based on different design storm methods corresponding to a) WRF-IDF Curves and b) GCM-IDF Curves. ABM1 (alternative block method) represents the way to apply constant temperature scaling rate to the whole event, and ABM2 (alternative block method) shows the way to apply varied temperature scaling rate to each time step. HUFF and SCS represent the method of Huff and the method of Soil Conservation Service. Future scenarios show near future (2041-2070) and far future (2071-2100) periods as 2050s and 2080s, under RCP 4.5 and RCP 8.5 (Representative Concentration Pathway).

The uncertainties between design storms and GCMs are compared for 25-year event during future scenario of 2050s under RCP 8.5 (Figure 5.15 and Figure 5.16). The mean peak flow rates among three design storm methods are ranged from 1300 to 1700CMS (cubic meter per second) for WRF-IDF curves and from 1125 to 1475CMS for GCM-IDF curves, while the mean peak discharges among GCMs are varied from 1150 to 1650CMS for WRF-IDF curves and from 1100 to 1900cm3 for GCM-IDF curves. The uncertainties from the choice of design storm methods are slightly larger than the uncertainties brought by GCMs when using WRF-IDF curves, however, different GCMs bring huge variations than design storm methods in using GCM-IDF curves. Although the choice of the pattern of design hyetographs is important, it is still crucial to pay more attention in the selection of GCMS as it might cause considerable uncertainties when using projected GCM-IDF curves.

The variations between projected IDF scenarios are shown in Figure 5.17. Among different return periods, future periods and RCP scenarios, the results based on GCM-IDF curves show larger ranges of uncertainty. Also, the variations between two projected IDF curves expand with higher RCP index and moving further into the future period. The simulated results conducted through WRF-IDF curves are relatively larger than that through GCM-IDF curves for 100-year event under high emission scenario of RCP 8.8 and far future period (2080s). Except for this scenario, the mean simulations of peak discharge are relatively close for two projected IDF curves. WRF-IDF curves would bring less variations for all scenarios, and the uncertainty between GCMs within WRF-IDF curves is relatively much lower during 100-year event.

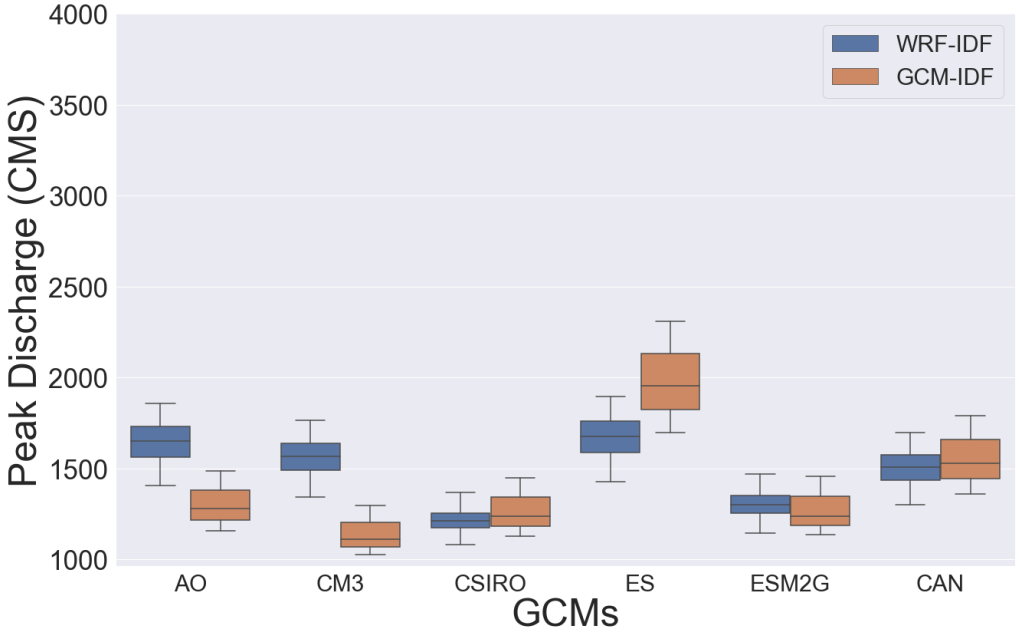

a.

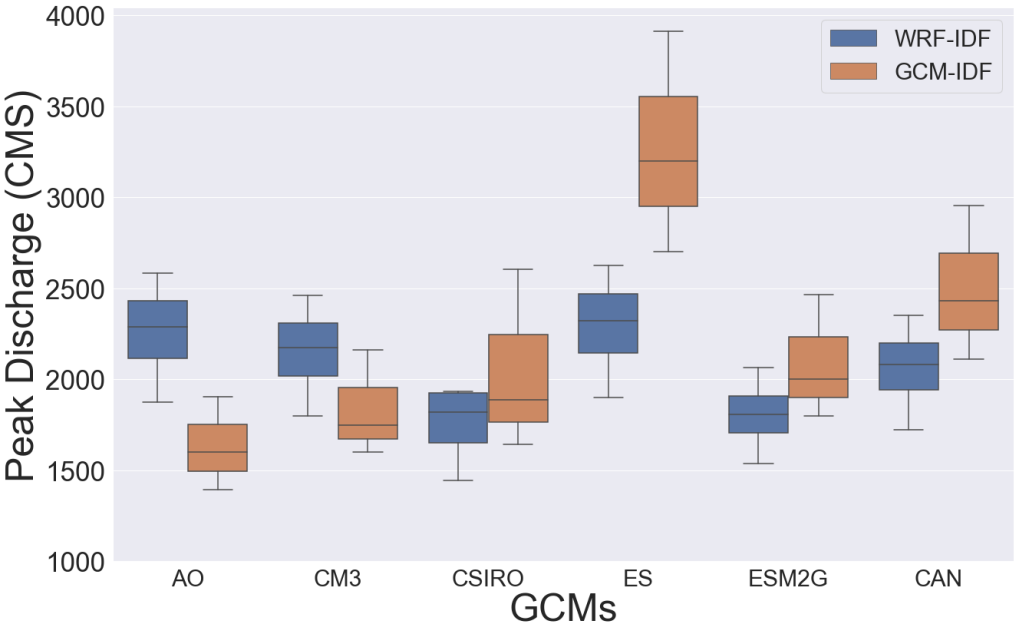

b.

Figure 5. 16 Simulated peak discharge between WRF-simulated IDF and GCM-simulated IDF corresponding to a) 25yrs event and b) 100yrs event). Future scenario is near future 2050s (2041-2070) under RCP 8.5. GCMs used in this study are listed in x-axis from left to right: ACCESS1.0, HadGEM-AO (AO), HadGEM2-CC (CC), GFDL-CM3 (CM3), CSIRO-Mk3.6.0 (CSIRO), HadGEM2-ES (ES), GFDL-ESM2G (ESM2G), MPI-ESM-LR (LR), and CanESM2 (CAN).

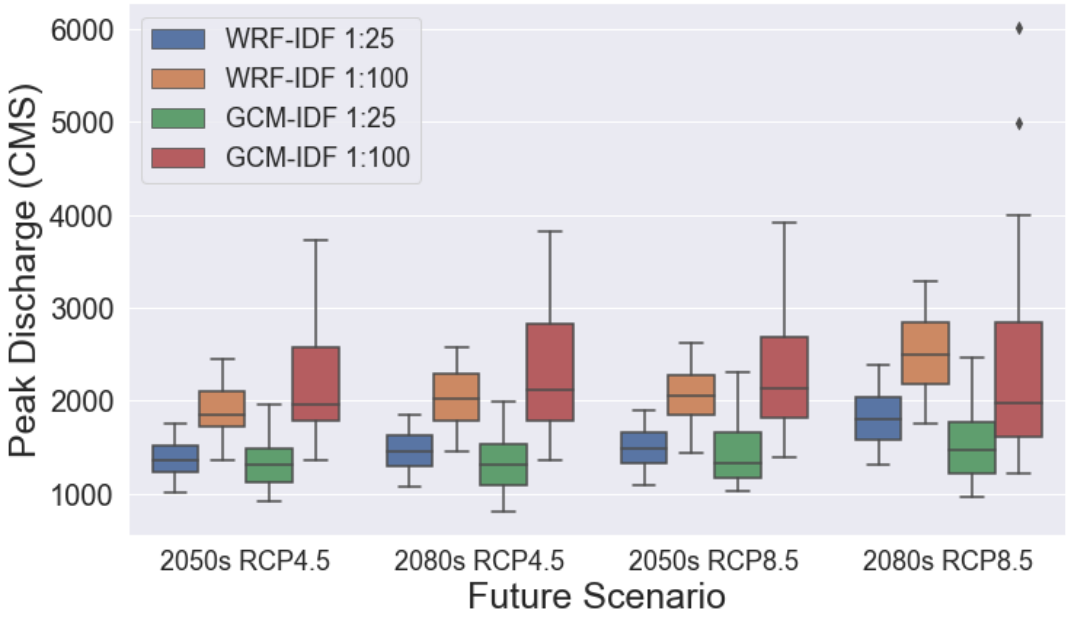

Figure 5. 17 Simulated peak discharge between WRF-simulated IDF and GCM-simulated IDF corresponding to 25yrs and 100yrs event. Future scenario are near future 2050s (2041-2070) and far future 2080s (2071-2100) under RCP 4.5 and RCP 8.5.

The resulting flow graphs between three design storm methods are compared for a 100-year event corresponding to the RCP 8.5 emission scenario for 2050s (Figure 5.18). The figure shows the average values of hydrographs generated based on nine GCMs and the corresponding minimum and maximum values. The overall pattern of simulated hydrographs generated based on the three design storm methods is similar, however the magnitude and timing of peak discharge rates are different. The peak discharge occurs at around the 16th hour for both ABM and SCS design dorms, however, peak discharge of Huff design storms occurs around the 19th hour. The 3-hour time lag is the same as the time lag of peak rainfall between Huff hyetographs and the other two hyetographs. Simulated peak runoff by SCS hyetographs exceeds the peak discharge by ABM hyetographs, which have the highest peak rainfall and peak intensity. In general, the peak discharge rate simulated by Huff hyetographs is much smaller, with less variation in magnitude. The overall

rainfall pattern in Huff method is more even and flat than other two methods. Relatively low rainfall intensities evenly distributed over the event give watershed more time in hydrological response, and thus, the simulated results of Huff hyetographs have less magnitude in peak runoff. Consequently, the estimated flow discharge is much smaller and it may cause an underestimation in peak flood volume in the hydrodynamic model simulation. The overall pattern and magnitude of peak runoff are similar in ABM-1 and ABM-2. However, the ABM2 hyetographs generated by varied scaling rates have more variations in peak flow, as there is a slightly wider higher uncertainty range.

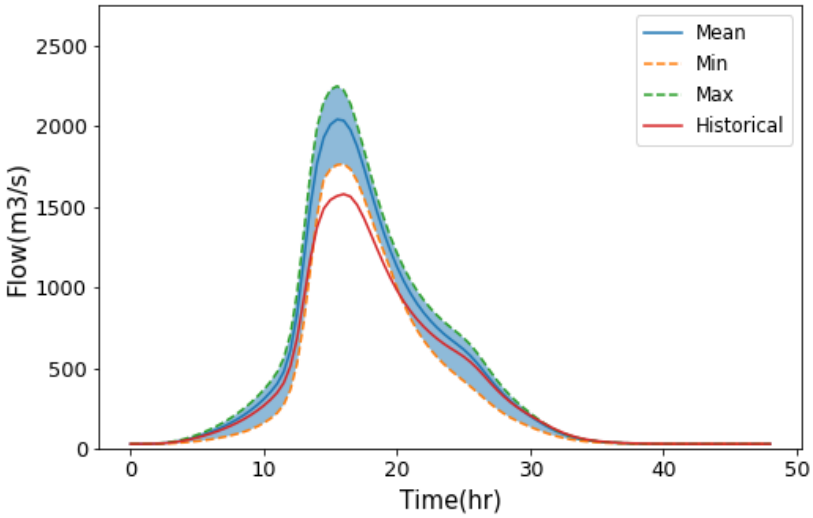

a.

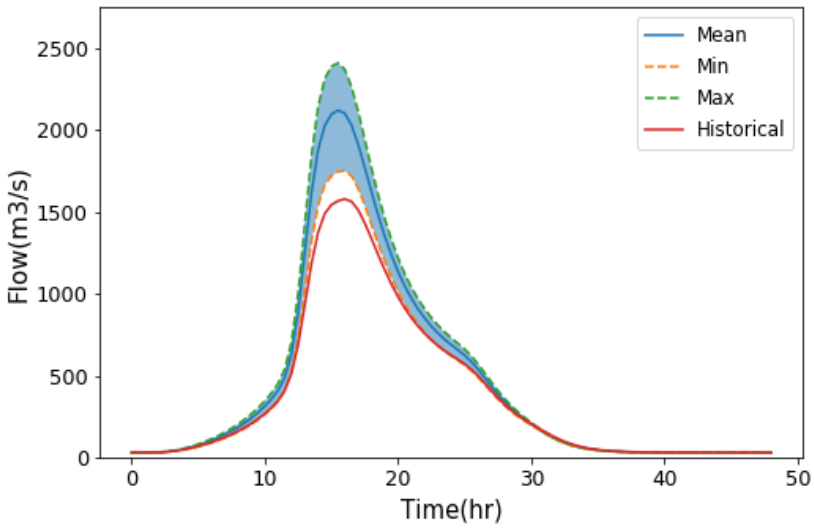

b.

c.

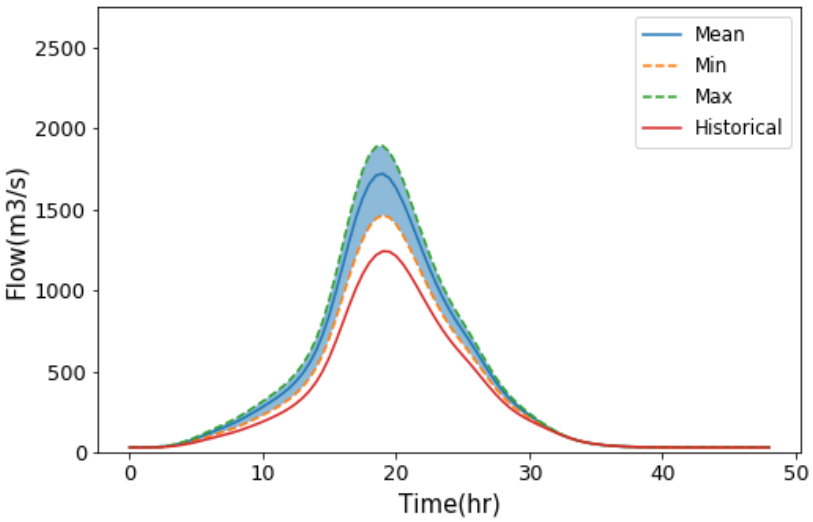

d.

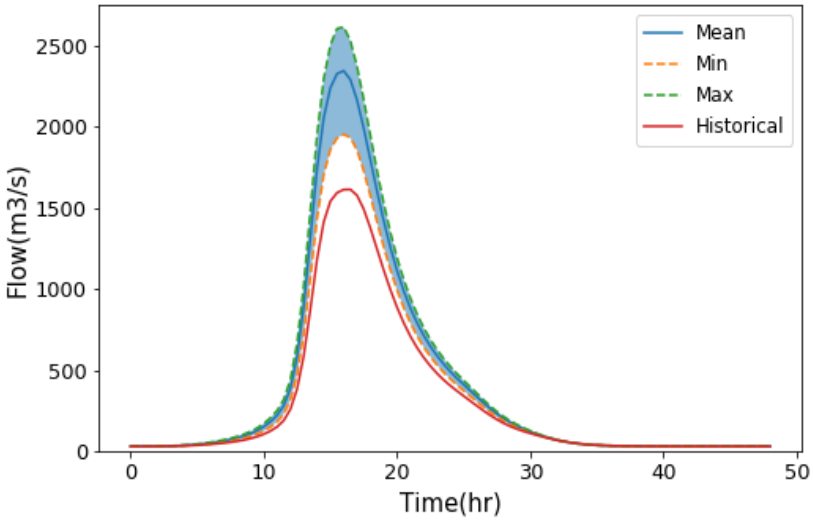

Figure 5. 18 Projected HEC-HMS hydrographs corresponding to the 100-year rainfall event based on historical condition and future condition of RCP 8.5 emission scenario in 2050s. The input hyetographs are generated based on projected WRF-IDF curves using a. ABM1 method, b. ABM2 method, c. Huff method, and d. SCS design storm method

The hydrological responses of the two projected IDF curves (WRF-IDF and GCM-IDF) are shown in Figures 5.19 and 5.20. The discharge hydrographs between the two projected IDF curves for the 25-year flood event are similar in pattern and peak value, but GCM-IDF simulations show larger variations between different GCMs. The peak flow corresponding to GCM-IDF curve ranges from around 900 m^3/s to 1600 m^3/s, while WRF-IDF simulations range between approximately 1100 m^3/s to 1500 m^3/s. A similar situation is observed in 100-year flood event simulation, the resulting average peak flow runoff is almost the same. Compared with 25-year event, the results of 100-year event based on GCM-IDF hyetographs have more significant variations in peak value, which ranges from approximately 1600 m^3/s to 5500 m^3/s. Hence, the hyetographs based on GCM-IDF curve is very sensitive to the choice of GCM, and the uncertainty within GCM structures is magnified in future IDF curves based on GCM rainfall estimates.

The average peak discharge value, based on two future IDF curves is around 1250 m^3/s for 25-year event during RCP 4.5 in 2050s, while the average runoff increases to approximately 2500m^3/s for 100-year event during RCP 8.5 in 2080s. Compared with the same future scenarios, the small differences in hyetographs can cause a huge difference in hydrological simulation, and this illustrates how uncertainty propagates from design storms to hydrological model. The uncertainties corresponding to AMB-1 and ABM-2 IDF methods are relatively low compared to the uncertainties between other design storm methods and projected IDF curves, especially in 100-year flood event simulation.

a.

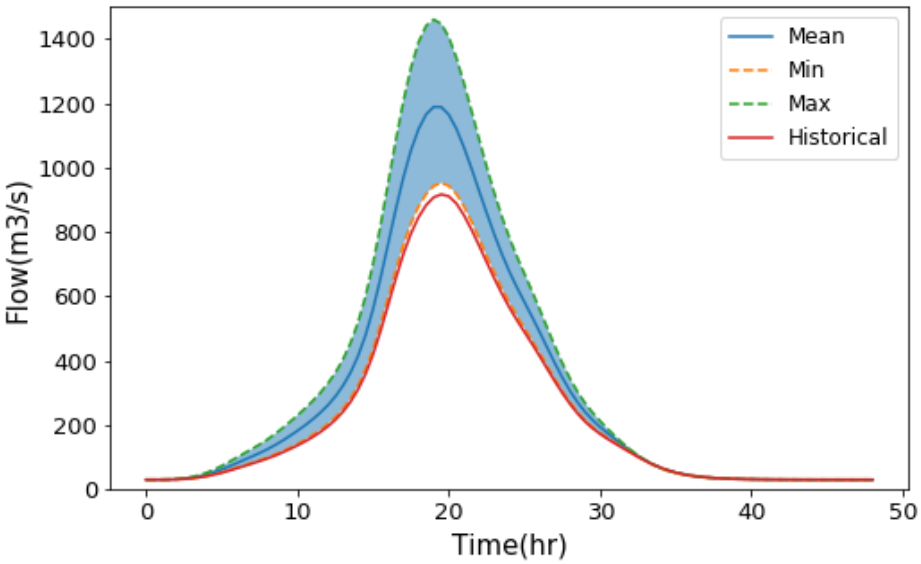

b.

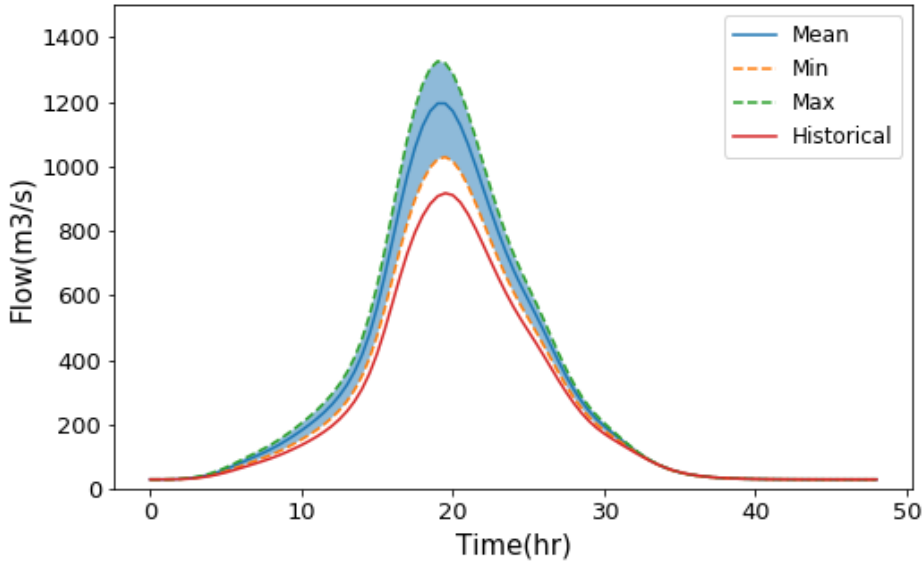

Figure 5. 19 Flow graphs at the gauge of Harry's River below Highway Bridge (see location in Figure 3.5) for a 25-year event corresponding to historical condition and future condition of RCP 4.5 in period of 2050s; a. HUFF hyetograph based on GCM-IDF curves; b. HUFF hyetograph based on WRF-IDF curves

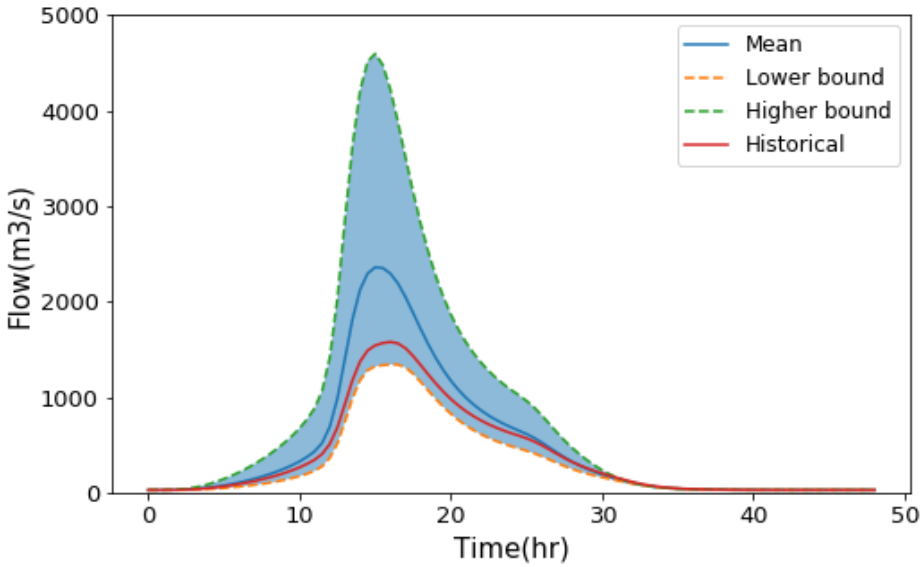

a.

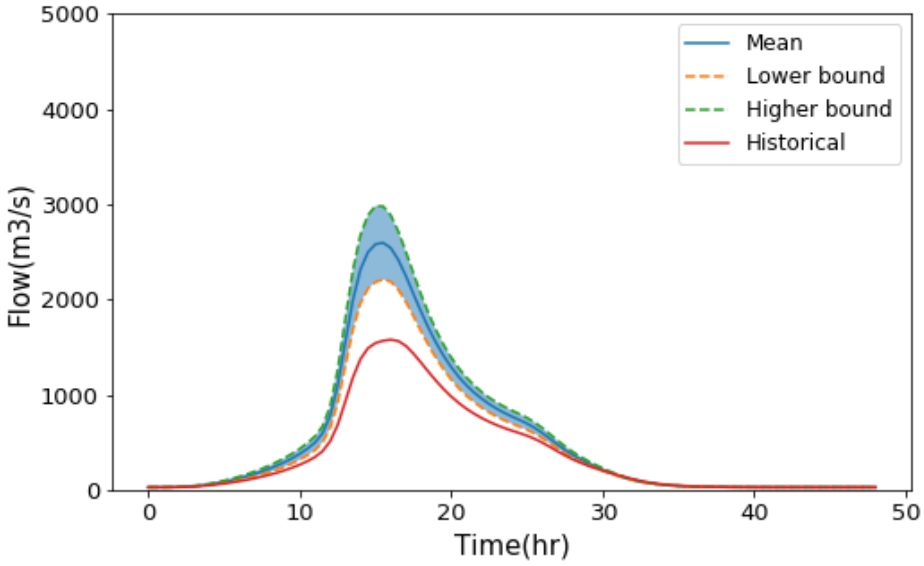

b.

Figure 5. 20 Flow graphs at the gauge of Harry's River below Highway Bridge (see location in Figure 3.5) for a 100-year event corresponding to historical condition and future condition of RCP 8.5 in period of 2080s; a. ABM hyetograph based on GCM-IDF curves; b. ABM2 hyetograph based on WRF-IDF curves

5.3.3 Hydrodynamic model simulations

The resulting flow hydrographs generated by hydrological model are used as the upstream boundary condition of the two-dimensional hydrodynamic model. The areas of the maximum flood extent corresponding to each design storm are summarized in Table 5.7. The Huff method results in the lowest flood inundation area, indicating that it can be considered as the lower bound of flood risk estimates in floodplain management and planning. Although the peak of discharge simulated by SCS hyetographs model is higher than that by ABM hyetographs, the use of ABM design storms will still provide a conservative estimation than others.

Table 5. 7 Inundation Area (square meter) for design storms

Design storm	**25-year event**	**Difference with Huff method**	**100-year event**	**Difference with Huff method**
ABM	6221460	57380	6427390	177980
SCS method	6210230	46150	6431170	181760
Huff method	6164080	0	6249410	0

Relative changes of simulated maximum flood depths between three design storm methods are calculated based on the average of maximum flood depths from all methods (Figure 5.21). During the future period of 2050s under RCP 8.5, method of SCS provides the most conservative simulation for 100-year event, while the method of Huff might underestimate future flooding scenarios greatly. Alternative block method is relatively even among three methods, and ABM2 provides higher estimations than ABM1 method. ABM2 method applies varied caling rate for each time step, while ABM1 method only considers a constant scaling factor for the whole event. The application approach of temperature scaling on ABM method may raise the uncertainty in flooding simulation, but their difference is relatively smaller compared with other design storm methods.

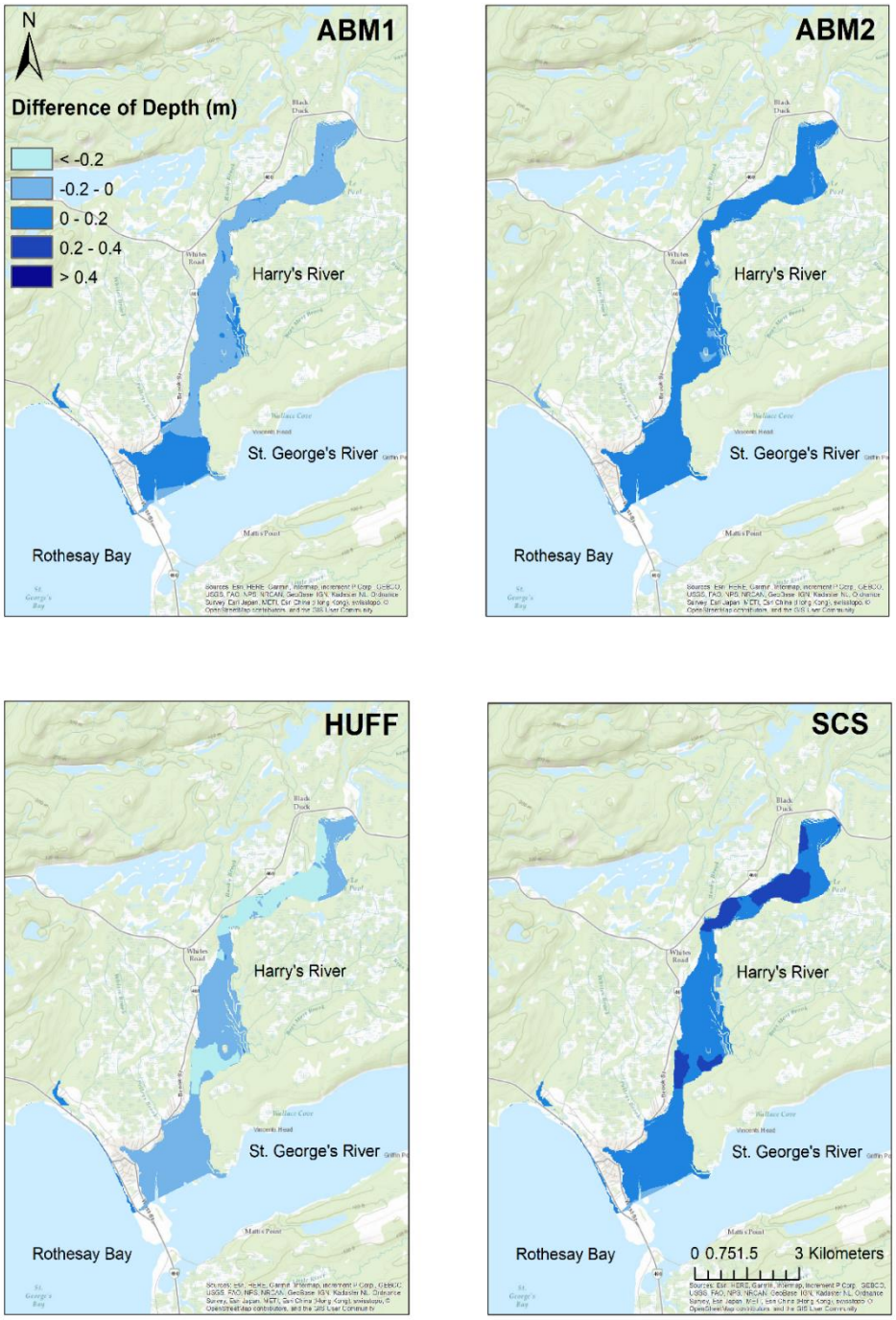

Figure 5. 21 Relative changes in simulated maximum flood depths (m) between different storm design methods (calculated the difference based on the average of maximum flood depths from all methods); Results correspond to a 100-year event, and RCP 8.5 emission scenario in 2050s based on projected WRF-IDF

Relative changes of simulate maximum flood depth of 25-year event and 100-year event are calculated as the difference between current IDF curve and projected future IDF curves, WRF-IDF and GCM-IDF curves (25-year event: Figure 5.22 and Figure 5.23; 100-year event: Figure 5.24 and Figure 5.25).

During 25-year event simulation, the relative changes of simulated flood depths through GCM-IDF curves are relatively small for two future periods of 2050s and 2080s under RCP4.5 (Figure 22.a and Figure 23.a), while the changes for RCP 8.5 are slightly higher at the middle region of Harry's River. Results from WRF-IDF curves are close from all future scenarios of 25-year event, except the case of RCP 8.5 and far future of 2080s, which has more inundation at the upstream and a few relatively high difference at the middle of river. Relative changes for the average simulated maximum depth are not significantly different between Figure 23.b-d and Figure 24.b-c. Overall, RCP 4.5 scenario based on GCM-IDF curves provides the lowest relative changes on flood depth, while RCP 8.5 and 2080s scenario of WRF-IDF curve provides the highest values witincreaseasment of flood inundation area at upstream stream of Harry's Rvier.

For 100-year event simulation, the inundation areas of upstream increase for most of the cases, except for the results by WRF-IDF curve under RCP 4.5 and future period of 2050s (Figure 5.24.b). The coastal part gets inundated for two projected IDF curves under high emission scenarios RCP 8.5 during both future periods of 2050s and 2080s, however, the result by GCM-IDF curves under RCP 8.5 and future period of 2080s has less changes in flood depth with less inundation area. For this special scenario, the results are consistent with the simulations of rainfall-runoff. GCM-IDF curves provide a very high peak discharge for one GCM, but the average peak discharge is much

lower than simulations through WRF-IDF curves. Therefore the relative changes for flood depths are significantly different between two projected IDF curves under high emission scenario of RCP 8.5 and far future period of 2080s (Figure 5.25). The huge variations existing in GCM-simulated precipitation cause the uncertainty of using projected GCM-IDF curves when cosidering far future flooding analysis under a high emission senario.

Overall the comparision between two types of projected IDF curve is conducted from total rainfall amout calculation to hydrodynamic modeling for mutiple future scenarios. The mean rainfall amounts during 100-year event between GCM-simulations and WRF- simulations are quite similar for RCP 8.5 and the period of 2080s (Table 5.4), but GCM-simulations has significant variations in maximum and minimum rainfall values. After rainfall-runodd simulation, the difference of mean peak flow rate between two future IDF curves becomes relatively large (Figure 5.17), and it is also observed for relative change map of flood depth (Figure 5.25. c-d). These results show the uncertainty within GCMs are enlarged through hydrologic and hydrodynamic models, especially for simulations using projected GCM-IDF curves.

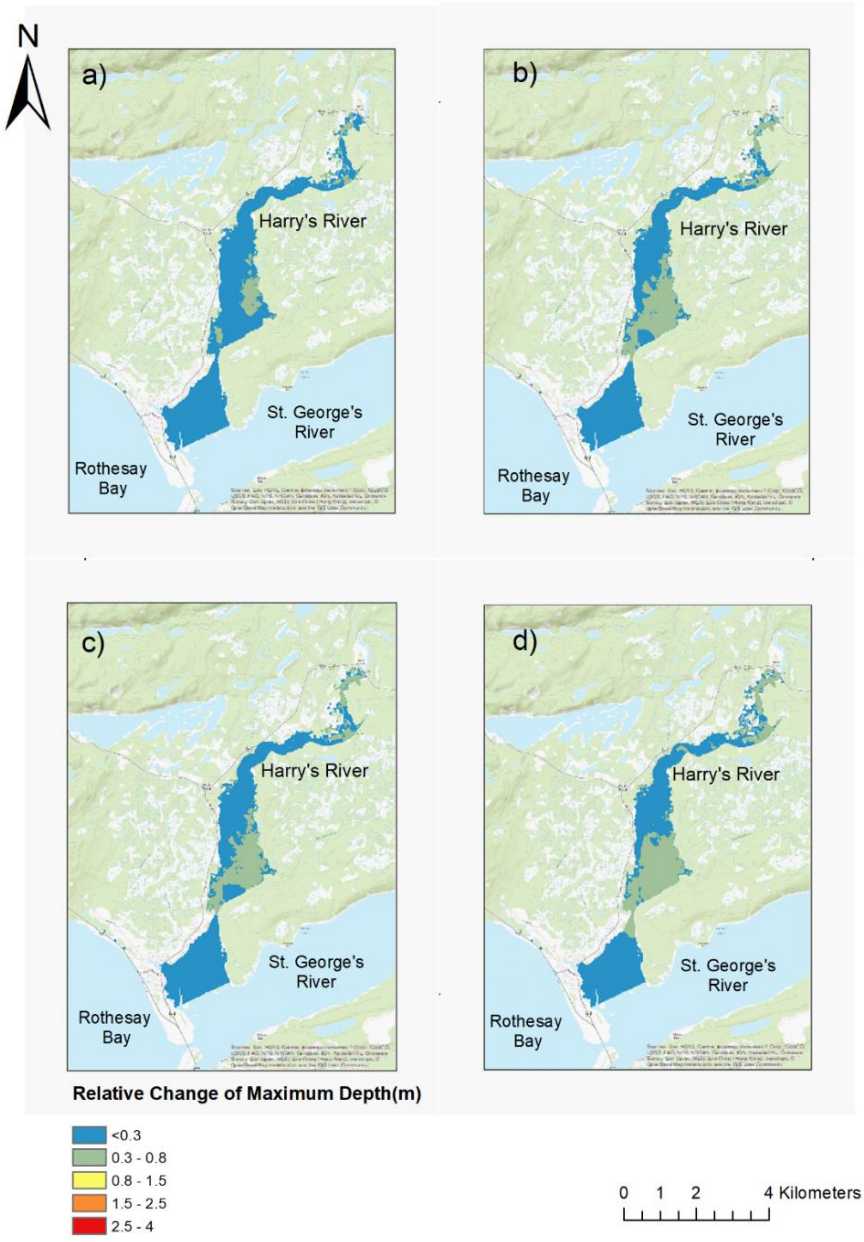

Figure 5. 22 Relative changes in the simulated mean of maximum depth for a 25-year event between future (period of 2050s) and historical condition; a) GCM-IDF under RCP 4.5, b) WRF-IDF under RCP 4.5, c) GCM-IDF under RCP 8.5, d) WRF-IDF under RCP 8.5

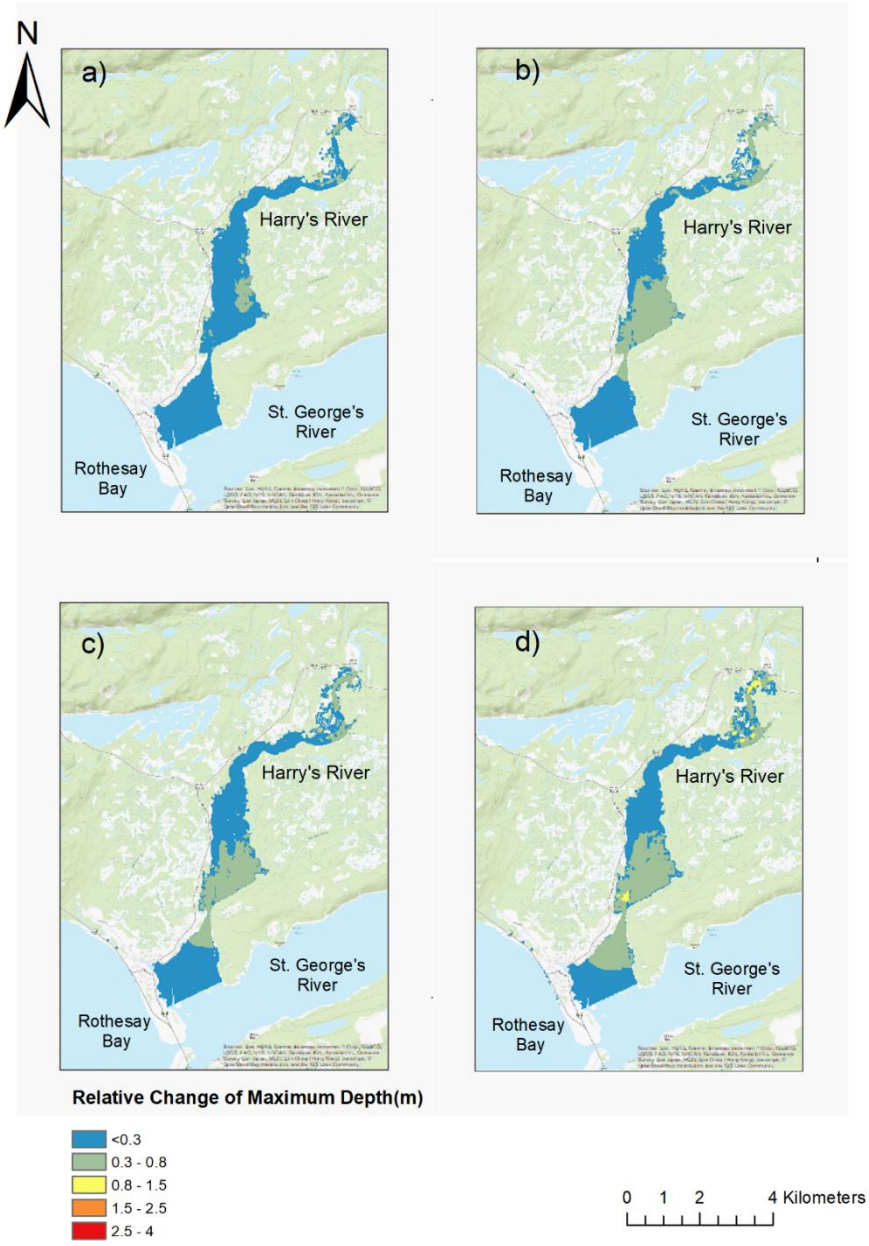

Figure 5. 23 Relative changes in the simulated mean of maximum depth for a 25-year event between future (period of 2080s) and historical condition; a) GCM-IDF under RCP 4.5, b) WRF-IDF under RCP 4.5, c) GCM-IDF under RCP 8.5, d) WRF-IDF under RCP 8.5

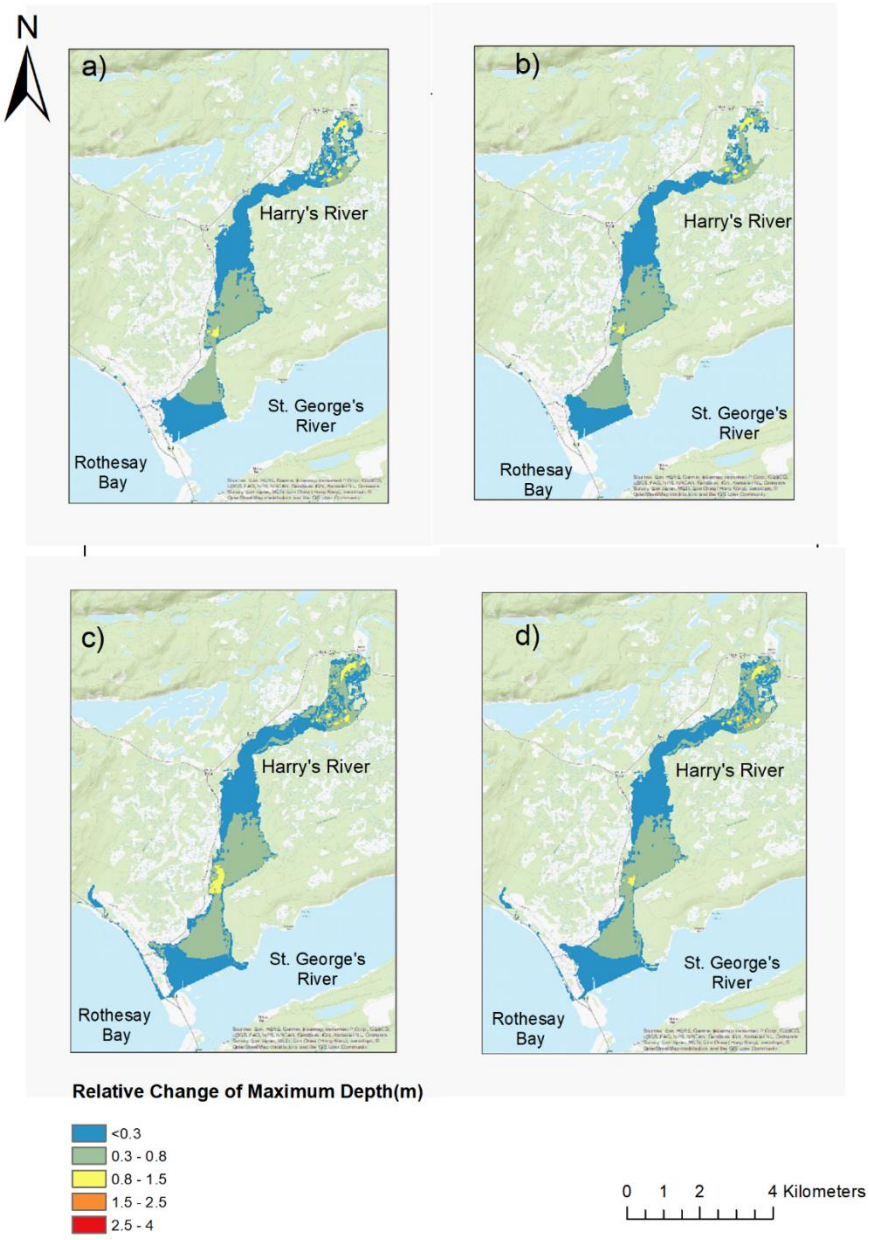

Figure 5. 24 Relative changes in the simulated mean of maximum depth for a 100-year event between future (period of 2050s) and historical condition; a) GCM-IDF under RCP 4.5, b) WRF-IDF under RCP 4.5, c) GCM-IDF under RCP 8.5, d) WRF-IDF under RCP 8.5

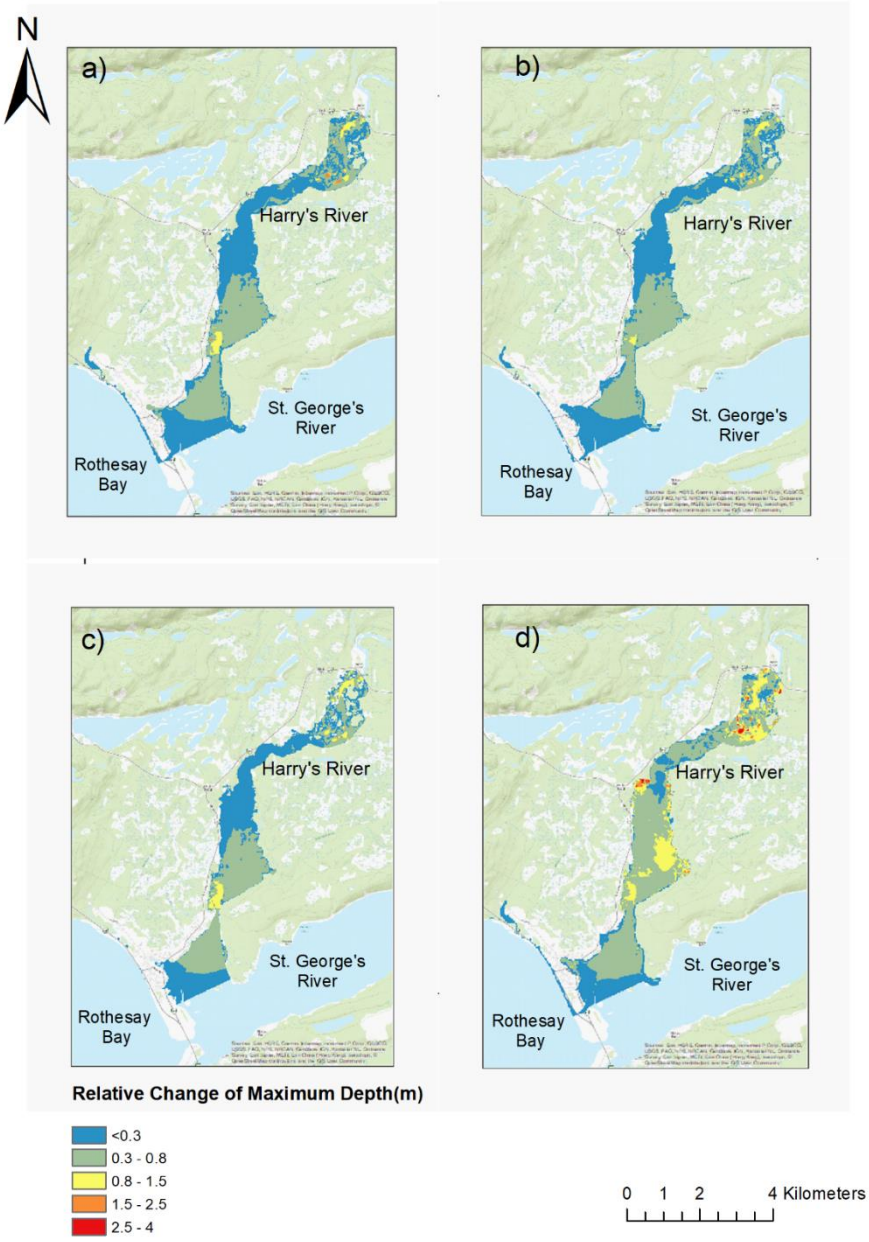

Figure 5. 25 Relative changes in the simulated mean of maximum depth for a 100-year event between future (period of 2080s) and historical condition; a) GCM-IDF under RCP 4.5, b) WRF-IDF under RCP 4.5, c) GCM-IDF under RCP 8.5, d) WRF-IDF under RCP 8.5

5.4 Conclusion

A two-dimensional HEC-RAS model is set up to simulate the individual effects of projected heavy rainfall events, and the combined effects of fluvial and coastal flooding under climate change. The roughness coefficients and downstream boundary condition of HEC-RAS 2D model are calibrated using measurement records along a few cross-sections during 26th September 2010. Then 2D model is validated with observation points and the results of a calibrated 1D model during 3rd November 2010. The results show that the 2D model can capture the peak levels, and match with the most of observations reasonably well, except two observations located at downstream locations.

Sensitivity analysis suggests that the selection of DEM, adequate cell size and Manning's n set is quite important to set up a hydrodynamic model. Only the results at the lower reach are compared with limited results of calibrated 1D mode, therefore, the lower floodplain, which is near the mouth of Harry's River, may be described with a single manning's n value instead of distributed values based on land cover.

The differences in flood extents for current and future climate conditions are significant with more inundation in the estuarine area. The importance of climate change analysis is highlighted in this chapter, as well as the study of compound flooding. Comparison between rainfall-only and compound fluvial-coastal flooding scenarios shows that the riverine flooding mainly affects the inundation area at the upstream of study reach, while coastal flooding causes the inundation on the land between bay and mouth of river. Areas close to the estuary are vulnerable to compound flooding caused by river overflows, storm surge, wave, and sea-level rise. Future urbanization

growth and population increases in urban low-lying areas can further increase the flood risks. Further, there is significant uncertainty in assessing the impacts of climate change on flood characteristics that arise from different design storms, projected IDF curves and climate models, among others.

Identifying different sources of uncertainties and understanding their influences are crucial for floodplain management in a changing climate. The uncertainties associated with GCM structures, future scenarios, design storms, and projected IDF curves are investigated in this Chapter. Future flood simulations correspond to the RCPs 4.5 and 8.5 emissions scenarios in near future (2050s) and far future (2080s) periods. Projected impacts of future climate change on IDF curves are based on WRF- and GCM-simulated precipitation. We apply three design storm methods including SCS, Huff, and Alternative Block Method (ABM). Future assessments are based on nine GCMs including ACCESS1.0, HadGEM2-CC, HadGEM2-ES, GFDL-CM3, MPI-ESM-LR, HadGEM-AO, CSIRO-Mk3.6.0, GFDL-ESM2G, and CanESM2.

Analyses show larger uncertainties corresponding to GCM-IDFs compared to those of WRF-IDFs, including higher variations in estimated hydrographs and flood depths. GCM structure, design storms and RCP scenarios are all significant sources of uncertainty in our analyses. Overall, results suggest that the uncertainties in design storms can be as significant as GCMs in climate change impact analysis. It is necessary to apply different design storms methods, which are varied in rainfall intensities and storm durations for a reliable flood risk assessment. Compared with using a single storm type, applying multiple methods of design storms can significantly advance our understanding of climate change impacts on flood characteristics.

The results show the Huff method may underestimate the peak flood volume, which is consistent with a study of design storms on urban flooding simulation conducted by Pan (2017). The differences between two ways of applying WRF-IDF temperature scales in alternative block method are negligible in our analyses and the corresponding means and uncertainty ranges of hydrographs are almost the same during the two future periods. Notably, there are inconsistent trends between two projected IDF curves from RCP 4.5 to RCP 8.5, and it shows the difference between WRF-IDF curves and GCM-IDF curves.

GCM has limited ability in the simulation of convectional rainfall, and the uncertainty of simulated short-duration rainfall extremes can be translated through projected GCM-IDF curves into flood modeling analysis. Consequently, a considerable variation of maximum flood depths is found in the scenarios based on GCM-IDF curves.

Chapter 6 Conclusion and Future Works

In this study, the individual and compounding effects of riverine and coastal flooding were analyzed over Stephenville Crossing on the west coast of Newfoundland. The area is located between St. George's River estuary and Rothesay Bay. In the past, this community suffered from floods due to storm surge, high river flows caused by heavy rainfall, and their combination. With increases in extreme rainfall events, sea level rise, etc. associated with climate change, such impacts can be exacerbated.

A two-dimensional hydrodynamic model (HEC-RAS 2D) was set-up and coupled with a hydrologic model (HEC-HMS) to simulate the historical and projected changes in flood events and analyze the corresponding uncertainties. The 2D model was driven by the flow hydrographs as the upstream boundary condition and coastal stage hydrographs as the downstream boundary condition. The model was validated using water surface elevation (WSE) measurements at specific points along the river. Further, results were compared with simulations based on a calibrated HEC-RAS 1D model and limited measurement points for 25th September 2010 and 3rd November 2010. The two models showed consistent behavior however slight differences were detected because of differences in the representation of inflow hydrographs. Only the peak discharge value simulated from hydrologic model was used to generate a triangular-shape hydrograph as the upstream boundary condition of 1D hydrodynamic model, while the simulated time-series discharge graphs

were directly applied as the boundary condition in 2D model. The limited number of surveyed cross-section details might cause the misrepresentation of the channel bathymetry as there was about 1/3 simulated reach in 2D model that did not have detailed surveyed cross-sections. Due to the lack of flood images during the event, Sentinel-1 satellite imagery was used for model validation for a period with high flow records. However, many noises existed in the flood map extracted from Sentinel-1, which made it challenging to evaluate the model.

After model validation and sensitivity analysis, the two-dimensional hydrodynamic model was used to assess the effects of individual and compound flooding under future climate scenarios. We assessed the changes in extreme 24-hour rainfall events with return periods of 25 and 100 years under RCP 4.5 and RCP 8.5 representing the intermediate and worst-case emission scenarios. Analyses were performed for the historical period (1976-2005) and future periods of 2041 – 2070 (2050s) and 2071 -2100 (2080s). As expected, the upstream area of Harry's River suffered more from riverine flooding, while the coastal regions were prone to coastal flooding. However, flooding in areas close to the estuary or the mouth of the river can be exacerbated because of the compounding effects of river overflows and increases in coastal water levels (including storm surge, wave, and sea-level rise). Such interactions should be considered in floodplain management and planning.

Further, we studied the uncertainties in the assessment of climate change impacts on flood characteristics that were associated with GCM structure, emission scenarios, design storms, and the approach used to develop projected IDF curves. Consider GCM limitations in simulating

convectional rainfall, projected IDF curves based on high-resolution WRF simulations were applied and compared with GCM-IDF curves. Results showed that WRF simulations project higher rates of heavy rainfall events in the future resulting in more intense flood events in the future compared to those associated with statistically downscaled GCM precipitation simulations. Results also showed relatively lower uncertainty ranges in WRF-IDF simulations.

Future studies are required to extend the analyses and address some of the limitations in this project:

- To assess compound flooding, we considered the worst-case scenario assuming the peak of the flow will coincide with the peak of coastal water level. This results in a conservative assessment of compound flood risks. The timing of the corresponding peaks can be simulated with time lags based on historical flood events or using a coupled in-land coastal hydrodynamic modeling.
- Future analyses are required to analyze the dependencies between different drivers of flooding using robust statistical approaches to characterize the frequency of compound flood events in the study area.
- Due to the limited observation data, the validation of the model was mainly based on water surface elevation measurements of the river. Future surveys and airborne records can provide more reliable observations to evaluate and improve the model.
- Future analyses can consider other satellite observations, besides Sentinel-1, to improve the flood model to validate the simulations. This will support future floodplain mapping and water resources management projects.

- The 1D & 2D HEC-RAS model simulations and comparison can be extended to other hydrodynamic models such as LISFLOOD-FP to assess the uncertainties in different model structures.

Bibliography

Abbasian, M. S., Najafi, M. R., & Abrishamchi, A. 2020a. Increasing risk of meteorological drought in the Lake Urmia basin under climate change: introducing the precipitation–temperature deciles index. *Journal of Hydrology*, 125586.

Abbasian, M. S., Abrishamchi, A., Najafi, M. R., & Moghim, S. 2020b. Multi-site statistical downscaling of precipitation using generalized hierarchical linear models: a case study of the imperilled Lake Urmia basin. *Hydrological Sciences Journal*, *65*(14), 2466-2481.

Abdessamed, D., and B. Abderrazak, 2019, Coupling hec-ras and hec-hms in rainfall–runoff modeling and evaluating floodplain inundation maps in arid environments: case study of ain sefra city, ksour mountain. sw of Algeria: Environmental Earth Sciences, 78, 586.

Abebe, Y., Kabir, G., & Tesfamariam, S. 2018. Assessing urban areas vulnerability to pluvial flooding using GIS applications and Bayesian Belief Network model. *Journal of Cleaner Production*, *174*, 1629-1641.

Alcrudo, F., 2004, A state of the art review on mathematical modelling of flood propagation, impact project.

Alfieri, L., L. Feyen, F. Dottori, and A. Bianchi, 2015, Ensemble flood risk assessment in Europe under high end climate scenarios: Global Environmental Change, 35, 199–212.

Ali, A., 1996, Vulnerability of Bangladesh to climate change and sea level rise through tropical cy- clones and storm surges, in Climate change vulnerability and adaptation in Asia and the Pacific: Springer, 171–179.

Ali, A. M., D. Solomatine, and G. Di Baldassarre, 2015, Assessing the impact of different sources of topographic data on 1-d hydraulic modelling of floods: Hydrology and Earth System Sciences, 19, 631–643.

Anderson, M., Z.-Q. Chen, M. Kavvas, and A. Feldman, 2002, Coupling hec-hms with atmospheric models for prediction of watershed runoff: Journal of Hydrologic Engineering, 7, 312–318.

Arnell, N. W., and S. N. Gosling, 2016, The impacts of climate change on river flood risk at the global scale: Climatic Change, 134, 387–401.

Atlantic Climate Adaption Solutions Association, 2012, Flood risk and vulnerability analysis

project.

Bacopoulos, P., Y. Tang, D. Wang, and S. C. Hagen, 2017, Integrated hydrologic-hydrodynamic modeling of estuarine-riverine flooding: 2008 tropical storm fay: Journal of Hydrologic Engineering, 22, 04017022.

Bakhtyar, R., Maitaria, K., Velissariou, P., Trimble, B., Mashriqui, H., Moghimi, S.,. & Flowers, T. 2020. A new 1D/2D coupled modeling approach for a riverine-estuarine system under storm events: Application to Delaware River Basin. *Journal of Geophysical Research: Oceans*, *125*(9), e2019JC015822.

Bates, P. D., R. J. Dawson, J. W. Hall, M. S. Horritt, R. J. Nicholls, J. Wicks, and M. A. A. M. Hassan, 2005, Simplified two-dimensional numerical modelling of coastal flooding and example applications: Coastal Engineering, 52, 793–810.

Batterson, M., and D. Liverman, 2010, Past and future sea-level change in newfoundland and Labrador: Guidelines for policy and planning: Current Research. Newfoundland and Labrador Department of Natural Resources Geological Survey, Report, 10–1.

Bernier, N. B., & Thompson, K. R. 2007. Tide-surge interaction off the east coast of Canada and northeastern United States. *Journal of Geophysical Research: Oceans*, *112*(C6).

Bevacqua, E., D. Maraun, M. I. Vousdoukas, E. Voukouvalas, M. Vrac, L. Mentaschi, and M. Widmann, 2019, Higher probability of compound flooding from precipitation and storm surge in Europe under anthropogenic climate change: Science advances, 5, eaaw5531.

Bilskie, M., and S. Hagen, 2018, Defining flood zone transitions in low-gradient coastal regions: Geophysical Research Letters, 45, 2761–2770.

Blanton, B., Dresback, K., Colle, B., Kolar, R., Vergara, H., Hong, Y., ... & Wachtendorf, T. 2020. An integrated scenario ensemble-based framework for hurricane evacuation modeling: Part 2—Hazard modeling. *Risk analysis*, *40*(1), 117-133.

Bunya, S., Dietrich, J. C., Westerink, J. J., Ebersole, B. A., Smith, J. M., Atkinson, J. H., ... & Cardone, V. J. 2010. A high-resolution coupled riverine flow, tide, wind, wind wave, and storm surge model for southern Louisiana and Mississippi. Part I: Model development and validation. *Monthly weather review*, *138*(2), 345-377.

Canada, S., 2016, 2016 census of Canada: Technical report, Statistics Canada, Ottawa, Ontario.

Cannon, A. J., and S. Innocenti, 2019, Projected intensification of sub-daily and daily rainfall extremes in convection-permitting climate model simulations over north America: implications for future intensity–duration–frequency curves.: Natural Hazards & Earth System Sciences, 19. Chen, J., F. P. Brissette, A. Poulin, and R. Leconte, 2011, Overall uncertainty study of the hydrologicalhydro- logical impacts of climate change for a Canadian watershed: Water Resources Research, 47.

Carrivick, J. L. 2006. Application of 2D hydrodynamic modelling to high-magnitude outburst floods: an example from Kverkfjöll, Iceland. *Journal of Hydrology*, *321*(1-4), 187-199.

Chen, J., A. A. Hill, and L. D. Urbano, 2009, A gis-based model for urban flood inundation: Journal of Hydrology, 373, 184–192.

Chow, V. T. 1959. *Open channel hydraulics*. Estados Unidos: McGraw-Hill Interamericana.

Chow, V. T. 1988, Applied hydrology: International edition, MacGraw-Hill, Inc, 149.

Cook, A., and V. Merwade, 2009, Effect of topographic data, geometric configuration and modeling approach on flood inundation mapping: Journal of hydrology, 377, 131–142.

Comer, J., Olbert, A. I., Nash, S., & Hartnett, M. 2017. Development of high-resolution multi-scale modelling system for simulation of coastal-fluvial urban flooding. *Natural Hazards and Earth System Sciences*, *17*(2), 205.

Couasnon, A., D. Eilander, S. Muis, T. Veldkamp, I. Haigh, T. Wahl, H. Winsemius, and P. Ward, 2020, Measuring compound flood potential from river discharge and storm surge extremes at the global scale: Natural Hazards and Earth System Sciences Discussions, 20, 489–504.

Couasnon, A., Sebastian, A., & Morales-Nápoles, O. 2018. A Copula-based bayesian network for modeling compound flood hazard from riverine and coastal interactions at the catchment scale: An application to the houston ship channel, Texas. Water, 10(9), 1190.

Cunderlik, J., 2003, Hydrologic model selection for the cfcas project: assessment of water resources risk and vulnerability to changing climatic conditions: Department of Civil and Environmental Engineering, The University of Western Ontario.

Dai, A., R. M. Rasmussen, C. Liu, K. Ikeda, and A. F. Prein, 2020, A new mechanism for warm-season precipitation response to global warming based on convection-permitting simulations: Climate Dynamics, 55, 343–368.

De Roo, A. P. J., Wesseling, C. G., & Van Deursen, W. P. A. 2000. Physically based river basin

modelling within a GIS: the LISFLOOD model. *Hydrological Processes*, *14*(11-12), 1981-1992.

Devia, G. K., B. Ganasri, and G. Dwarakish, 2015, A review on hydrological models: Aquatic Procedia, 4, 1001–1007.

Dibike, Y. B., and P. Coulibaly, 2005, Hydrologic impact of climate change in the Saguenay watershed: comparison of downscaling methods and hydrologic models: Journal of hydrology, 307, 145–163.

Didier, D., Bernatchez, P., Boucher-Brossard, G., Lambert, A., Fraser, C., Barnett, R. L., & Van-Wierts, S. 2015. Coastal flood assessment based on field debris measurements and wave runup empirical model. *Journal of Marine Science and Engineering*, *3*(3), 560-590.

Didier, D., Baudry, J., Bernatchez, P., Dumont, D., Sadegh, M., Bismuth, E., ... & Sévigny, C. 2019. Multihazard simulation for coastal flood mapping: Bathtub versus numerical modelling in an open estuary, Eastern Canada. *Journal of Flood Risk Management*, *12*, e12505.

Eccles, R., Zhang, H., & Hamilton, D. 2019. A review of the effects of climate change on riverine flooding in subtropical and tropical regions. *Journal of Water and Climate Change*, *10*(4), 687-707.

Elkhrachy, I., 2015, Flash flood hazard mapping using satellite images and gis tools: a case study of Najran city, kingdom of Saudi Arabia (ksa): The Egyptian Journal of Remote Sensing and Space Science, 18, 261–278.

Evans, B., Chen, A. S., Djordjević, S., Webber, J., Gómez, A. G., & Stevens, J. 2020. Investigating the Effects of Pluvial Flooding and Climate Change on Traffic Flows in Barcelona and Bristol. *Sustainability*, *12*(6), 2330.

Engineers, U. A. C., 2008, Hydrologic modeling system (hec-hms) application guide: version 3.1.0: Institute for Water Resources, Davis.

Falconer, R., D. Cobby, P. Smyth, G. Astle, J. Dent, and B. Golding, 2009, Pluvial flooding: new approaches in flood warning, mapping and risk management: Journal of Flood Risk Management, 2, 198–208.

Feng, Y., and K. L. Brubaker, 2016, Sensitivity of flood-depth frequency to watershed-runoff change and sea-level rise using a one-dimensional hydraulic model: Journal of Hydrologic Engineering, 21, 05016015.

Fernandez, A., M. R. Najafi, M. Durand, B. G. Mark, M. Moritz, H. C. Jung, J. Neal, A. Shastry, S. Laborde, S. C. Phang, et al., 2016, Testing the skill of numerical hydraulic modeling to

simulate spatiotemporal flooding patterns in the logone floodplain, Cameroon: Journal of Hydrology, 539, 265–280.

Freeze, R. A., and R. Harlan, 1969, Blueprint for a physically-based, digitally-simulated hydrologic response model: Journal of hydrology, 9, 237–258.

Ganguli, P., & Merz, B. 2019. extreme coastal Water Levels exacerbate fluvial flood Hazards in northwestern europe. *Scientific reports*, *9*(1), 1-14.

Gao, C., Z. He, S. Pan, W. Xuan, and Y.P. Xu, 2020, Effects of climate change on peak runoff and flood levels in Qu river basin, east China: Journal of Hydro-Environment Research, 28, 34–47.

Garcia, E. S., & Loáiciga, H. A. 2014. Sea-level rise and flooding in coastal riverine flood plains. *Hydrological Sciences Journal*, *59*(1), 204-220.

Garner, A. J., M. E. Mann, K. A. Emanuel, R. E. Kopp, N. Lin, R. B. Alley, B. P. Horton, R. M. DeConto, J. P. Donnelly, and D. Pollard, 2017, Impact of climate change on New York City's coastal flood hazard: Increasing flood heights from the preindustrial to 2300 ce: Proceedings of the National Academy of Sciences, 114, 11861–11866.

Gaur, A., A. Gaur, and S. P. Simonovic, 2018, Future changes in flood hazards across Canada under a changing climate: Water, 10, 1441.

Gori, A., N. Lin, and J. Smith, 2020, Assessing compound flooding from landfalling tropical cyclones on the North Carolina coast: Water Resources Research, 56, e2019WR026788.

Government of Newfoundland and Labrador, 2012, Hydrotechnical Study of Stephenville Crossing/Black Duck Siding.

Gupta, H. V., Sorooshian, S., & Yapo, P. O. 1998. Toward improved calibration of hydrologic models: Multiple and noncommensurable measures of information. *Water Resources Research*, *34*(4), 751-763.

Halwatura, D., and M. Najim, 2013, Application of the hec-hms model for runoff simulation in a tropical catchment: Environmental modelling & software, 46, 155–162.

Her, Y., S.-H. Yoo, J. Cho, S. Hwang, J. Jeong, and C. Seong, 2019, Uncertainty in hydrological analysis of climate change: multi-parameter vs. multi-gcm ensemble predictions: Scientific reports, 9, 1–22.

Herdman, L., L. Erikson, and P. Barnard, 2018, Storm surge propagation and flooding in small tidal rivers during events of mixed coastal and fluvial influence: Journal of Marine Science

and Engineering, 6, 158.

Hicks, F. E., & Peacock, T. 2005. Suitability of HEC-RAS for flood forecasting. *Canadian water resources journal*, *30*(2), 159-174.

Hinkel, J., D. Lincke, A. T. Vafeidis, M. Perrette, R. J. Nicholls, R. S. Tol, B. Marzeion, X. Fettweis, C. Ionescu, and A. Levermann, 2014, Coastal flood damage and adaptation costs under 21st century sea-level rise: Proceedings of the National Academy of Sciences, 111, 3292–3297.

Hirabayashi, Y., R. Mahendran, S. Koirala, L. Konoshima, D. Yamazaki, S. Watanabe, H. Kim, and S. Kanae, 2013, Global flood risk under climate change: Nature Climate Change, 3, 816–821.

Horritt, M., and P. Bates, 2002, Evaluation of 1d and 2d numerical models for predicting river flood inundation: Journal of hydrology, 268, 87–99.

Hunt, J., 2005, Inland and coastal flooding: developments in prediction and prevention: Philosophical Transactions of the Royal Society A: Mathematical, Physical and Engineering Sciences, 363, 1475–1491.

Hunter, N., P. Bates, S. Neelz, G. Pender, I. Villanueva, N. Wright, D. Liang, R. A. Falconer, B. Lin, S. Waller, et al., 2008, Benchmarking 2d hydraulic models for urban flooding: Proceedings of the Institution of Civil Engineers-Water Management, Thomas Telford Ltd, 13–30.

Ikeuchi, H., Hirabayashi, Y., Yamazaki, D., Muis, S., Ward, P. J., Winsemius, H. C.,& Kanae, S. 2017. Compound simulation of fluvial floods and storm surges in a global coupled river-coast flood model: Model development and its application to 2007 C yclone S idr in B angladesh. *Journal of Advances in Modeling Earth Systems*, *9*(4), 1847-1862.

Jalili Pirani F, Najafi MR. Recent Trends in Individual and Multivariate Compound Flood Drivers in Canada's Coasts. Water Resources Research. 2020 Aug;56(8):e2020WR027785.

Karim, M. F., and N. Mimura, 2008, Impacts of climate change and sea-level rise on cyclonic storm surge floods in Bangladesh: Global environmental change, 18, 490–500.

Kaspersen, P. S., Ravn, N. H., Arnbjerg-Nielsen, K., Madsen, H., & Drews, M. 2017. Comparison of the impacts of urban development and climate change on exposing European cities to pluvial flooding. *Hydrology and Earth System Sciences*, *21*(8), 4131-4147.

Kay, A., H. Davies, V. Bell, and R. Jones, 2009, Comparison of uncertainty sources for climate change impacts: flood frequency in England: Climatic change, 92, 41–63.

Kirkpatrick, J. I. M., and A. I. Olbert, 2020, Modelling the effects of climate change on urban coastal-fluvial flooding: Journal of Water and Climate Change.

Knebl, M., Z.-L. Yang, K. Hutchison, and D. R. Maidment, 2005, Regional scale flood modeling using nexrad rainfall, gis, and hec-hms/ras: a case study for the San Antonio river basin summer 2002 storm event: Journal of Environmental Management, 75, 325–336.

Kumbier, K., R. Cabral Carvalho, A. T. Vafeidis, and C. D. Woodroffe, 2018, Investigating com- pound flooding in an estuary using hydrodynamic modelling: a case study from the Shoalhaven river, Australia.

Kumbier, K., R. C. Carvalho, A. T. Vafeidis, and C. D. Woodroffe, 2019, Comparing static and dynamic flood models in estuarine environments: a case study from south-east Australia: Marine and Freshwater Research, 70, 781–793.

Lee, C., Hwang, S., Do, K., & Son, S. 2019. Increasing flood risk due to river runoff in the estuarine area during a storm landfall. *Estuarine, Coastal and Shelf Science*, *221*, 104-118.

Lian, J., K. Xu, and C. Ma, 2013, Joint impact of rainfall and tidal level on flood risk in a coastal city with a complex river network: a case study of Fuzhou city, China: Hydrology and Earth System Sciences, 17, 679.

Liu, Z., V. Merwade, and K. Jafarzadegan, 2019, Investigating the role of model structure and surface roughness in generating flood inundation extents using one-and two-dimensional hydraulic models: Journal of Flood Risk Management, 12, e12347.

Long, S., T. E. Fatoyinbo, and F. Policelli, 2014, Flood extent mapping for Namibia using change detection and thresholding with sar: Environmental Research Letters, 9, 035002.

Löwe, R., Urich, C., Domingo, N. S., Mark, O., Deletic, A., & Arnbjerg-Nielsen, K. (2017). Assessment of urban pluvial flood risk and efficiency of adaptation options through simulations–A new generation of urban planning tools. *Journal of Hydrology*, *550*, 355-367.

Mah, D. Y., Putuhena, F. J., & Salim, S. 2007. Use of infoworks river simulation (RS) in Sungai Sarawak Kanan modeling. *Journal of the Institution of Engineers, Malaysia (IEM)*, *68*(1), 1-10.

Maksimović, Č., D. Prodanović, S. Boonya-Aroonnet, J. P. Leitão, S. Djordjević, and R. Allitt,

2009, Overland flow and pathway analysis for modelling of urban pluvial flooding: Journal of Hydraulic Research, 47, 512–523.

Mark, O., S. Weesakul, C. Apirumanekul, S. B. Aroonnet, and S. Djordjević, 2004, Potential and limitations of 1d modelling of urban flooding: Journal of Hydrology, 299, 284–299.

Masood, M., & Takeuchi, K. 2012. Assessment of flood hazard, vulnerability and risk of mid-eastern Dhaka using DEM and 1D hydrodynamic model. *Natural hazards*, *61*(2), 757-770.

McClearn, M., 2019, Poor flood-risk maps, or none at all, are keeping Canadian communities in flood-prone areas.

Moftakhari, H. R., Salvadori, G., AghaKouchak, A., Sanders, B. F., & Matthew, R. A. 2017. Compounding effects of sea level rise and fluvial flooding. *Proceedings of the National Academy of Sciences*, *114*(37), 9785-9790.

Najafi, M., H. Moradkhani, and I. Jung, 2011, Assessing the uncertainties of hydrologic model selection in climate change impact studies: Hydrological processes, 25, 2814–2826.

Najafi, M. R., Zwiers, F. W., & Gillett, N. P. 2017. Attribution of observed streamflow changes in key British Columbia drainage basins. *Geophysical Research Letters*, *44*(21), 11-012.

Najafi MR, Zhang Y, Martyn N. A Flood Risk Assessment Framework for Interdependent Infrastructure Systems in Coastal Environments. Sustainable Cities and Society. 2021.

Neal, J., Schumann, G., Fewtrell, T., Budimir, M., Bates, P., & Mason, D. 2011. Evaluating a new LISFLOOD-FP formulation with data from the summer 2007 floods in Tewkesbury, UK. *Journal of Flood Risk Management*, *4*(2), 88-95.

Neumann, B., A. T. Vafeidis, J. Zimmermann, and R. J. Nicholls, 2015, Future coastal population growth and exposure to sea-level rise and coastal flooding-a global assessment: PloS one, 10, e0118571.

News, C., 2014, flooding on west coast due to high winds: CBC News.

Nied, M., T. Pardowitz, K. Nissen, U. Ulbrich, Y. Hundecha, and B. Merz, 2014, On the relationship between hydro-meteorological patterns and flood types: Journal of Hydrology, 519, 3249–3262.

Officer, P. B., 2016, Estimate of the average annual cost for disaster financial assistance arrangements due to weather events: Ottawa, ON: Office of the Parliamentary Budget Officer.

Olbert, A. I., Comer, J., Nash, S., & Hartnett, M. 2017. High-resolution multi-scale modelling of coastal flooding due to tides, storm surges and rivers inflows. A Cork City example. *Coastal Engineering*, *121*, 278-296.

Papaioannou, G., A. Loukas, L. Vasiliades, and G. Aronica, 2016, Flood inundation mapping sensitivity to riverine spatial resolution and modelling approach: Natural Hazards, 83, 117–132.

Pappenberger, F., K. Beven, M. Horritt, and S. Blazkova, 2005, Uncertainty in the calibration of effective roughness parameters in hec-ras using inundation and downstream level observations: Journal of Hydrology, 302, 46–69.

Pasquier, U., Y. He, S. Hooton, M. Goulden, and K. M. Hiscock, 2019, An integrated 1d–2d hydraulic modelling approach to assess the sensitivity of a coastal region to compound flooding hazard under climate change: Natural Hazards, 98, 915–937.

Patel, D. P., J. A. Ramirez, P. K. Srivastava, M. Bray, and D. Han, 2017, Assessment of flood inundation mapping of Surat city by coupled 1d/2d hydrodynamic modeling: a case application of the new hec-ras 5: Natural Hazards, 89, 93–130.

Patro, S., C. Chatterjee, S. Mohanty, R. Singh, and N. Raghuwanshi, 2009, Flood inundation modeling using mike flood and remote sensing data: Journal of the Indian Society of Remote Sensing, 37, 107–118.

Pender, D., S. Patidar, K. Hassan, and H. Haynes, 2016, Method for incorporating morphological sensitivity into flood inundation modeling: Journal of Hydraulic Engineering, 142, 04016008.

Perez, J., M. Menendez, F. J. Mendez, and I. J. Losada, 2014, Evaluating the performance of cmip3 and cmip5 global climate models over the north-east Atlantic region: Climate dynamics, 43, 2663–2680.

Pregnolato, M., Ford, A., Glenis, V., Wilkinson, S., & Dawson, R. 2017. Impact of climate change on disruption to urban transport networks from pluvial flooding. *Journal of Infrastructure Systems*, *23*(4), 04017015.

Public Safety Canada. 2015. Floods. Retrieved August 17, 2020, from https://www.publicsafety.gc.ca/cnt/mrgnc-mngmnt/ntrl-hzrds/fld-en.aspx

Purvis, M. J., Bates, P. D., & Hayes, C. M. 2008. A probabilistic methodology to estimate future

coastal flood risk due to sea level rise. *Coastal engineering*, *55*(12), 1062-1073.

Ramly, S., Tahir, W., Abdullah, J., Jani, J., Ramli, S., & Asmat, A. 2020. Flood Estimation for SMART Control Operation Using Integrated Radar Rainfall Input with the HEC-HMS Model. *Water Resources Management*, *34*(10), 3113-3127.

Ray, T., E. Stepinski, A. Sebastian, and P. B. Bedient, 2011, Dynamic modeling of storm surge and inland flooding in a Texas coastal floodplain: Journal of Hydraulic Engineering, 137, 1103–1110.

Razi, M., J. Ariffin, W. Tahir, N. Arish, et al., 2010, Flood estimation studies using hydrologic modeling system (hec-hms) for Johor river, Malaysia.: Journal of Applied Sciences, 10, 930–939.

Saleh, F., V. Ramaswamy, Y. Wang, N. Georgas, A. Blumberg, and J. Pullen, 2017, A multiscale ensemble-based framework for forecasting compound coastal-riverine flooding: The Hackensack Passaic watershed and Newark bay: Advances in Water Resources, 110, 371–386.

Santiago-Collazo, F. L., M. V. Bilskie, and S. C. Hagen, 2019, A comprehensive review of compound inundation models in low-gradient coastal watersheds: Environmental Modelling & Software.

Semadeni-Davies, A., C. Hernebring, G. Svensson, and L.-G. Gustafsson, 2008, The impacts of climate change and urbanization on drainage in Helsingborg, Sweden: Combined sewer system: Journal of Hydrology, 350, 100–113.

Seneviratne, S., N. Nicholls, D. Easterling, C. Goodess, S. Kanae, J. Kossin, Y. Luo, J. Marengo, K. McInnes, M. Rahimi, et al., 2012, Changes in climate extremes and their impacts on the natural physical environment.

Serafin, K. A., P. Ruggiero, and K. Parker, 2019, What's streamflow got to do with it? a probabilistic simulation of the competing oceanographic and fluvial processes driving extreme along-river water levels: Natural Hazards and Earth System Sciences, 19.

Seyoum, S. D., Z. Vojinovic, R. K. Price, and S. Weesakul, 2012, Coupled 1d and non-inertia 2d flood inundation model for simulation of urban flooding: Journal of Hydraulic Engineering, 138, 23–34.

Shaw, E., 1983, Hydrology in practice: Chapman and Hall.

Shrestha, S., and W. Lohpaisankrit, 2017, Flood hazard assessment under climate change scenarios in the yang river basin, Thailand: International Journal of Sustainable Built Environment, 6, 285– 298.

Shustikova, I., A. Domeneghetti, J. C. Neal, P. Bates, and A. Castellarin, 2019, Comparing 2d capabilities of hec-ras and lisflood-fp on complex topography: Hydrological Sciences Journal, 64, 1769–1782.

Simonovic, S. P., A. Schardong, D. Sandink, and R. Srivastav, 2016, A web-based tool for the development of intensity duration frequency curves under changing climate: Environmental modelling & software, 81, 136–153.

Singh, H., Pirani, F. J., & Najafi, M. R., 2020. Characterizing the temperature and precipitation covariability over Canada. Theoretical and Applied Climatology, 139(3), 1543-1558.

Singh, H., & Najafi, M. R., 2020. Evaluation of gridded climate datasets over Canada using univariate and bivariate approaches: Implications for hydrological modelling. Journal of Hydrology, 584, 124673.

Singh H., Najafi M.R., 2020. Characterizing Non-Stationary Compound Extreme Events in a Changing Climate based on Large-Ensemble Climate Simulations Climate Dynamics, Climate Dynamics, DOI: 10.1007/s00382-020-05538-2

Tassew, B. G., M. A. Belete, and K. Miegel, 2019, Application of HEC-HMS model for flow simulation in the lake tana basin: The case of gilgel abay catchment, upper blue Nile basin, Ethiopia: Hydrology, 6, 21.

Teng, J., A. J. Jakeman, J. Vaze, B. F. Croke, D. Dutta, and S. Kim, 2017, Flood inundation modelling: A review of methods, recent advances and uncertainty analysis: Environmental Modelling & Software, 90, 201–216.

Terrapoint. 2010. Hatch Shearstown and Stephenville Project Report.

Thompson, J., H. R. Sørenson, H. Gavin, and A. Refsgaard, 2004, Application of the coupled mike she/mike 11 modelling system to a lowland wet grassland in southeast England: Journal of Hydrology, 293, 151–179.

Thompson, K. R., Bernier, N. B., & Chan, P. 2009. Extreme sea levels, coastal flooding and climate change with a focus on Atlantic Canada. *Natural hazards*, *51*(1), 139-150.

Trenberth, K. E., 2011, Changes in precipitation with climate change: Climate Research, 47,

123– 138.

UNISDR, and CRED, 2015, The human cost of natural disasters 1995-2015.

Van, P. D. T., Popescu, I., Van Griensven, A., Solomatine, D. P., Trung, N. H., & Green, A. 2012. A study of the climate change impacts on fluvial flood propagation in the Vietnamese Mekong Delta. *Hydrology & Earth System Sciences*, *16*(12).

Van Der Knijff, J. M., Younis, J., & De Roo, A. P. J. 2010. LISFLOOD: a GIS-based distributed model for river basin scale water balance and flood simulation. *International Journal of Geographical Information Science*, *24*(2), 189-212.

Vanderkimpen, P., Melger, E., & Peeters, P. 2008. Flood modeling for risk evaluation: a MIKE FLOOD vs. SOBEK 1D2D benchmark study.

Vitousek, S., P. L. Barnard, C. H. Fletcher, N. Frazer, L. Erikson, and C. D. Storlazzi, 2017, Doubling of coastal flooding frequency within decades due to sea-level rise: Scientific reports, 7, 1–9.

Vojtek, M., A. Petroselli, J. Vojteková, and S. Asgharinia, 2019, Flood inundation mapping in small and ungauged basins: sensitivity analysis using the eba4sub and hec-ras modeling approach: Hydrology Research, 50, 1002–1019.

Wahl, T., S. Jain, J. Bender, S. D. Meyers, and M. E. Luther, 2015, Increasing risk of compound flooding from storm surge and rainfall for major us cities: Nature Climate Change, 5, 1093–1097.

Wagener, T., Boyle, D. P., Lees, M. J., Wheater, H. S., Gupta, H. V., & Sorooshian, S. 2001. A framework for development and application of hydrological models.

Webster, T., McGuigan, K., Collins, K., & MacDonald, C. 2014. Integrated river and coastal hydrodynamic flood risk mapping of the lahave river estuary and town of Bridgewater, Nova Scotia, Canada. *Water*, *6*(3), 517-546.

Western Health. (n.d.). Bay St. George Long Term Care Centre.cho Retrieved May 17, 2020, http://westernhealth.nl.ca/home/locations/locations-2/bay-st-george-long-term-care-centre/

Wilby, R. L., K. J. Beven, and N. Reynard, 2008, Climate change and fluvial flood risk in the UK: More of the same?: Hydrological Processes: An International Journal, 22, 2511–2523.

Woodruff, J. D., J. L. Irish, and S. J. Camargo, 2013, Coastal flooding by tropical cyclones and sea-level rise: Nature, 504, 44–52.

Yin, J., Yu, D., Yin, Z., Liu, M., & He, Q. 2016. Evaluating the impact and risk of pluvial flash flood on intra-urban road network: A case study in the city center of Shanghai, China. *Journal*

of hydrology, *537*, 138-145.

Yu, D., & Lane, S. N. 2006. Urban fluvial flood modelling using a two-dimensional diffusion-wave treatment, part 1: mesh resolution effects. *Hydrological Processes: An International Journal*, *20*(7), 1541-1565.

Zahmatkesh, Z., S. J. Burian, M. Karamouz, H. Tavakol-Davani, and E. Goharian, 2015, Low-impact development practices to mitigate climate change effects on urban stormwater runoff: Case study of New York City: Journal of Irrigation and Drainage Engineering, 141, 04014043.

Zheng, F., S. Westra, and S. A. Sisson, 2013, Quantifying the dependence between extreme rainfall and storm surge in the coastal zone: Journal of hydrology, 505, 172–187.

Zhou, Q., Mikkelsen, P. S., Halsnæs, K., & Arnbjerg-Nielsen, K. 2012. Framework for economic pluvial flood risk assessment considering climate change effects and adaptation benefits. *Journal of Hydrology*, *414*, 539-549.

Zscheischler, J., S. Westra, B. J. Van Den Hurk, S. I. Seneviratne, P. J. Ward, A. Pitman, A. AghaK- ouchak, D. N. Bresch, M. Leonard, T. Wahl, et al., 2018, Future climate risk from compound events: Nature Climate Change, 8, 469–477.

SHUYI WANG

EDUCATION

Western University **Sep 2018 – Dec 2020**
M.E.Sc in Civil Engineering
Specializing in Environmental and Water Resources Engineering

Western University **Sep 2014 – May 2018**
B.E.Sc in Civil Engineering
Specializing in Environmental Engineering

EXPERIENCE

Graduate Teaching Assistant **Jan 2019 – May 2020**
Western University, London, ON.
Courses: ES4498G and ES1022

Lab Technician Summer Intern **May 2017 – Aug 2017**
Aerospace Kaitian Environmental Technology Co., Ltd.

SKILLS

Software: MATLAB, MS Office, MODFLOW, HEC-RAS, HEC-HMS, ArcGIS, Python

Language: English, Mandarin

AWARD

- The Western Scholarship of Distinction
- Dean's Honor List
- DeMarco Family Green Technologies Award
- City of London Design Competition Second Place

PROJECTS

Capstone – Chippewa of the Thames First Nation WTP **Sep 2017 – Mar 2018**
Awarded as second place in City of London Design Competition

Drinking Water Filtration System Design **Sep 2016 – Dec 2016**